

Analysis of the slow-moving landslides in the Mazar Region in southeast Ecuador

Urgilez Vinueza, A.R.

DOI

[10.4233/uuid:04e4fe71-d257-4cac-aaa6-56390b3d80f9](https://doi.org/10.4233/uuid:04e4fe71-d257-4cac-aaa6-56390b3d80f9)

Publication date

2024

Document Version

Final published version

Citation (APA)

Urgilez Vinueza, A. R. (2024). *Analysis of the slow-moving landslides in the Mazar Region in southeast Ecuador*. [Dissertation (TU Delft), Delft University of Technology]. <https://doi.org/10.4233/uuid:04e4fe71-d257-4cac-aaa6-56390b3d80f9>

Important note

To cite this publication, please use the final published version (if applicable). Please check the document version above.

Copyright

Other than for strictly personal use, it is not permitted to download, forward or distribute the text or part of it, without the consent of the author(s) and/or copyright holder(s), unless the work is under an open content license such as Creative Commons.

Takedown policy

Please contact us and provide details if you believe this document breaches copyrights. We will remove access to the work immediately and investigate your claim.

**ANALYSIS OF THE SLOW-MOVING LANDSLIDES IN
THE MAZAR REGION IN SOUTHEAST ECUADOR**

ANALYSIS OF THE SLOW-MOVING LANDSLIDES IN THE MAZAR REGION IN SOUTHEAST ECUADOR

Dissertation

for the purpose of obtaining the degree of doctor
at Delft University of Technology

by the authority of the Rector Magnificus, Prof.dr.ir. T.H.J.J. van der Hagen,
chair of the Board for Doctorates

to be defended publicly on Monday 15 January 2024 at 15:00 hours

by

Alexandra Rocio URGILEZ VINUEZA

Master of Science in Hydrogeology and Water Management
Newcastle University, Newcastle upon Tyne, United Kingdom
born in Cuenca, Ecuador

This dissertation has been approved by the promotors.

Composition of the doctoral committee:

Rector Magnificus	Chairperson
Prof.dr.ir. M. Bakker	Delft University of Technology, promotor
Dr. T. A. Bogaard	Delft University of Technology, promotor

Independent members:

Prof.dr.ir. R. Uijlenhoet	Delft University of Technology, Netherlands
Prof.dr. R. Greco	Università degli Studi della Campania “Luigi Vanvitelli”, Italy
Prof.dr. S. de Jong	Utrecht University, Netherlands
Dr. R. C. Lindenbergh	Delft University of Technology, Netherlands
Prof.dr. P. J. Vardon	Delft University of Technology, reserve member

Other members:

Dr. P.I. Guzmán Cárdenas	Universidad del Azuay, Ecuador
--------------------------	--------------------------------



Keywords: Slow-moving landslides, Hydro-geology, Hydro-Meteorology, Accelerations-decelerations, Multiple regression

Copyright © 2024 by A. Urgilez Vinueza

ISBN: 978-94-6384-526-7

Printed by: Proefschrift-aio.nl

The photo on the cover page shows slow-moving landslides in southeast Ecuador.

An electronic version of this dissertation is available at

<http://repository.tudelft.nl/>

To my family

CONTENTS

Summary	xi
Resumen	xv
1 Introduction	1
1.1 Research objective	5
1.2 Research outline	6
2 Characterization and hydrological analysis of the Guarumales deep-seated landslide in the tropical Ecuadorian Andes	9
2.1 Introduction	11
2.2 Description of the Study Area	13
2.3 Methodology and Data Availability	16
2.4 Results.	21
2.4.1 Geology	21
2.4.2 Surface Dynamics	23
2.4.3 Hydro-meteorological analysis	28
2.5 A Hydrogeological Conceptual Model of Guarumales Slope	33
2.6 Discussion	35
2.7 Conclusion	38
3 A new method to detect changes in displacement rates of slow-moving landslides using InSAR time series	41
3.1 Introduction	43
3.2 InSAR methods	44
3.2.1 InSAR processing for Big Sur, California	44
3.2.2 InSAR processing for Southeast Ecuador	45

3.3	Methodology for the detection of accelerations and decelerations. . .	46
3.3.1	Pixel selection.	46
3.3.2	Outlier detection	47
3.3.3	Model fitting, evaluation, and selection.	48
3.3.4	Spatial analysis: Detection of accelerations and decelerations	50
3.4	Case study 1: Mud Creek landslide	51
3.4.1	Pixel selection, case 1.	51
3.4.2	Outlier detection, case 1	52
3.4.3	Model fitting, evaluation, and selection, case 1	53
3.4.4	Spatial analysis: Detection of accelerations and decelerations, case 1	54
3.5	Case study 2: Mazar region	56
3.5.1	Pixel selection, case 2.	57
3.5.2	Outlier detection, case 2	58
3.5.3	Model fitting, evaluation, and selection, case 2	59
3.5.4	Detection of accelerations and decelerations in a cluster, case 2	59
3.6	Discussion	62
3.7	Conclusions.	64
4	Evaluation of the dynamics of the slow-moving landslides in the Mazar region using InSAR-derived displacement data	67
4.1	Introduction	69
4.2	Description of the study area	70
4.3	Data sources	71
4.3.1	Displacement data	71
4.3.2	Hydrometeorological data	72
4.4	Methodology	73
4.4.1	Displacement analysis	73
4.4.2	Hydrometeorological variables	74
4.4.3	Evaluation of displacement data against hydrometeorological variables	75

4.5	Results	76
4.5.1	Displacement analysis	76
4.5.2	Hydrometeorological analysis	82
4.5.3	Evaluation of displacement data against hydrometeorological variables	83
4.6	Discussion	86
4.7	Conclusion	89
5	Synthesis and Conclusions	91
5.1	Guarumales case study	93
5.2	Development of a method to detect accelerations and decelerations from InSAR displacement time series	94
5.3	Analysis of the detected accelerations and decelerations in the Mazar region	95
5.4	Limitations of slow-moving landslides research in the context of the Andes mountain range	97
5.5	Slow-moving landslides in the Ecuadorian Andes	99
5.6	Future Work.	100
	References	101
A	In-situ and satellite rainfall analysis for the Mazar region	123
	Acknowledgements	129
	Curriculum Vitae	131
	List of Publications	133
A.1	Papers	133
A.2	Presentations	133

SUMMARY

Landslide activity in the Andes remains an ongoing natural hazard with significant implications for regional development. Slow-moving landslides, while not typically resulting in catastrophic outcomes, can still cause substantial damage to critical infrastructure, including roads, buildings, crops, and hydropower dams. In southeast Ecuador, slow-moving landslides threaten the stability and functionality of the Mazar dam and reservoir. This thesis aimed to address these challenges by characterizing the slow-moving landslides in the Mazar region and developing a systematic approach to identify changes in their displacement rates, understand their physical causes and assess the influence of hydrometeorological forcings. [Chapter 1](#) establishes the relevance of slow-moving landslides in Ecuadorian society and highlights the common mechanisms observed in slopes influenced by reservoirs. Additionally, the chapter explores several methods utilized to model these mechanisms under the influence of hydrometeorological factors.

[Chapter 2](#) presents the characterization and hydrogeological analysis of the Guarumales landslide, situated approximately 20 kilometers downstream of the Mazar dam. This deep-seated landslide has been under monitoring for an extended period, providing valuable data such as displacement, rainfall, groundwater levels, and drain flow for analysis. We examined the displacement data spanning 18 years, revealing a consistent movement throughout the entire period. However, the limited measurement accuracy and time resolution posed challenges in identifying potential accelerations or decelerations in response to hydrometeorological forcings. The groundwater and slope drainage data showed a delayed response to rainfall events. Moreover, we constructed a conceptual model of the landslide, highlighting the presence of giant boulders within the colluvium, perched groundwater systems, and a relatively deep slip surface.

Chapter 3 focused on interpreting the landslides surrounding the Mazar dam and reservoir. Given the limited availability of comprehensive in-situ data, we turned to satellite-derived data for our analysis. Using InSAR displacement time series, we tracked the deformation of the region with high temporal and spatial resolution. In this chapter, we developed a systematic method to identify, quantify, and inventory changes in the surface deformation rate of slowly deforming areas at local and regional scales. The result was the creation of multitemporal maps depicting unstable areas and an inventory of the timing of changes in their deformation rates. To validate our method, we applied it to the Mud Creek landslide in the United States, where a previous study had thoroughly evaluated the interferograms used in defining the InSAR displacement time series, yielding a high-quality dataset. Our method successfully detected monthly accelerations and decelerations, aligning with periods of heavy and no rainfall, respectively. Subsequently, we applied our method to the Mazar reservoir region. While the displacement time series in this area were of lower quality than the Mud Creek dataset, we could still identify deforming areas displaying complex acceleration and deceleration patterns.

Chapter 4 aimed to leverage the results obtained in **chapter 3**, specifically focusing on identifying the timing and frequency of changes in the displacement rate of landslides within the Mazar reservoir area. The primary objective was to investigate whether these changes correlated with hydrometeorological forcings using multiple linear regression analysis. The analysis did not reveal any significant correlation between the dynamics of the landslides and the seasonal behavior of hydrometeorological forcings in the study area. Our findings suggested that the available hydrometeorological variables were insufficient in amount and level of detail to explain the behavior of slow-moving landslides in the Mazar region. Interestingly, most of the identified surficial dynamics exhibited only one or two velocity changes over four years, independent of the seasonal variations in hydrometeorological data. In the case of the Mazar region, some challenges hindered our analysis. On the one hand, the lower quality InSAR displacement time series could only show the most significant changes in displacement rate,

while smaller (likely seasonal) changes were hidden within the noise. On the other hand, the limited availability of in-situ data, such as groundwater and soil moisture, did not allow a more detailed slope analysis. Local factors are crucial in influencing the sliding mechanisms of landslides around the Mazar reservoir. A more in-depth analysis of local slope settings and mechanisms is essential to better comprehend the effect of hydrometeorological forcings in the area. Satellite-derived surficial dynamics would greatly benefit from a comprehensive examination of local factors to provide a complete understanding of the slow-moving landslide dynamics in the Mazar region.

Chapter 5 offers a synthesis of the findings in this thesis, the overall conclusions of each chapter, discusses the limitations of this kind of research in the Andes and discusses the relevance of the findings in the context of the Ecuadorian Andes. Our research showed notable relationships between rainfall patterns and groundwater responses, as the Guarumales case study demonstrated. However, we encountered challenges in identifying empirical relationships between displacement (whether derived from in-situ measurements or satellite data) and the hydrometeorological forcings at both the local scale (Guarumales) and regional scale (Mazar region). The limitations primarily stemmed from the lack of a comprehensive dataset, hindering a detailed analysis of the slopes in the Mazar region. This critical insight is significant in countries like Ecuador, where hydropower development is a priority. As harnessing hydroelectric resources increases, the accurate assessment and monitoring of slow-moving landslide dynamics become even more crucial. Improving the spatiotemporal resolution of the in-situ monitoring systems is imperative for a better insight into slow-moving landslide dynamics and, thus, a reliable landslide early-warning system.

RESUMEN

Los deslizamientos de tierra en los Andes siguen siendo un peligro natural continuo con importantes implicaciones para el desarrollo regional. Los deslizamientos de tierra de movimiento lento, si bien no suelen tener resultados catastróficos, aún pueden causar daños sustanciales a infraestructura crítica, incluidas carreteras, edificios, cultivos y represas hidroeléctricas. En el sureste de Ecuador, deslizamientos de tierra de lento avance amenazan la estabilidad y funcionalidad de la presa y el embalse de Mazar. Esta tesis tuvo como objetivo abordar estos desafíos caracterizando este tipo de deslizamientos de tierra en la región de Mazar y desarrollando un enfoque sistemático para identificar cambios en su velocidad de desplazamiento, comprender sus causas físicas y evaluar la influencia de los factores hidrometeorológicos. El [Capítulo 1](#) establece la relevancia de los deslizamientos de tierra de movimiento lento en la sociedad ecuatoriana y destaca los mecanismos comunes observados en laderas influenciadas por embalses. Además, el capítulo explora varios métodos utilizados para modelar estos mecanismos bajo la influencia de factores hidrometeorológicos.

El [Capítulo 2](#) presenta la caracterización y análisis hidrogeológico del deslizamiento de Guarumales, situado aproximadamente a 20 kilómetros aguas abajo de la presa Mazar. Este deslizamiento de tierra profundo ha estado en monitoreo durante un período prolongado, proporcionando datos valiosos para su análisis como desplazamiento, precipitaciones, niveles de agua subterránea y flujo de drenaje. Examinamos 18 años de datos de desplazamiento, revelando un movimiento constante durante todo el período. Sin embargo, la limitada precisión de las mediciones y la resolución temporal plantearon desafíos a la hora de identificar posibles aceleraciones o desaceleraciones en respuesta a los factores hidrometeorológicos. Los datos de aguas subterráneas y drenaje mostraron una respuesta tardía a los eventos de lluvia. Además, construimos un modelo

conceptual del deslizamiento, destacando la presencia de rocas gigantes dentro del coluvión, sistemas de agua subterránea encaramados y una superficie de deslizamiento relativamente profunda.

El [Capítulo 3](#) se centró en la interpretación de los deslizamientos de tierra que rodean la presa y el embalse de Mazar. Dada la disponibilidad limitada de datos in situ, recurrimos a datos derivados de satélites para nuestro análisis. Utilizando series temporales de desplazamiento InSAR, rastreamos la deformación de la región con alta resolución temporal y espacial. En este capítulo, desarrollamos un método sistemático para identificar, cuantificar e inventariar cambios en la velocidad de deformación de la superficie de áreas que se deforman lentamente a escalas local y regional. Como resultado se desarrollaron mapas multitemporales que representan áreas inestables y un inventario de los cambios en su velocidad de deformación. Para validar nuestro método, lo aplicamos al deslizamiento de tierra de Mud Creek en los Estados Unidos, donde un estudio previo había evaluado exhaustivamente los interferogramas utilizados para definir la serie temporal de desplazamiento InSAR, generando un conjunto de datos de alta calidad. Nuestro método detectó con éxito aceleraciones y desaceleraciones mensuales, alineándose con períodos de lluvia intensa y sin lluvia, respectivamente. Posteriormente, aplicamos nuestro método a la región del embalse de Mazar. Si bien las series temporales de desplazamiento en esta área fueron de menor calidad que el conjunto de datos de Mud Creek, aún pudimos identificar áreas deformantes que muestran patrones complejos de aceleración y desaceleración.

El [Capítulo 4](#) tuvo como objetivo aprovechar los resultados obtenidos en el [capítulo 3](#), centrándose específicamente en identificar el momento y la frecuencia de los cambios en la velocidad del desplazamiento de los deslizamientos de tierra dentro del área del embalse de Mazar. El objetivo principal fue investigar si estos cambios se correlacionaban con los factores hidrometeorológicos mediante un análisis de regresión lineal múltiple. El análisis no reveló ninguna correlación significativa entre la dinámica de los deslizamientos y el comportamiento estacional de los factores hidrometeorológicos en el área de estudio.

Nuestros hallazgos sugirieron que las variables hidrometeorológicas disponibles eran insuficientes en cantidad y nivel de detalle para explicar el comportamiento de los deslizamientos de tierra de lento movimiento en la región de Mazar. Curiosamente, la mayoría de las dinámicas superficiales identificadas exhibieron sólo uno o dos cambios de velocidad durante cuatro años, independientemente de las variaciones estacionales en los datos hidrometeorológicos. En el caso de la región de Mazar, algunos desafíos obstaculizaron nuestro análisis. Por un lado, la serie temporal de desplazamiento InSAR de menor calidad solo pudo mostrar los cambios más significativos en la velocidad de desplazamiento, mientras que los cambios más pequeños (probablemente estacionales) pudieron haber quedado ocultos dentro de la dispersión de los datos. Por otro lado, la limitada disponibilidad de datos in situ, como el agua subterránea y la humedad del suelo, no permitió realizar un análisis más detallado. Los factores locales influyen crucialmente en los mecanismos de deslizamientos alrededor del embalse de Mazar. Es esencial realizar un análisis más profundo de la configuración y los mecanismos de las pendientes locales para comprender mejor el efecto de los factores hidrometeorológicos en el área. La dinámica superficial derivada de satélites se beneficiaría enormemente de un examen exhaustivo de los factores locales para proporcionar una comprensión completa de la dinámica de los deslizamientos de lento movimiento en la región de Mazar.

El [Capítulo 5](#) ofrece una síntesis de los hallazgos de esta tesis, las conclusiones generales de cada capítulo, discute las limitaciones de este tipo de investigación en los Andes y discute la relevancia de los hallazgos en el contexto de los Andes ecuatorianos. Nuestra investigación mostró relaciones notables entre los patrones de lluvia y las respuestas del agua subterránea, como lo demostró el estudio de caso de Guarumales. Sin embargo, encontramos desafíos al identificar relaciones empíricas entre el desplazamiento (ya sea derivado de mediciones in situ o datos satelitales) y los forzamientos hidrometeorológicos tanto a escala local (Guarumales) como regional (región de Mazar). Las limitaciones surgieron principalmente de la falta de un conjunto de datos completo, lo que impidió un análisis detallado de las laderas en la región de Mazar. Esta visión crítica es significativa en países como Ecuador, donde el desarrollo hidroeléctrico es una priori-

dad. A medida que aumenta el aprovechamiento de los recursos hidroeléctricos, la evaluación y el seguimiento precisos de la dinámica de los deslizamientos de tierra de lento movimiento se vuelven aún más cruciales. Mejorar la resolución espaciotemporal de los sistemas de monitoreo in situ es imperativo para tener una mejor comprensión de la dinámica de los deslizamientos de movimiento lento y, por lo tanto, un sistema confiable de alerta temprana de deslizamientos.

1

INTRODUCTION

Parts of this chapter are based on:

Urgilez Vinueza, A., Robles, J., Bakker, M., Guzman, P., and Bogaard, T. (2020). *Characterization and hydrological analysis of the Guarumales deep-seated landslide in the tropical Ecuadorian Andes*. *Geosciences*, 10(7), 267, <https://doi.org/10.3390/geosciences10070267>

Urgilez Vinueza, A., Handwerger, A.L., Bakker, M., and Bogaard, T. (2022). *A new method to detect changes in displacement rates of slow-moving landslides using InSAR time series*. *Landslides*, 19(9), 2233-2247, <https://doi.org/10.1007/s10346-022-01913-8>

Landslides are a natural hazard that occur worldwide, with consequences ranging from economic losses to many fatalities (Guzzetti et al., 2003; Petley, 2012; Papathoma-Köhle et al., 2015; Froude and Petley, 2018). The study of landslides is an essential task in mountainous areas in the world, especially in underdeveloped areas such as Latin America. Here, the presence of the Andes mountain range, accompanied by its relatively young geological composition (Zeil, 1979), makes it a landslide-prone area (Petley, 2012; Alcántara-Ayala and Oliver-Smith, 2014). Despite this situation, urban areas have developed around the mountain range, and Ecuador is no exception.

One of Ecuador's most critical infrastructure developments is the construction of dams for electricity generation as an alternative to fossil fuels. In the next few years, Ecuador will commission 25 hydropower plants around the country in addition to the 71 already existing projects, to generate 90% of the national electrical demand (Míte-León and Barzola-Monteses, 2018; Barzola-Monteses et al., 2019). While hydropower is considered an environmentally-friendly energy generation alternative, it can adversely affect the environment (Alho, 2011; Díaz et al., 2019). Implementing hydropower plants involves the construction of dams, which impound an extensive area. The reservoir affects the morphodynamics processes and especially the slopes' stability around it.

Researchers have found that in areas where a reservoir is present, fast-moving and slow-moving landslides are likely to occur, such as reported in case of the Three Gorges Dam in China (Jian et al., 2009; Du et al., 2013; Xu et al., 2015), the Vajont landslide in Italy (Barla and Paronuzzi, 2013), and several cases in the Andes (Schuster et al., 2002; Plaza et al., 2011). It is known that old landslide reactivations and new landslide occurrences may be caused by water level variations and the reservoir impoundment itself (e.g., Schuster (1979); Pinyol et al. (2012); Guo et al. (2015)). The variations of reservoir water levels and rainfall can cause seepage-induced or buoyancy-induced periodic deformations, showing either step-wise or constant cumulative displacement. The mechanical properties of slip zones also play a role in reservoir-induced landslides (Tang et al., 2019).

Regional-scale investigations are carried out to reduce the effects of landslide hazard (Xu et al., 2017; Bogaard and Greco, 2018; Monsieurs et al., 2019; Wang et al., 2020). The focus can be on rapid or catastrophic landslides (Xu et al.,

2017), which refer to events that displace at high velocity and frequently cause loss of life and infrastructure. On the other hand, the focus can be on slow-moving landslides, which refer to slow to very slow slope movement that can be active for a long time without causing catastrophic damage (Varnes, 1978). However, given a precise set of circumstances, they could be prone to fail catastrophically (i.e., suddenly increase their velocity until failure) (e.g., Handwerger et al. (2019b)). These types of landslides are typically investigated for mapping purposes (Lu et al., 2012; Borrelli et al., 2018; Zhang et al., 2018), long-term monitoring (Bekaert et al., 2020), and individual case studies (Tomás et al., 2016; Kang et al., 2017; Bounab et al., 2021; Dille et al., 2021; Li et al., 2021; Jacquemart and Tiampo, 2021).

These regional investigations can be supported using either empirically or physically based models. Empirical models refer to data-driven models that use a set of available environmental variables to predict landslide occurrence using rainfall thresholds (Segoni et al., 2018; Uwihirwe et al., 2020), produce maps of landslide hazards (e.g., Mancini et al. (2010)), among other applications. The conditions that predispose landslides to occur are determined using statistical analyses between site variables (e.g., soil, geology, hydrometeorology) and a list of past landslides, their location, and type (Dai and Lee, 2002; Kirschbaum et al., 2012). These models assume that the geological conditions over a selected region are comparable. However, this might not be applicable everywhere. Additionally, these models rely on the availability and completeness of landslide inventories, and if available, they likely represent landslides that occurred in urban areas or inhabited rural areas (Monsieus et al., 2018).

On the other hand, physically based models consider geotechnical and hydrological processes using equations to model the physical behavior of the slope. They tend to be more robust than the data-driven models, providing assessments of rainfall-induced and earthquake-induced landslides (e.g., An et al. (2016); Cui et al. (2022); Zhang et al. (2022, 2018)). Probabilities of slope failure are also evaluated using these types of models by combining hydrological models (that determine the pore pressure changes in the soil due to rainfall) and slope stability models (estimates the factor of safety on potential deformation areas) (Crosta and Frattini, 2003; Rosso et al., 2006). These models need detailed in-situ geotech-

nical and hydrological data to work correctly, which is often scarce and only found in local or site-based studies and difficult to replicate at large scales. Their performance can be limited due to the availability of data on soil properties (Valentino et al., 2011).

Some studies combine empirical and physically based dynamic models to forecast landslide occurrence, improve landslide susceptibility maps, and define rainfall-induced landslide early warning thresholds (Anderson and Lloyd, 1991; Rosso et al., 2006; Kuriakose et al., 2009; Goetz et al., 2011; Peruccacci et al., 2017). Hydrometeorological landslide early-warning thresholds indicate the minimum rainfall, groundwater, and any other hydrological parameters that can be connected to landslide initiation at any scale (i.e., local, regional, or global) (Uwihirwe et al., 2020; Ciavolella et al., 2016; Mostbauer et al., 2018). However, these are almost exclusively developed for fast-moving landslides. Empirically-based research on fast-moving landslides relies on the completeness of landslide inventories and the availability of hydrometeorological data over the selected area.

In contrast, limited attention has been given to empirically-based research of slow-moving landslides. In this case, there is no inventory of landslide occurrences since their movement is constant throughout time unless they fail catastrophically. Here, the displacement time series of slow-moving landslides are evaluated against hydrometeorological variables in the area to make sense of the slow-moving dynamics of the slopes represented by the cumulative displacement time series of available monitored points.

These slow-moving landslides are commonly monitored with remote sensing and in-situ approaches. Remote sensing approaches include Light Detection and Ranging (lidar) (Mackey and Roering, 2011; Pirasteh et al., 2018; Jaboyedoff and Derron, 2020), Interferometric synthetic aperture radar (InSAR) (Strozzi et al., 2005; Handwerger et al., 2013; Bayer et al., 2018; Dai et al., 2020), and optical remote sensing (Bennett et al., 2016; Lacroix et al., 2020a). The in-situ approach includes the Global Navigation Satellite System (GNSS) (Mulas et al., 2018; Notti et al., 2020), terrestrial laser scanners (Rosser et al., 2007; Aryal et al., 2012; Booth et al., 2018), geophysical methods (Whiteley et al., 2019b,a), accelerometers (Bagwari et al., 2021), slope deformation sensors (Askarinejad and Springman, 2017), inclinometers, extensometers, and Electronic Distance Measurement (EDM) (Pet-

ley et al., 2005; Pecoraro et al., 2019). While the highest data quality comes from in-situ measurements, these are limited to specific locations within a single landslide and thus fail to capture spatial changes in regional landslide behavior. Additionally, constant monitoring of slow-moving landslides can be challenging in areas without sufficient resources. Satellite-based data is an alternative to in-situ monitoring since large regions of active slow-moving landslide bodies can be identified and monitored (Lu et al., 2012; Bianchini et al., 2018; Del Soldato et al., 2019; van Natijne et al., 2020). They provide high spatial and temporal resolution datasets. This approach is preferred where in-situ monitoring is scarce or, in extreme cases, impossible.

Slow-moving landslides research, therefore, includes identifying anomalous points in their displacement time series (i.e., points indicating changes in the dynamic of motion) (Raspini et al., 2018), classifying these time series (Cigna et al., 2012; Berti et al., 2013), and identifying and classifying of ground motion areas (Bordoni et al., 2018; Raspini et al., 2019). Some studies evaluated the slow-moving dynamics against the seasonal behavior related to heavy rainfall, lithological composition, and slope geometry, among other variables (Handwerker et al., 2015, 2019a). These studies usually consist of long-term monitoring to provide decision-makers with information for the landslide hazard assessment (Raspini et al., 2019). Research on slow-moving landslides has been limited to the United States, Europe, and certain parts of Asia Lacroix et al. (2020b), whereas slow-moving landslides are abundant in the Andes region of South America.

1.1. RESEARCH OBJECTIVE

The main objective of this dissertation is to develop a systematic approach to identify the onset of accelerations and decelerations, their physical causes, and the influence of hydrometeorological factors on the landslides near the Mazar dam and reservoir in southeast Ecuador. Specifically, we address the following objectives:

1. To perform a hydrogeological characterization of the Guarumales landslide at the local scale while considering its broader implications within the Mazar region;

2. To develop a new methodology to identify accelerations and decelerations of slow-moving landslides at the regional scale using InSAR displacement time series, and apply it on the landslides in the Mazar region;
3. To analyze the detected accelerations and decelerations of the landslides in the Mazar region and explore the influence of hydrometeorological forcings on the dynamics of the landslides.

This thesis presents an evaluation of the slow-moving landslides in the Mazar region in southeast Ecuador using data collected for over 20 years in the Guarumales landslide and a new method to detect changes in the normal behavior of the slow-moving landslides around the Mazar reservoir. Then we identify the timing and frequency of velocity changes in the Mazar reservoir area and investigate whether they are correlated with hydrometeorological forcings. We used InSAR displacement time series to identify and inventory the time a landslide starts to accelerate or decelerate. We then linked these changes to hydrometeorological factors such as rainfall and reservoir levels. A comprehensive approach to understanding the behavior of slow-moving landslides in Southeast Ecuador will have positive socio-economic consequences since it can help map and monitor potentially unstable areas before considering urban development. It can also be used for better urban planning, modeling, and forecasting this hazard.

1.2. RESEARCH OUTLINE

This thesis is organized as follows:

The second chapter, following the introduction chapter, is a case study of a landslide in the Ecuadorian Andes near the Mazar reservoir in southeast Ecuador. It summarizes the hydrometeorological factors affecting landslide behavior over 20 years of monitoring. Results show that the current management plan keeps the landslide relatively stable, with a constant rate of movement.

The third chapter aims to study slow-moving landslides at a regional scale and proposes a new method to detect accelerations and decelerations of slow-moving landslides based on InSAR displacement time series. This method was verified in California in the United States and Mazar in Ecuador. Results show that the method can reproduce shifts in the constant rate of movement of slow-

moving landslides observed in the field. With this method, we were able to produce high spatial and temporal resolution data for the monitoring of a large region.

The fourth chapter applies the method developed in chapter two to the slopes around the Mazar reservoir. It performs a multiple regression analysis between the displacement-based data and the hydrometeorological forcings in the area to identify the most important factors influencing the slow-moving dynamics.

The fifth chapter summarizes the findings of this research and discusses the relevance, advantages, and disadvantages of the site-scale and regional-scale analyses of the landslides threatening the functionality of the hydropower infrastructures in southeast Ecuador. The role of the hydrometeorological factors in this specific context is also analyzed. We finally discuss the limitations and possible alternatives for a regional follow-up assessment.

2

CHARACTERIZATION AND HYDROLOGICAL ANALYSIS OF THE GUARUMALES DEEP-SEATED LANDSLIDE IN THE TROPICAL ECUADORIAN ANDES

This chapter is based on: Urgilez Vinueza, A.; Robles, J.; Bakker, M.; Guzman, P.; Bogaard, T. Characterization and Hydrological Analysis of the Guarumales Deep-Seated Landslide in the Tropical Ecuadorian Andes. *Geosciences* 2020, 10, 267. <https://doi.org/10.3390/geosciences10070267>

Abstract

The high landslide risk potential along the steep hillslopes of the Eastern Andes in Ecuador provides challenges for hazard mitigation, especially in areas with hydropower dams and reservoirs. The objective of this study was to characterize, understand, and quantify the mechanisms driving the motions of the Guarumales landslide. This 1.5 km² deep-seated, slow-moving landslide is actively moving and threatening the “Paute Integral” hydroelectric complex. Building on a long time series of measurements of surface displacement, precipitation, and groundwater level fluctuations, we analyzed the role of predisposing conditions and triggering factors on the stability of the landslide. We performed an analysis of the time series of measured groundwater levels and drainage data using transfer functions. The geological interpretation of the landslide was further revised based on twelve new drillings. This demonstrated a locally complex system of colluvium deposits overlying a schist bedrock, reaching up to 100 m. The measured displacement rates were nearly constant at ~50 mm/year over the 18 years of study. However, the measurement accuracy and time resolution were too small to identify possible acceleration or deceleration phases in response to hydro-meteorological forcing. The groundwater and slope drainage data showed a lagged response to rainfall. Finally, we developed a conceptual model of the Guarumales landslide, which we hope will improve our understanding of the many other deep-seated landslides present in the Eastern Andes.

2.1. INTRODUCTION

Landslides are the movement of earth down the slope of a hill or mountain. Gravity is the primary driver of this movement, but water and other factors, including anthropogenic influences, may play a role as well (Sidle and Ochiai, 2006). There are several classification systems that describe the characteristics of the movement, including timing and predisposing and triggering factors (Sidle and Ochiai, 2006; Schuster and Fleming, 1982; Hutchinson, 1988; Cruden and Varnes, 1996; Hungr et al., 2001). Apart from the morphological classifications of landslides, Brönnimann (2011) proposed a classification system where the hydrogeological ‘architecture’ and predisposing conditions for landslide occurrence are defined by the permeability and degree of saturation of the slope layers. This approach allows researchers to assess the hydrogeological predisposing conditions and triggering mechanisms behind specific slope instabilities, and to characterize different landslides under the same hydrogeological conditions.

The occurrence of landslides is affected by time-dependent factors. Effective stress in landslides is controlled by the water content within the slope and is dynamically linked to slope deformation and progressive failure (Cotecchia et al., 2011). In several studies, rainfall is identified as the threshold parameter that determines the occurrence of landslides (e.g., Guzzetti et al. (2008)), but other factors must be considered as well, including antecedent water content, time-variant geotechnical parameters within the regolith, vegetation cover and land use, and the tectonic activities around the area (e.g., Sidle and Ochiai (2006); Prokešová et al. (2013); Brückl et al. (2013); Bogaard and Greco (2016); Sidle and Bogaard (2016); Belle et al. (2018)).

Deep-seated landslides require water to accumulate in the landslide body to initiate movement (either due to rainfall or snowmelt), unless they are triggered by a seismic event. Acceleration can vary from days to several weeks after a meteorological event has happened and the hydrological threshold is reached (Sidle and Ochiai, 2006) (defined as the condition after which an acceleration of the slope occurs), when seismicity is not the trigger. Groundwater variation can be linked to the occurrence of deep-seated landslides, but other factors also affect movement, including the different geological compositions of the regolith and bedrock, and the permeability and quality of bedrock (e.g., fractures) (Bogaard

and Greco, 2016).

Landslides in tropical areas have been relatively under-studied compared to other areas (e.g., Europe, USA). Underlying factors that are essential for landslide occurrence are permanently present in tropical mountainous areas, including rainfall throughout the entire year (Loaiza-Usuga et al., 2018) (present in 50% of the areas around the tropical belt, including Ecuador), tectonic activity, and erosion processes that influence slope geometry and surface conditions leading to changes in predisposing factors. Additionally, tropical areas are mainly located in developing countries, where anthropogenic factors such as human settlements, agriculture, change of land use, and mining are not always adequately planned and controlled, which may become important factors to consider for landslide occurrence (Gupta, 2011).

Located in South America, Ecuador is crossed by the Andes mountain range and is situated in a geo-dynamically active region. The Ecuadorian Andes is formed by elevated heights (up to ~6000 m; e.g., Chimborazo volcano). Metamorphosed Triassic and Jurassic plutons dominate, separated by screens of metamorphosed sedimentary and volcanic rocks. The most important structure is the sub-Andean Fault (major reverse fault), and the Inter-Andean Valley with Oligocene and Miocene ignimbrites, that obscures the western limit of metamorphic rocks that form the Cordillera Real (Spikings et al., 2001). The presence of faults increases seismic risk, leading to deformation processes of the terrain (e.g., Baize et al. (2015); Tibaldi et al. (1995)) and aiding the formative phases of the Ecuadorian Andes (Baize et al., 2015).

Some key reported landslides in the Ecuadorian Andes (i.e., with major economical and societal repercussions) include the rotational movements of Pacha in 2004, Guasuntos in 2000, La Josefina in 1993, and debris avalanches in Las Moras in 1985 (Argentino et al., 2007). Several detailed case studies of landslides in the Andes showed the importance of land cover and land cover conversion, e.g., from forest to pasture, on slope deformation in southeastern Ecuador (Guns and Vanacker, 2013, 2014). Among the predisposing factors that influence landslide occurrence, the most common are lithological and hydrogeological conformation (Zimmermann and Elsenbeer, 2009), geomorphology (Vorpahl et al., 2012), volcanic activity, land use and land use change (Guns and Vanacker, 2013;

Soto et al., 2017), and anthropogenic impacts (Muenchow et al., 2012), while triggering factors include rainfall and seismic activity (e.g., Schuster et al. (2002); Moreiras (2005); Aristizábal et al. (2017)).

At the transition between the Andes and the low-lying Amazon rainforest, landslides can be further enhanced by the construction of artificial lakes created for hydropower production, due to an increased pore water pressure at the toe of the slope (Schuster, 1979). Approximately 35% of Ecuador's electricity is generated from three dams, which form the Paute Integral hydroelectric complex, over the Paute River. Along two of those reservoirs and their vicinities, researchers identified twenty-one deep-seated landslides (Robles and Guzmán, 2017). These landslides pose a critical risk to the communities, the operation of the lakes, and the surrounding infrastructure.

Guarumales is one of the twenty-one identified landslides located in the Paute Integral hydroelectric complex and is classified as a deep-seated landslide. Various studies have been conducted on the Guarumales landslide (e.g., Cevallos Andrade (2010); Almeida et al. (1997); Vásconez (2000); López (1995)). However, detailed research on the long-term hydrological factors that may affect the landslide dynamics was not performed prior to this study.

The objectives of this study were to characterize, understand, and quantify the possible driving mechanisms underlying the Guarumales landslide. Special attention was paid to predisposing conditions, such as geology/lithology, and the relationship between the slope acceleration (if any observed), and possible triggering factors, such as rainfall and subsequent groundwater fluctuations. A detailed understanding of the Guarumales deep-seated, slow-moving landslide is expected to shed light on the other landslides around the Paute Integral hydroelectric complex, which will contribute to a better hazard and risk assessment for the entire region.

2.2. DESCRIPTION OF THE STUDY AREA

The Guarumales landslide (2°35' S, 78°30' W) is a ~1.5 km² deep-seated landslide located in the Eastern Andes (Cordillera Real), 110 km from the city of Cuenca. The altitude at the Paute River basin varies from ~400 to ~4600 m.a.s.l. (Vásconez, 2000). The geology of Ecuador is highly complex since the Andes have grown

through a combination of events like compression, uplift, intrusion, crustal thickening, and volcanism. In Ecuador, the boundary between accreted terranes and S American continental crust is unclear (Pratt et al., 2005). However, some models have been proposed for the evolution of the Cordillera Real. Pratt et al. (2005) and Spikings et al. (2001) proposed geological models in which new geological field observations aided in adjusted interpretations of the geological evolution of the Cordillera Real and the model of autochthonous terrain through the mountain range.

Morpho-structurally, Litherland et al. (1994) established five lithotectonic divisions consisting of belts or informal metamorphic terrains such as Guamote, Alao, Loja, Salado, and Zamora, separated by structural limits represented by the regional fault systems Peltetec, Baños Front, Llangantes fault, and Cosanga Mendez fault. Regionally, the Paute Integral hydroelectric complex is located in the Alao terrain, formed in a middle Jurassic oceanic island arc environment. It is assumed to be largely covered by extensive Plio-Pleistocene volcanic deposits, which cover much of the Ecuadorian Andes. Specifically, the hydroelectric complex is located within the Alao Paute Unit and El Pan Unit (as part of the Alao terrain). The Alao Paute Unit (which is where the Guarumales landslide lies) is made up of meta-andesites, volcanic agglomerates, tuffs, and green rocks that have developed pelite and schist facies. The structural features present regional lineaments and plans of foliation oriented to the NNE-SSW diving towards the NW (Litherland et al., 1994). A detailed geological map of the region is presented in Figure 2.1.

Locally, the Guarumales landslide is composed of two litho-stratigraphic sequences, as described later in this study. The altitude of the Guarumales landslide varies from 1300 to 1700 m.a.s.l. and the slopes range from 0° to >45°, with an average of 20°. The vegetation is considered as lower mountain rain forest, with (smaller) trees similar to those in the lowlands. Generally, the buttresses and stilt roots on trees are infrequent or non-existing (Gupta, 2011; Luteyn and Churchill, 2000). However, it is observed that, in some locations of the Guarumales slope, anthropogenic disturbances have changed the land cover and land use (e.g., the construction of the electrical corporation of Ecuador (CELEC)'s headquarters, irrigation, and cattle grazing on the south of the slope). Other locations

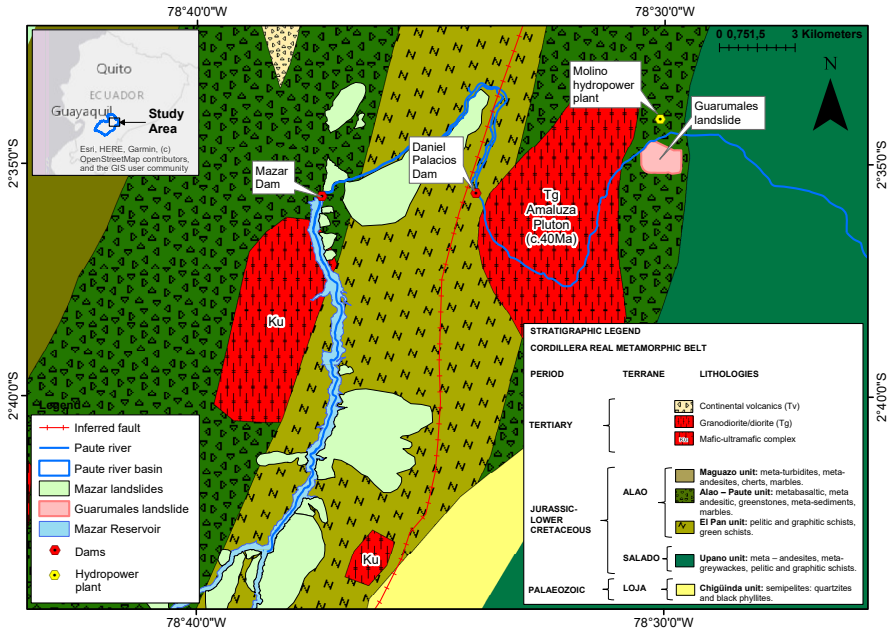


Figure 2.1: Geological map of the Paute Integral hydroelectric complex

in the Ecuadorian Andes show similar anthropogenic disturbances (e.g., Molina et al. (2015); Jokisch and Lair (2002)).

The mean annual rainfall is around 3000 mm/year measured at the Guarumales station from 2013 to 2018, with a standard deviation of ~200 mm/y. The Amazonian regime influences rainfall. The wettest season is from April to August, with 52% of the rainfall occurring during five months, and the somewhat drier season is between September and March, with 48% of the rainfall spread over seven months.

The Guarumales landslide endangers one of the most important hydropower plants of Ecuador: the Molino hydropower plant of the Paute Integral hydroelectric complex with an installed capacity of 1100 MW. The administrative facilities of Molino are located on the Guarumales landslide, where an average of 250 people live. Most of them are employees of CELEC EP (Electrical corporation of Ecuador public company). Instrumentation and essential infrastructure are located on the landslide (Figure 2.2).

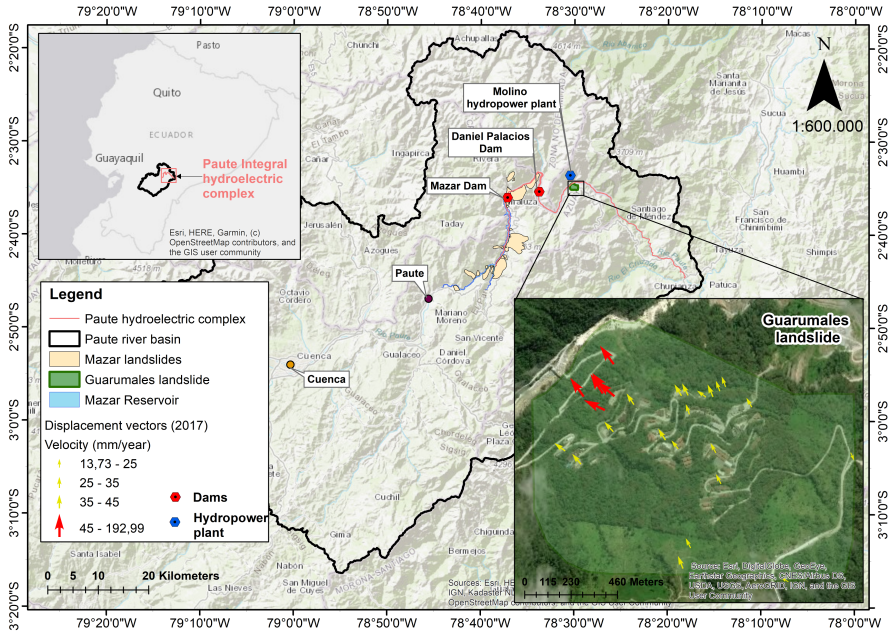


Figure 2.2: Location of the 21 landslides around Mazar and Molino hydropower facilities, including the Guarumales landslide

2.3. METHODOLOGY AND DATA AVAILABILITY

For this study, three geological cross sections were made in Guarumales: A-A', B-B', and C'-C. These were constructed from data collected during the drilling campaigns carried out from 2016–2018 and corroborated by historical data before 2016. Two of the stratigraphic columns used to construct these profiles can be seen in Figure 2.3. A stratigraphic correlation was used to construct the local stratigraphic sections.

Data for the surface displacement were from 2001 to 2018 and were collected monthly using total stations with 6 and 5 s of precision from 2010 to 2015, and since 2015, respectively, from a fixed reference point located on the opposite slope ($2^{\circ}34' S$, $78^{\circ}30' W$). As a result, the spatial coordinates (x, y, z) of 26 fixed points located on the Guarumales landslide were obtained and labeled as indicated in Table 2.1. The cumulative horizontal displacement per observation point was determined to evaluate the slope displacement. We determined the accuracy of the measurements by comparing the residuals (using the total least

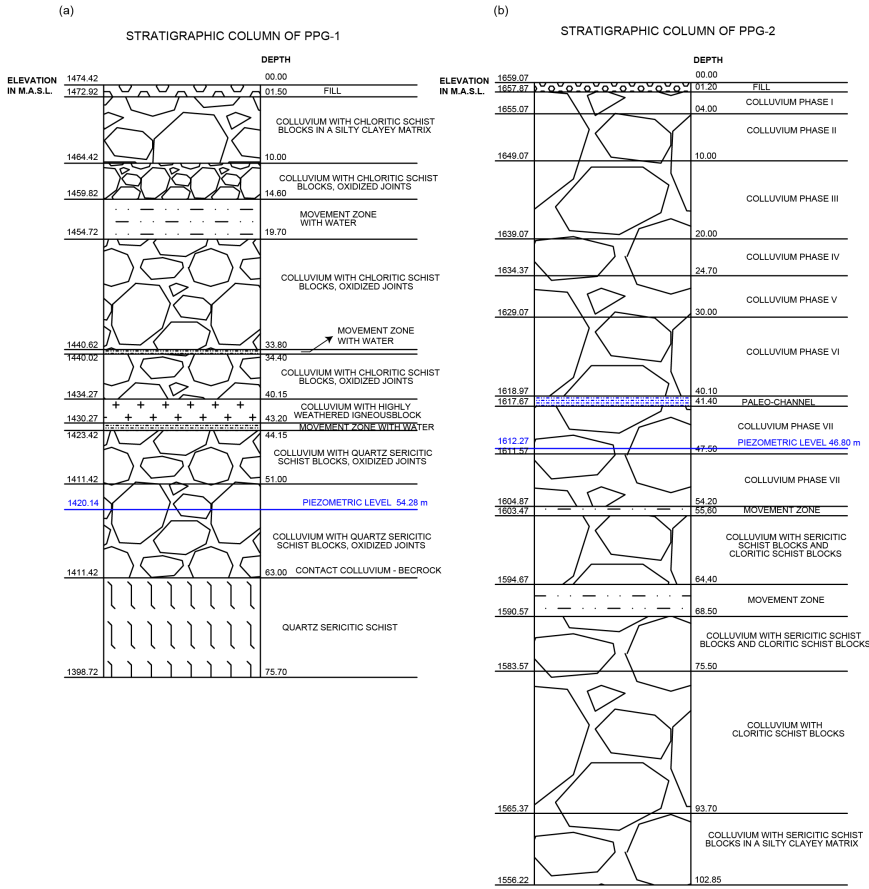


Figure 2.3: Stratigraphic columns for boreholes PPG-1 (a) and PPG-2 (b)

squares method (Golub and Van Loan, 1980)) between the geodetical measurements and the azimuth of movement (for horizontal displacement), to the annual horizontal displacement.

A meteorological station was located south of the landslide (2°34' S, 78°29' W), where rainfall and evaporation data were collected daily from 2013 to 2018. Missing rainfall data were substituted by using the climatological mean of the day of the missing data, with an error of 4 mm per day (Guerrero, 2018), while the evaporation was calculated using the Penman–Monteith equation directly by the sensor using temperature, solar radiation, among other variables.

Groundwater level data were collected manually at 11 piezometers twice per

month for the period of 2013 to 2018. For this study, 11 piezometers were evaluated (see [Table 2.1](#) for the labels and depth information).

Horizontal drains were drilled and installed in the landslide in 1994, in order to reduce the groundwater recharge in the slope ([Ramon, 1997](#)). In this study, the analyses were carried out using data from 2013 to 2018. Out of these, 29 were operational and formed four groups over the landslide, as indicated in [Table 2.1](#). The drain discharges were measured daily, weekly, and monthly using a graduated container. Their length varied from ~30 m to ~150 m.

We analyzed how the groundwater levels and drain discharges were affected by rainfall and reference evaporation ([Bakker and Schaars, 2019](#)) using transfer function noise (TFN) modeling as implemented in the Python package *Pastas* ([Collenteur et al., 2019](#)). In general, TFN modeling was used to identify the different stresses (or forcings) that cause the input time series (e.g., head values) to fluctuate or respond. Impulse response functions were estimated to explain a time series (piezometric level and discharge from drains) based on one or more forcings (rainfall and evaporation) ([Collenteur et al., 2019](#)). Outliers in the groundwater data were identified and removed using the approach of [Peterson et al. \(2018\)](#) before the analysis.

The electrical conductivity was measured at 18 points once per week since 2018, using a multi-parameter water quality meter (Horiba U-50 series). We sampled 10 points from surface water bodies and 8 representative points from drains (1–3 per group of drains), as indicated in [Table 2.1](#). Boxplot diagrams were used to assess the electrical conductivity. These were compared to each other and to the typical values found in the literature to determine likely water sources.

The Brönnimann classification system ([Brönnimann, 2011](#)) was used to provide a conceptual assessment of the possible hydrogeological mechanisms influencing mass movement. This system uses the permeability contrast between slope layers (high and low permeable) and the degree of saturation of the layers (unsaturated, saturated, and confined). [Figure 2.4](#) shows all possible combinations of these two parameters. The interpretations that come from analyzing the rainfall, groundwater variations, and drain discharge were linked to the geology and the spatial distribution of the measured surface displacement of the site.

An overview of the available instrumentation and locations is shown in [Fig-](#)

Table 2.1: Instrumentation in the Guarumales landslide used in this study

Monitoring Points	Quantity	Labels
Surface displacement	26	T4, T18, PEG3, PI3, PI5, PI6, PI9, PI10, PI11, PI12, S1, S2, S3, T9, T10, T11, T12, T13, T14, T8, T16, PI7, T17, T19, T20, and PI2.
Piezometric levels (with the depth of the borehole)	11	PP4A (43 m deep), PP4B (43 m deep), PEG3 (47 m deep), PI11 1 (44 m deep), PP2A (77.5 m deep), PP2B (77.5 m deep), PI4 1 (30 m deep), PI3 1 (41 m deep), PI10 1 (40 m deep), PI2 1 (50 m deep), and PP3A (~50 m deep).
Horizontal drains	29	Group 1 (5 drains: 1.1, 1.2, 1.3, 1.4, and 1.7), Group 2 (15 drains: 2.0, 2.1, 2.2, 2.3, 2.4, 2.5, 2.6, 2.10, 2.11, 2.12, 2.14, 2.15, 2.16, 2.17, and 2.18), Group 4 (6 drains: 4.1, 4.2, 4.3, 4.4, 4.5, and 4.6), and Group 6 (3 drains: 6.1, 6.2, and 6.3).
Horizontal drains depth		1.1: 47 m, 1.2: 46 m, 1.3: 53 m, 1.4: 30 m, 1.7: 50 m, 2.0, 2.1: 23 m, 2.2: 29 m, 2.3: 37 m, 2.4: 25 m, 2.5: 21 m, 2.6: 18 m, 2.10: 33 m, 2.11: 12 m, 2.12: 21 m, 2.14: 34 m, 2.15: 27 m, 2.16: 43 m, 2.17: 34 m, 2.18, 4.1: 20 m, 4.2: 19 m, 4.3: 13 m, 4.4: 18 m, 4.5: 16 m, 4.6: 34 m, 6.1: 26 m, 6.2: 28 m, 6.3: 27 m.
Electrical conductivity	18	From surface water bodies (10 locations: CA-1, CA-3, CA-4, CA-5, CA-11, CA-12, CA-14, CA-15, CA-16, and CA-17) and from drains (8 locations: 1.4, 2.0, 2.5, 2.17, 2.18, 4.2, 4.5, and 6.1)

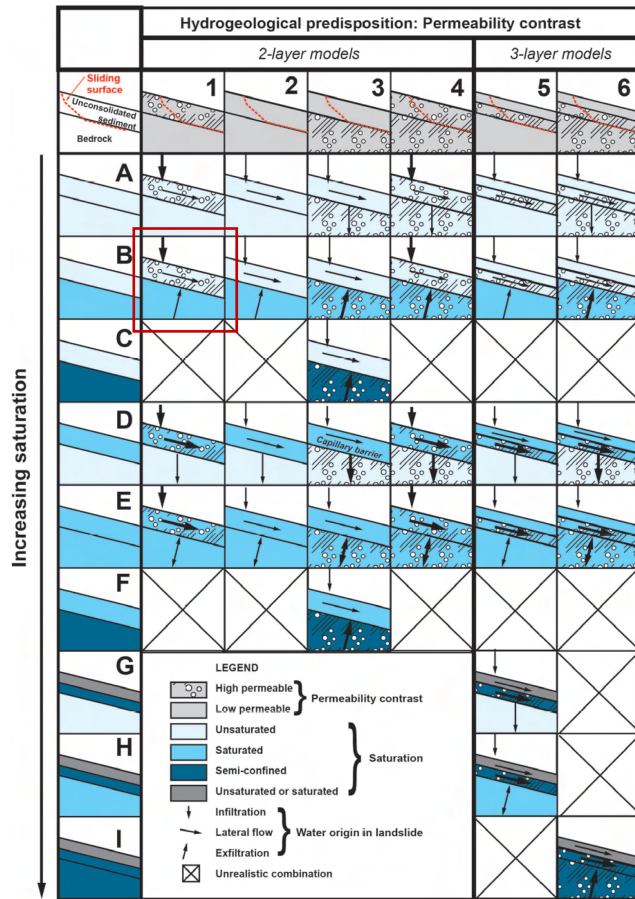


Figure 2.4: Hydrogeological classification for landslides, from Brönnimann (Brönnimann, 2011). Reproduced with permission from Laurent Tacher, Thesis: Effect of groundwater on landslide triggering; published by EPFL, 2011

ure 2.5.

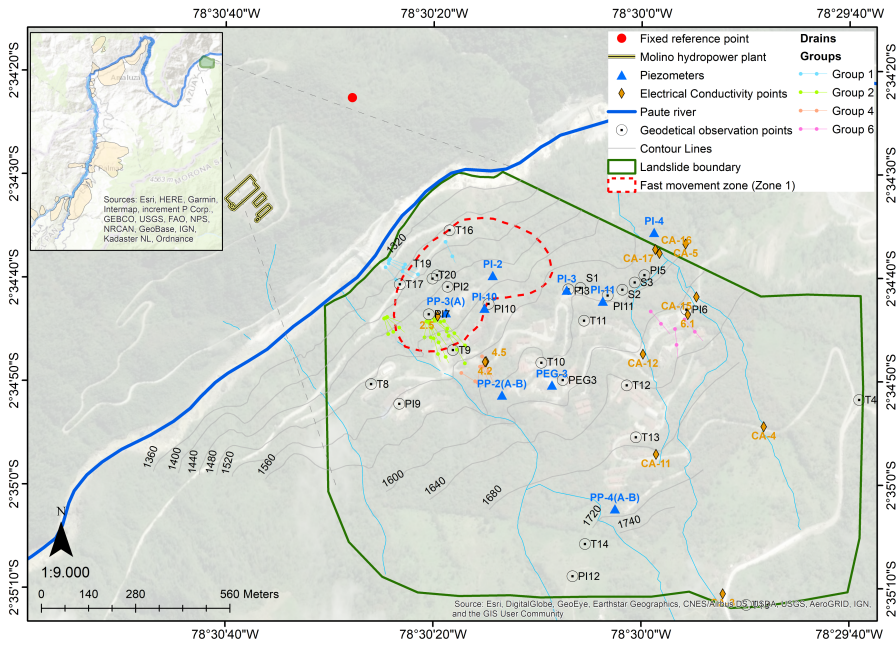


Figure 2.5: Instruments available in Guarumales and their location

2.4. RESULTS

2.4.1. GEOLOGY

The Guarumales landslide contained two main litho-stratigraphic units:

Unit 1—Bedrock: Undifferentiated metamorphic rock of Paleozoic–Mesozoic age, with intercalations of sericitic, chloritic, graphitic, and metavolcanic schists (shale). This lies below a slip surface composed of grey clay, containing angular clasts to sub-angles of chloritic, sericitic and graphitic schists.

Unit 2—Colluvium: Overlying the slip surface, a thick (20 to 100 m) heterogeneous colluvium layer, consisting mainly of large chloritic, sericitic and graphitic shale clasts in a clayey silt to silty sand matrix. Furthermore, in the close vicinity of the Paute river, unsorted (sub-) rounded alluvial deposits were present (see Figure 2.6).

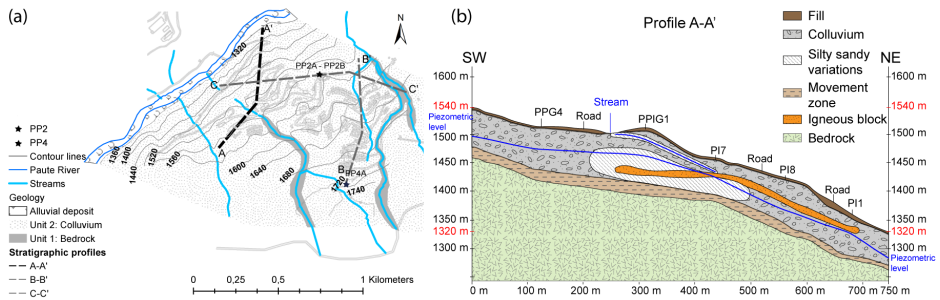


Figure 2.6: (a) Geological map of the Guarumales landslide, where two litho-stratigraphic units were identified. Unit 1: Bedrock, Unit 2: Colluvium, (b) Profile A-A' indicating the presence of the bedrock, clayey slip surface (that is located ~100 m deep), and a colluvium layer formed by shale blocks and silty sandy lenses. An igneous block was also found through the colluvium layer. Groundwater was present at two levels; one shallow presence that mainly originated in the sandy silt lens and another deeper (30 to 50 m deep) in the colluvium body. Profiles B-B' and C'-C are presented in Figure 2.7 and Figure 2.8.

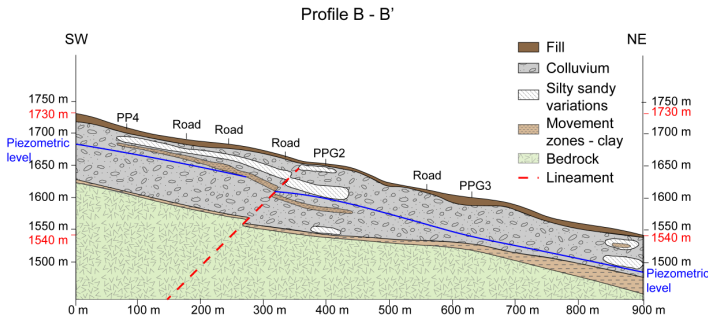


Figure 2.7: Stratigraphic profile B-B'

Several drilling campaigns were carried out from 2016 to 2018, and these were corroborated by data from before 2016. In addition to a deep, continuous groundwater level, a shallow groundwater level was found during the 2016–2018 drilling campaign in boreholes PP2 and PP4, suggesting that a perched groundwater level existed in a lens of sandy silt matrix, which seemed to link to small surface water streams present on the Guarumales slope (see Figure 2.6). Within the colluvium layer of profile A-A', a large igneous block was found, possibly associated with the granodioritic body of Amaluza (pluton of the Eocene age) (Litherland et al., 1994). This unit is present along the Paute river, in the lower part of the basin.

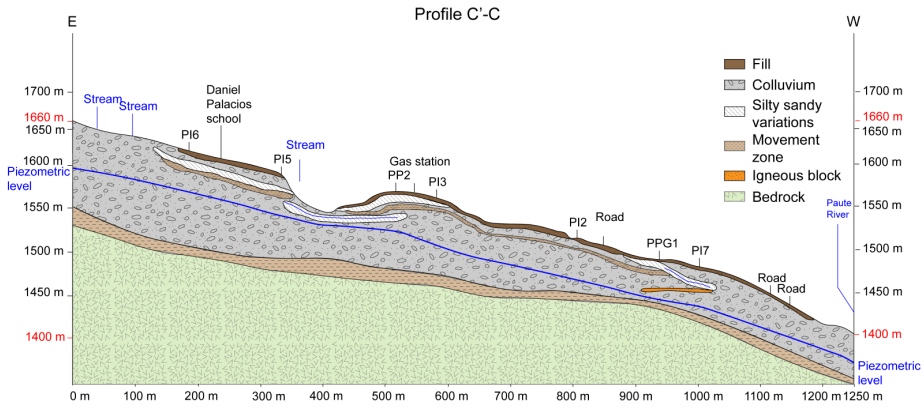


Figure 2.8: Stratigraphic profile C'-C

2.4.2. SURFACE DYNAMICS

Survey campaigns in Guarumales take place once per month, but there are interruptions due to weather conditions resulting in an average of eight measurements per year with a minimum of three measurements per year at the 26 geodetical observation points. There are two zones with distinct movement. Zone 1 (red dashed line in Figure 2.5) is located in the lower part of the landslide (N-W) and represents the fastest movement with horizontal velocities that can go up to 210 mm/year. Zone 2 (yellow) represents the rest of the slope where the horizontal velocities typically range from 30 to 60 mm/year and up to 150 mm/year (Figure 2.9a). The cumulative yearly horizontal displacement is plotted in Figure 2.9b.

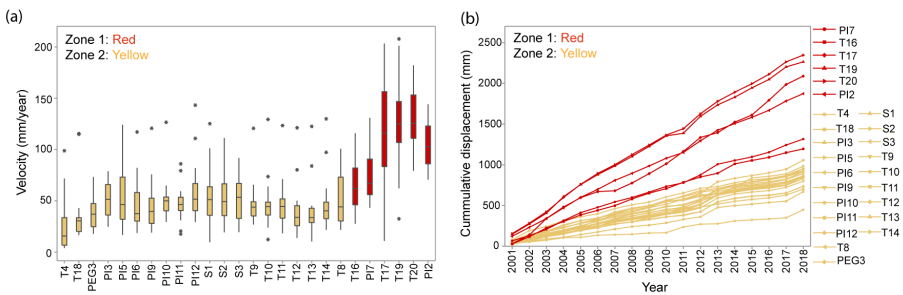


Figure 2.9: The horizontal displacement velocity of 26 geodetical observation points in Guarumales for 18 years, indicating Zone 1 (red, higher velocity) and Zone 2 (yellow, lower velocity). (a) Boxplots, (b) Cumulative horizontal displacement

The overall direction of the movement in all 26 points was northwest, with an azimuth that varied from 250 to 330 degrees (see [Figure 2.2](#)). The direction and magnitude of the velocity vectors of all individual observation points along the horizontal plane are presented in [Table 2.2](#) and [Table 2.3](#).

Table 2.2: The initial coordinates and horizontal displacement detected by 26 fixed points in Guarumales from 2001 to 2018

Point	Initial Coordinates (m)			Displacement (mm)																	Average	Accumulated	
	x	y	z	2001	2002	2003	2004	2005	2006	2007	2008	2009	2010	2011	2012	2013	2014	2015	2016	2017			2018
PEG3	7780060.63	9714664.70	15903.91	46.19	55.15	20.46	56.42	37.61	31.44	24.83	23.75	50.94	41.19	43.82	46.13	36.33	33.84	24.52	17.71	34.60	73.11	38.89	7006.05
P13	7780251.24	9715134.72	15563.52	66.21	78.41	36.39	78.81	52.80	32.69	50.21	62.42	41.65	52.87	63.87	66.25	24.60	47.50	34.83	24.95	38.44	65.64	51.04	918.76
P15	7780512.24	9715176.83	15403.81	18.98	83.36	54.38	42.23	40.59	78.65	71.21	46.30	45.62	66.10	16.76	46.52	33.11	69.83	124.20	19.77	28.73	96.17	38.73	982.54
P16	7783760.07	9715074.17	16009.79	50.80	56.79	25.84	49.93	33.47	61.88	18.71	39.47	37.11	37.39	22.95	73.40	117.09	37.59	31.62	18.76	33.68	82.10	46.03	828.58
P19	7775225.00	9714794.21	15317.4	33.85	37.18	53.14	30.50	42.20	43.37	57.99	38.66	25.86	28.67	52.41	120.74	48.68	22.85	19.11	40.63	75.70	44.30	797.39	
P10	7778784.84	9715091.17	1501.97	49.72	52.02	52.86	45.24	50.25	55.44	53.20	42.21	40.17	41.25	29.56	64.85	126.58	52.80	34.52	33.06	40.28	62.04	51.45	926.07
P11	778141.91	9715116.04	1551.38	50.35	86.01	43.39	53.42	43.73	44.53	52.48	44.00	53.59	43.97	59.24	52.61	17.65	48.31	31.00	20.45	31.79	79.38	47.55	855.91
P12	778037.53	9714282.10	17869.93	52.22	96.10	65.48	90.98	58.19	53.08	81.91	46.83	32.98	49.32	29.23	70.67	143.22	42.41	34.17	33.65	44.31	110.84	58.64	1053.58
S1	778061.23	9715138.95	15560.09	20.57	47.61	55.35	90.36	51.98	45.72	68.34	52.96	32.76	63.29	9.70	65.14	125.24	60.79	32.61	27.23	38.14	101.14	52.95	953.15
S2	778185.72	9715133.53	15507.6	78.28	111.23	49.84	73.11	47.32	37.36	64.40	46.51	32.76	63.68	49.50	55.00	21.33	48.99	32.09	19.23	36.45	87.24	53.02	954.29
S3	778222.45	9715155.27	15463.36	57.09	69.85	58.53	66.55	60.79	30.13	69.94	43.11	39.27	68.12	43.35	56.64	24.36	50.26	32.43	19.39	33.02	91.79	50.81	914.62
T9	777982.11	9714953.91	1512.26	46.35	40.54	51.25	40.19	45.66	47.26	48.30	27.78	40.02	42.17	29.45	56.63	120.66	47.98	28.75	26.88	37.23	65.65	46.82	842.75
T10	777944.87	9714916.40	1572.02	53.71	44.98	47.14	43.68	45.35	32.41	63.88	39.09	37.30	46.53	12.29	40.00	129.41	45.38	30.38	23.90	38.29	73.58	47.07	847.31
T11	778071.91	9715041.24	1585.34	51.87	45.46	49.45	43.52	40.06	52.02	51.14	33.19	45.86	34.77	32.54	67.23	123.38	39.63	29.60	18.23	32.87	71.18	47.89	861.99
T12	778195.74	9714694.28	1654.66	44.57	90.20	34.27	33.67	31.44	31.79	44.95	25.18	33.99	29.63	16.86	46.04	121.19	44.95	24.43	13.87	25.99	80.18	40.73	733.20
T13	778225.66	9714694.89	1678.90	45.32	42.23	29.26	40.33	32.62	34.71	44.49	30.03	26.20	31.35	27.46	39.27	122.58	40.32	25.21	10.53	29.67	83.91	40.86	735.46
T14	778074.50	9714377.62	1752.03	37.86	42.89	39.64	39.22	44.84	41.70	62.02	33.72	24.42	40.77	47.25	53.31	129.95	37.80	26.88	21.81	29.38	97.20	47.25	850.47
T4	778889.60	9714805.92	1823.11	35.49	17.49	19.50	31.24	3.91	24.97	7.03	6.14	13.76	4.35	71.79	33.08	5.56	34.98	13.33	11.29	13.73	98.83	24.80	446.47
T8	777438.58	9714852.99	1500.13	26.67	34.74	54.22	29.38	48.73	54.06	45.29	30.62	32.88	38.69	79.08	80.90	73.70	100.79	21.58	24.09	42.95	72.81	49.51	891.20
T18	778553.43	9714196.82	1892.91	29.78	26.63	32.96	19.24	32.61	32.41	34.97	31.47	17.42	28.02	42.89	31.14	115.01	22.79	18.18	20.39	16.62	115.49	37.11	668.01
P17	777610.35	9715060.41	1461.22	66.47	59.77	78.50	107.92	98.07	65.65	67.04	53.86	64.75	71.49	45.00	96.26	130.92	46.81	43.16	56.60	88.91	73.54	73.04	1314.72
T16	777671.99	9715308.82	1380.58	27.67	87.32	108.30	78.00	81.95	55.71	59.17	82.33	69.80	55.01	79.38	64.78	45.54	113.90	41.88	38.42	56.13	46.28	66.31	1193.57
T17	777524.25	9715149.42	1397.36	28.33	107.17	203.31	140.60	116.35	73.09	10.93	95.05	115.37	121.47	150.96	172.51	57.91	130.17	86.75	182.82	193.00	102.26	116.00	2088.06
T19	777634.77	9715175.96	1436.38	145.69	125.24	133.64	201.13	149.93	122.59	107.65	114.74	124.29	129.19	32.46	207.84	139.49	96.57	113.01	104.57	153.07	62.15	125.73	2283.23
T20	777621.50	9715166.31	1435.48	152.79	127.29	141.44	176.08	160.29	134.89	107.19	123.84	117.14	122.82	79.19	182.05	153.90	112.07	104.59	116.05	152.27	83.38	130.40	2347.28
P12	777866.36	9715141.99	1457.73	120.92	109.00	107.66	131.97	129.17	98.00	110.92	86.11	91.29	94.44	70.64	144.16	129.77	82.36	76.05	85.80	114.09	90.67	104.06	1873.01

Table 2.3: The initial coordinates and azimuth of movement detected by 26 fixed points in Guarumales from 2001 to 2018

Point	Initial Coordinates (m)				Azimuth (degrees)																		Average	
	x	y	z		2001	2002	2003	2004	2005	2006	2007	2008	2009	2010	2011	2012	2013	2014	2015	2016	2017	2018		
PE3	778008.63	9714664.70	1590.91	341.94	321.72	333.18	332.40	332.40	290.78	312.40	327.50	338.25	338.03	336.37	312.3	346.50	312.77	20.17	348.40	323.05	321.58	278.96	292.85	
P3	778025.19	9715134.72	1556.52	341.91	327.10	330.34	341.39	341.39	319.66	331.52	339.75	337.00	326.89	332.80	16.26	352.09	327.00	9.09	348.33	329.56	328.89	269.35	297.50	
P5	778025.24	9715176.83	1540.81	267.82	312.33	338.04	337.44	328.73	329.84	327.82	343.36	286.00	344.31	220.66	314.60	329.29	3.59	35.80	311.72	328.52	227.68	277.71	277.71	
P6	778376.07	9715074.17	1609.79	307.47	322.07	350.30	329.22	309.98	334.79	307.57	323.90	339.16	318.69	200.18	343.62	33.30	17.30	351.38	325.82	330.01	263.06	286.85	286.85	
P9	777522.50	9714794.21	1531.74	321.45	314.96	346.28	319.10	320.58	332.46	337.26	344.78	310.33	328.47	226.78	301.07	29.64	40.66	349.73	328.41	319.85	281.64	288.37	288.37	
P10	777878.84	9715091.17	1501.97	315.11	323.42	353.07	317.43	328.58	337.21	335.18	342.88	312.81	333.33	256.21	316.59	29.96	15.03	347.44	332.73	326.52	264.19	290.94	290.94	
P11	778141.91	9715116.04	1551.38	196.94	318.36	338.36	334.25	314.75	337.71	337.27	337.80	341.01	21.69	17.59	9.81	312.88	5.19	347.80	318.75	306.33	262.64	247.90	247.90	
P12	778037.53	9714282.10	1786.93	337.53	339.81	345.56	333.32	326.15	346.48	339.26	338.17	335.33	336.49	210.71	327.00	25.07	15.20	351.03	342.58	338.65	322.19	297.94	297.94	
S1	778061.23	9715138.95	1556.09	287.32	323.80	348.16	325.67	330.05	343.31	343.07	343.88	322.19	325.21	67.14	317.25	30.02	14.45	349.79	332.69	333.84	270.06	279.40	279.40	
S2	778185.72	9715133.53	1550.76	176.99	304.27	355.14	349.45	317.58	333.10	333.79	349.58	296.17	350.55	14.91	2.74	324.67	4.53	346.01	320.47	336.37	238.71	261.07	261.07	
S3	778222.45	9715155.27	1546.36	172.17	292.50	332.17	347.07	327.98	310.71	316.84	347.38	335.66	332.63	320.70	327.45	220.29	308.28	30.12	27.23	347.22	329.09	318.07	274.22	287.23
T9	777682.11	9714953.91	1512.26	301.39	322.39	350.89	313.61	316.84	347.38	347.54	347.54	333.66	332.63	320.70	327.45	220.29	308.28	30.12	27.23	347.22	329.09	318.07	274.22	287.23
T10	777944.87	9714916.40	1527.02	310.38	316.23	349.52	319.98	320.51	358.54	323.79	330.74	330.46	329.76	261.32	287.30	24.87	23.49	348.90	330.70	328.17	276.87	289.82	289.82	
T11	778071.91	9715041.24	1585.34	316.51	318.21	356.99	322.66	325.76	338.86	342.92	325.47	338.29	326.18	230.90	346.87	31.34	14.67	349.86	335.60	340.60	266.98	293.65	293.65	
T12	778198.74	9714849.28	1654.86	296.45	327.41	357.37	333.89	310.05	330.33	340.37	330.36	330.04	325.63	198.11	323.64	33.00	28.70	357.12	321.72	331.22	278.25	288.39	288.39	
T13	778225.66	9714694.89	1678.90	319.42	336.11	351.86	345.72	289.14	343.58	335.44	333.85	331.29	342.21	198.62	321.75	31.72	32.60	4.24	313.58	332.86	288.72	274.19	274.19	
T14	778074.50	9714377.62	1752.03	319.20	351.88	330.65	346.46	338.46	336.57	340.41	339.06	315.66	344.70	191.31	325.78	28.87	27.05	0.17	334.72	333.52	313.74	276.42	276.42	
T4	778889.60	9714805.92	1823.11	26.53	328.51	198.46	6.06	204.64	161.34	234.05	61.74	5.36	175.66	28.53	69.90	152.51	56.90	35.23	151.16	156.55	271.41	135.62	135.62	
T8	777438.58	9714852.99	1500.13	308.93	305.84	344.99	310.03	320.04	340.33	317.57	341.48	315.59	322.91	231.42	269.06	18.12	41.68	347.90	336.15	306.31	278.69	281.92	281.92	
T18	778533.43	9714196.82	1892.91	359.14	303.30	314.99	296.83	315.97	329.82	300.04	297.98	313.24	321.44	193.36	284.86	31.59	37.98	341.75	303.14	306.44	311.62	276.82	276.82	
P17	777610.35	9715060.41	1461.22	304.29	310.47	344.76	309.24	316.41	323.09	329.02	321.21	313.94	323.30	311.42	25.05	2.37	331.38	307.57	295.61	277.10	281.59	281.59	281.59	
T16	777671.99	9715309.82	1380.58	178.85	332.05	333.34	342.48	327.98	333.53	313.43	342.29	336.99	332.41	328.68	349.62	254.72	5.15	320.61	324.08	323.33	315.08	301.30	301.30	
T17	777524.25	9715149.42	1397.36	232.57	338.04	333.99	336.97	318.22	317.92	286.31	324.92	337.51	326.79	335.59	330.77	274.92	336.09	326.37	323.51	324.32	321.77	319.64	319.64	
T19	777634.77	9715175.96	1436.38	304.09	339.58	320.30	327.17	329.51	332.69	332.69	324.89	337.51	312.37	324.38	323.69	5.68	338.95	323.39	322.48	321.33	294.11	306.31	306.31	
T20	777621.50	9715166.31	1435.48	304.72	322.90	337.56	323.41	320.83	330.54	334.72	324.28	323.11	320.14	329.19	315.00	9.62	349.32	332.54	320.83	327.98	294.29	308.29	308.29	
P2	777666.36	9715141.99	1457.73	300.77	311.83	330.92	305.92	311.92	324.22	317.58	316.73	308.48	315.31	288.48	308.60	10.17	344.86	316.99	311.01	310.52	277.41	296.56	296.56	

The annual horizontal velocity of all 26 observation points is presented for each year in [Figure 2.10a](#). On average, the velocity was around 50 mm/year, which mostly corresponded to the behavior of zone 2. The higher displacement rates (expressed here as outliers) corresponded to observation points in zone 1 with velocities up to 200 mm/year in some years. In 2013, the velocities ranged from 0 to 150 mm/year with no anomalies that corresponded to Zone 1. In [Figure 2.10b](#), a plan view of the evolution of the horizontal movement over 18 years is shown for PI3. It is clear that in 2013, there was a dramatic shift in the displacement; however, the effect vanished after one or two years, as the movement returned to a northwest direction.

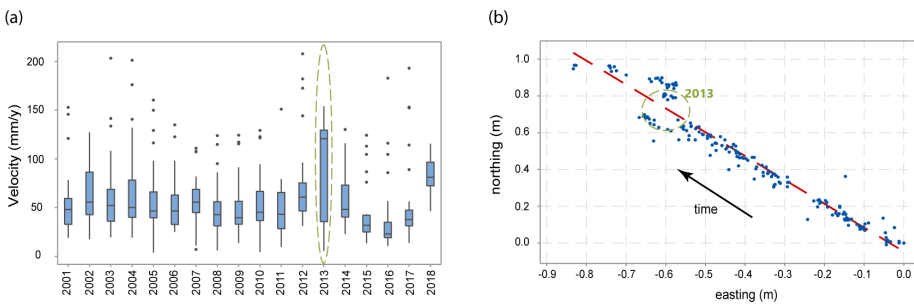


Figure 2.10: (a) Boxplots of the average annual horizontal displacement velocity of 26 geodetical observation points for 18 years. (b) Plan view of the evolution of the horizontal movement from 2001 to 2018, with the respective trendline for observation point PI3

The residuals between the observed locations and the trendline (i.e., the azimuth of movement for the horizontal coordinates), as in [Figure 2.10b](#) for PI3, were calculated. These results were compared to the average horizontal displacement per year to obtain the normalized residuals. This revealed that the residuals for zones 1 and 2 were ~ 1.7 and ~ 3.5 (up to six) times the average yearly displacement, respectively. To determine a reliable displacement and velocity, it was necessary to average at least 2–3 years of data to overcome the residuals. This can be seen in [Figure 2.11](#) and [Figure 2.12](#).

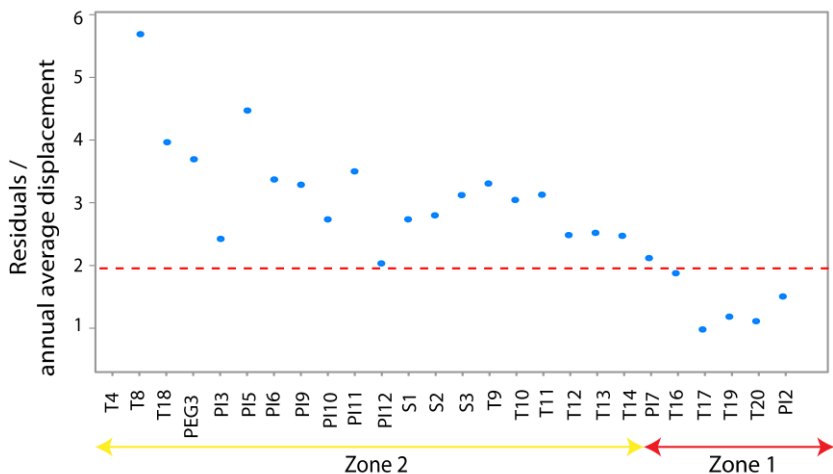


Figure 2.11: Residuals compared to the horizontal annual average displacement for the 26 geodetical observation points

2.4.3. HYDRO-METEOROLOGICAL ANALYSIS

The hydro-meteorological data are summarized in Figure 2.13. The mean annual rainfall was around 2937 mm per year. The years 2015 and 2013 were the wettest and driest years, with 3144 mm and 2607 mm of rainfall, respectively. The mean monthly rainfall ranged from 237 mm/month to 470 mm/month (Figure 2.13a). The wet season occurred from March to July. During the dry season, the lowest recorded monthly rainfall was 25 mm/month. The rainfall and discharge from the drains increased during the wet season (Figure 2.13a,c), while the evaporation increased during the drier season (Figure 2.13b). A time lag was always observed between the groundwater level rise (here for PP4A, depth: 43 m) and the rainfall.

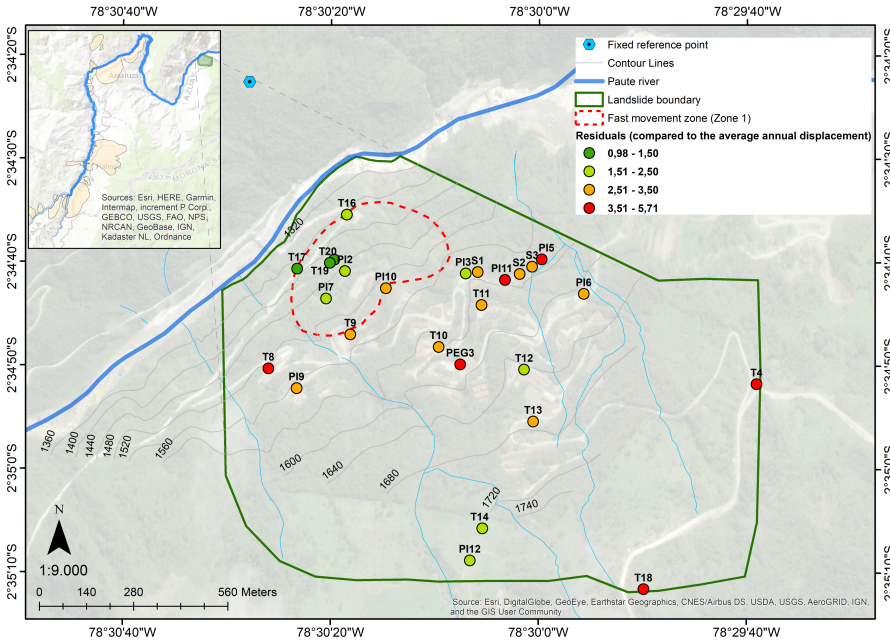


Figure 2.12: Plan view of the residuals compared to the annual average displacement in Guarumales

We analyzed the response of the groundwater levels to rainfall and evaporation. We applied transfer function noise modeling with response functions using the Python package Pastas (Bakker and Schaars, 2019; Collenteur et al., 2019). First, we attempted to analyze the measured groundwater levels using rainfall and reference evaporation as stresses (forcings). The results of the analysis showed that evaporation did not have a significant effect on groundwater levels, and the estimated parameters had high uncertainty. Next, the groundwater levels were analyzed with rainfall as the only stress causing groundwater fluctuations. The results were almost identical regarding Coefficient of Determination R^2 , and the parameters were estimated with much less uncertainty.

All 11 piezometers were analyzed, and three of them (PP2A, PP3A, and PP4A) showed a R^2 higher than 0.65, indicating that measured groundwater levels in these piezometers could be analyzed reasonably well using rainfall as the only stress. The resulting response functions for these three piezometers are shown in Figure 2.16.

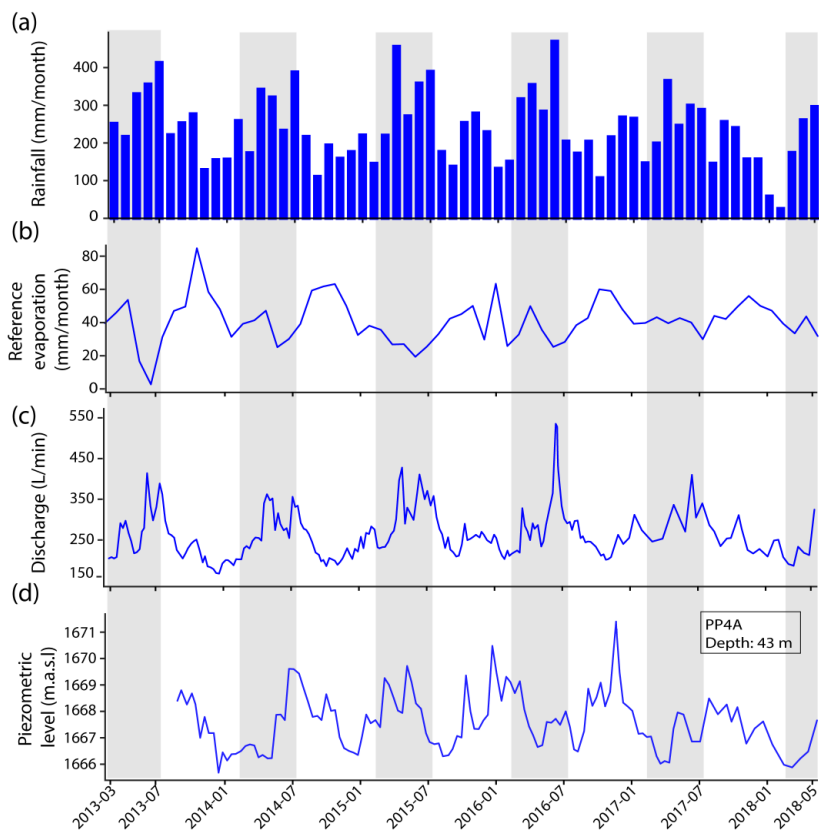


Figure 2.13: Time series of the (a) monthly rainfall, (b) monthly reference evaporation, (c) total discharge from 29 drains, and (d) piezometric level from the piezometer PP4A for the period 2013–2018. The shaded area indicates the rainy season. Time series plots for the ten remaining piezometers and the individual 29 drains are shown in [Figure 2.14](#) and [Figure 2.15](#).

The impulse response represents the response of the groundwater level to an instantaneous recharge event of 1 mm/day ([Figure 2.16a](#), dashed lines). The response time is defined here as the time when the impulse response reaches a peak, which represents the time lag between the rainfall event and the maximum groundwater response. The optimal value of the response time was estimated together with a 95% confidence interval. The peak response in PP2A was ~ 0.005 m, and the response time (time lag of the peak) was ~ 16 – 31 days. The peak response in PP3A was 0.008 m after ~ 1 – 12 days, and the peak response in PP4A was ~ 0.01 m after ~ 5 – 13 days.

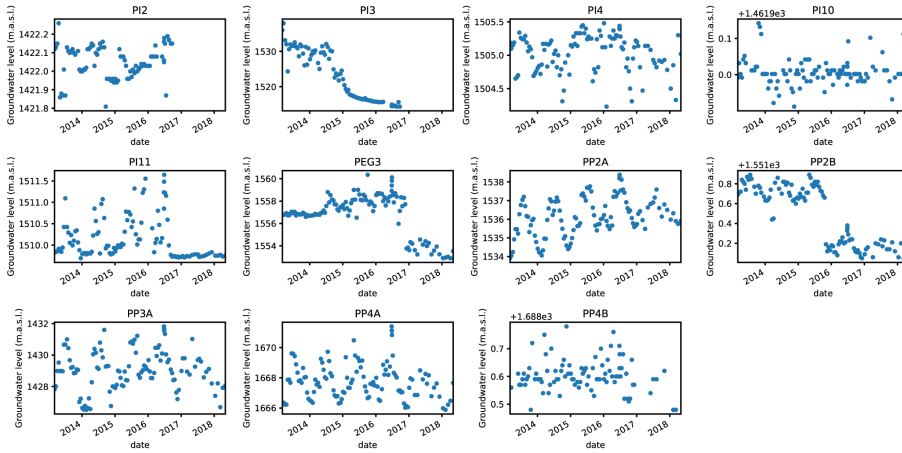


Figure 2.14: Time series plot of 11 groundwater observation points. Of the 11 piezometers, only 3 had meaningful results in the time series analysis. Out of the 11, 10 showed significant fluctuations; however, those could not be linked via the (simple) time series analysis to meteorological forcing. However, the fluctuations were in the same order of magnitude.

The step response represents the level to which the head rises in response to a continuous recharge of 1 mm/day (Figure 2.16b). The time it takes for the response to reach its plateau is called the memory of the system. Inversely, the memory of the system represents the time it takes for the effect of an impulse of rain to vanish. The optimal value of the memory was estimated together with a 95% confidence interval. In PP2A, the step response leveled off at ~ 0.35 m, and the memory was ~ 71 – 147 days. In PP3A, the step response leveled off at ~ 0.5 m after ~ 59 – 221 days, and in PP4A, the step response leveled off at ~ 0.35 m after ~ 41 – 76 days.

The same procedure was applied to the 29 drains located on the slope, and we attempted to analyze the measured discharge using time series analysis and rainfall as the stress. Discharge from individual drains was difficult to analyze, likely due to the relatively low discharge rates of the individual drains. Next, we attempted to analyze the cumulative discharge of each group of drains (groups 1, 2, 4, and 6 in Figure 2.5). The analysis for groups 2 and 4 resulted in a R^2 value larger than 0.65, indicating that cumulative drain discharge could be analyzed reasonably well using rainfall as the only stress. The impulse response functions for the drain discharge are shown in Figure 2.16a (continuous lines). Not surpris-

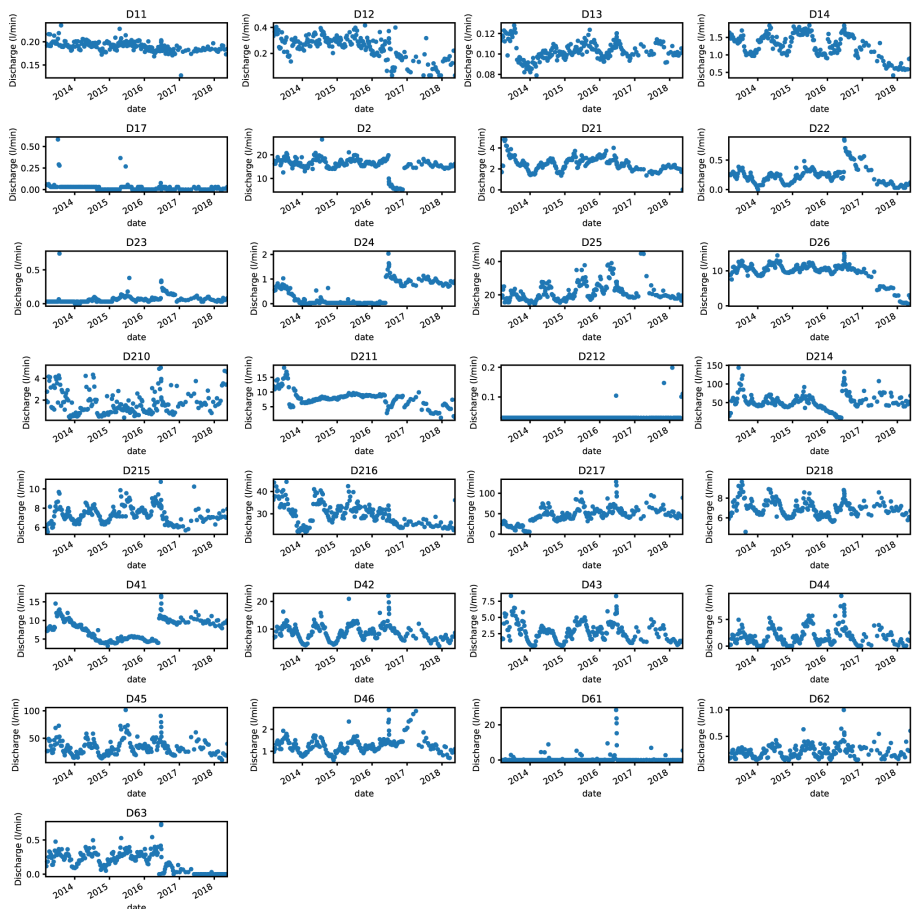


Figure 2.15: Time series plot of 29 monitored drains

ingly, the drain response was faster than the groundwater response. A response of 0.5 L/min and a response time of ~2–5 days was obtained for Group 2 (DG2), while a response of 0.25 L/min and a response time of ~1–4 days was obtained for Group 4 (DG4).

The electrical conductivity was tested in 18 locations across the slope and is shown in Figure 2.17. Values from the samples collected from the surface water bodies and drains were similar, ranging from ~20 $\mu\text{s}/\text{cm}^2$ to ~90 – 100 $\mu\text{s}/\text{cm}^2$ (see Figure 2.5). These values are typical for rainfall water. The variation of the electrical conductivity values was larger in the surface water bodies than in the drains.

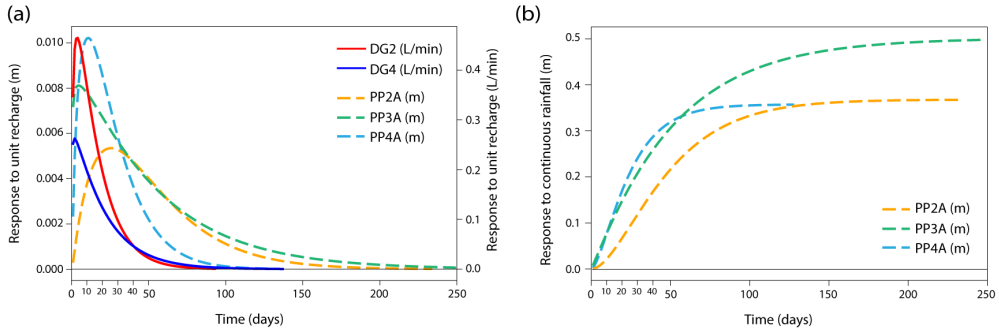


Figure 2.16: The impulse responses (a) for piezometers PP2A, PP3A, and PP4A, and drain groups 2 (DG2) and 4 (DG4); and the step responses (b) for piezometers PP2A, PP3A and PP4A

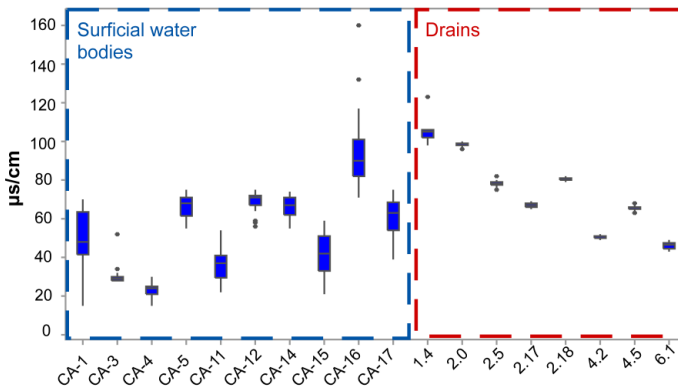


Figure 2.17: The electrical conductivity for 18 observation points in the slope for the period July–December/2018

2.5. A HYDROGEOLOGICAL CONCEPTUAL MODEL OF GUARUMALES SLOPE

Guarumales is a deep-seated landslide in a local complex geological setting. Here, we use the Brönnimann classification system to interpret the hydrogeological characteristics of the slow-moving landslide (Figure 2.4). Based on all observations, we simplified the landslide in a two-layer slope composed of a relatively permeable and mainly unsaturated colluvium layer and a low permeable, saturated bedrock layer with a 1–3 m thick weak layer acting as slip surface between the colluvium and the bedrock. Furthermore, we observed a delayed but distinct

correlation between the rainwater input and groundwater response of the unconfined aquifer in the slope. The heterogeneous nature of the colluvium and bedrock layers, highly fractured and weathered in some locations while intact in others, added complexity, including local perched water tables. Lastly, we found that the drains in the slope did not tap into the deeper groundwater system but drained the perched areas of the otherwise unsaturated top layer. This places the Guarumales slope in hydrogeological class B1 (see Figure 2.4), mainly influenced by local infiltration and percolation processes, free-draining into the Paute river at the toe of the slope, and with limited influence from the deep regional groundwater flow (Figure 2.18).

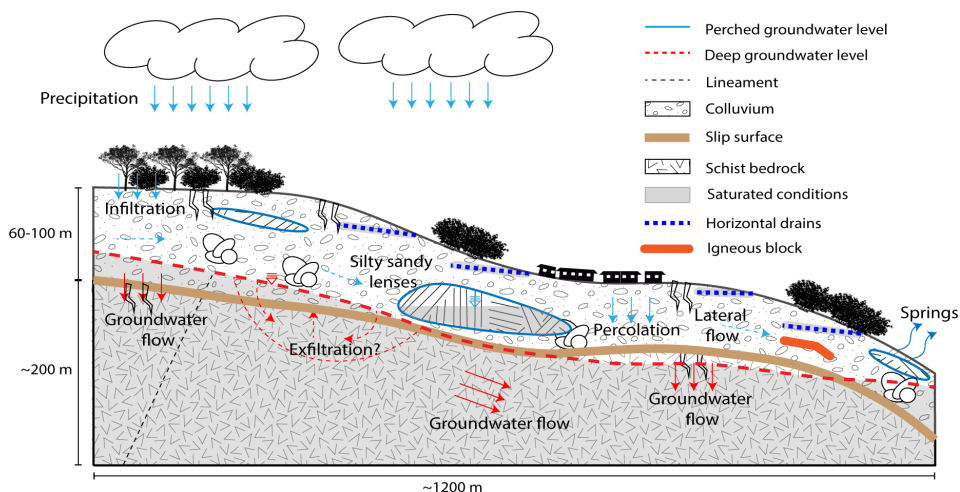


Figure 2.18: Conceptual model of the Guarumales landslide. There is a deep permanent groundwater level that varies around the slip surface, with scattered perched groundwater systems in silty sandy lenses overlaid by low permeable blocks. The Guarumales slope is an unconfined system, which means there is no pressurized water and very limited upward flow of water. There are 29 horizontal drains, which do not reach the deep groundwater systems but drain small perched water bodies in the slope, which are fed by rainfall, as also evidenced by the very low electrical conductivity of the drained water

In terms of comparing the displacement to hydro-meteorological factors, we concluded from the data shown in Figure 5b that no seasonal signal in the displacement could be determined due to the coarse time resolution and measurement error, which means that no relation could be established between the rainfall and displacement at this stage.

2.6. DISCUSSION

In this study, we analyzed the role of predisposing conditions and triggering factors on the stability of the Guarumales landslide. Eighteen years of displacement measurements showed that the yearly surface displacement rates were constant over time. While rainfall was shown to strongly influence the unconfined groundwater system with a ~1–31 days response time, no monthly variations in the horizontal displacement rates were observed with our displacement data. There were some areas where secondary shallow landslides and debris flow happened on top of the deep-seated, slow-moving landslide, and these were intensified during high-intensity rainfall, blocking small streams and roads in Guarumales (Vásconez, 2000). These movements occurred on a short time scale and could not be detected by the current monitoring system. Therefore, it was not possible to link this behavior to the proposed triggering factors.

The slow-moving behavior of the Guarumales landslide and its spatial distribution showed a constant annual deformation rate over 18 years, based on (bi-) monthly surveys. This was also reported by others (ECUAELECTRICIDAD, 2000a,b; Robles, 2000; CELEC-EP, 2011; Villacis and Robles, 2015; Robles et al., 2016). However, the limited subsurface information did not allow for detailed geological or geotechnical interpretation of the spatially distributed character of the Guarumales landslide. The deformation patterns did not link with the measured groundwater levels. The different compositions of the lithology and the depths of the slip surface (30 to >90 m) may influence the movement patterns of the slope. Therefore, geophysical monitoring in Guarumales could be a useful tool to identify subsurface structures.

Two additional limitations were identified with the 18 years of geodetical data. First, the limited temporal resolution of, on average, eight measurements per year, was insufficient to identify small accelerations and decelerations of surface displacement following the groundwater response to rainfall, if present. This is especially important as our analyses showed that groundwater fluctuations were correlated with rainfall with a response time of the maximum head after rainfall of ~1 to 31 days, and an increased head that lasted ~40 to 220 days. Second, the geodetical accuracy (1–5 cm) was low compared to the measured displacement (1 to 10 cm/year), which complicated the interpretation of the re-

sults. For most of the landslide, multi-annual displacement was required to assess the displacement magnitude and direction, which made it impossible to link the displacement to potential driving processes such as specific rainfall periods. To unravel the transient behavior of the Guarumales landslide, we need higher frequency and more accurate displacement measurements, which may be obtained with real-time kinematic global positioning systems (RTK-dGNSS).

In 2013, a shift in the direction of movement was found in all surface monitoring points in Guarumales. What influenced this directional shift is not clear. The cause could be related to a displacement of the fixed reference point on the other side of the valley from where the geodetical measurements were taken. Alternatively, it could be related to high seismic activity in the study area where the number of seismic events (115), with a magnitude above 4 Mb (body-wave magnitude), was higher in 2013 than in other years (Córdova et al., 2014). The additional lateral forces would have weakened the soil by reducing its shear strength. Additionally, an alteration of the drainage system at the toe of the landslide through the reinforcement of an existing retaining wall was conducted in 2013, which may have resulted in a temporary direction shift of the overall movement. The excess of water that built up at the toe of the slope was unable to drain properly, and this groundwater accumulation, which was evidenced in the springs found at the toe of the slope, decreased the stability of the slope. After the modification of the retaining walls, water may have found a new way to drain towards the river, resulting in a normalization of the movement to the north-west direction.

The 2016–2018 drillings revealed that the slip surface of the Guarumales landslide was situated between 30 m and >90 m below the ground surface. This is deeper than was reported previously (Vásconez, 2000; Charpentier, 1996; Vásconez and Vásconez, 2001) based on the analysis of inclinometer data from eight inclinometers located in the landslide, in the periods of 1994–1996, 1994–1998, and 2000–2001, respectively. Recent explorations revealed that large blocks (~20 m in diameter), abundantly present in the colluvium layer, were mistakenly considered as bedrock. This misunderstanding led to relatively shallow drillings, and inclinometers were installed with their lowest point fixed in the moving block instead of in the stable bedrock, which compromised the inclinometer results.

The observed groundwater level fluctuations of ~0.6 m to ~4 m at Guaru-

males were small compared to the depth of the slip surface (~30 m to >90 m). With a groundwater depth of 30 m, a 1 m groundwater level rise equals a relative increase in pore pressure of 1%, which has a limited effect on the overall slope movement. Hydrologically, a 1-m groundwater level rise is equivalent to 10–100 mm of groundwater recharge (assuming an effective porosity of 1–10%). This was the order of magnitude of groundwater recharge in deep-seated landslides observed by others (Prokešová et al., 2013; Malet et al., 2003; Vallet et al., 2015). This behavior was observed during the six years of groundwater monitoring when the landslide movement did not change its annual displacement rate.

We analyzed groundwater heads at three observation points, with rainfall as a driving force. The response time for PP3A and PP4A was shorter than for PP2A, while the memory of the system for all three wells was similar, where PP4A had a slightly shorter memory. It was not possible to analyze the measured heads with a time series analysis at all observation points. One reason may be that the applied approach was linear, which may be insufficient for deep groundwater levels, where non-linear effects may be important (Collenteur et al., 2019).

Groundwater observations could not be analyzed with time series analysis in eight of the eleven piezometers. Time series analysis was carried out using rainfall as the only driving force and approximating the system as linear (i.e., twice the rainfall results in twice the rise in head). This approach was not adequate when the response to rainfall was non-linear in, for example, fractured and fissured rock formations. Some of the measured heads showed unexpected jumps, which could not be explained physically and were likely related to instrument handling issues (PEG3, PP2B). Other measured heads showed only very small variations over the entire measurement period (PI10, PP4B), which may indicate the possible presence of clogged screens (Hencher, 2010) or that the piezometer was screened in a layer of very low permeability. These responses come from boreholes that were meant to host inclinometers, but they were adapted to provide piezometric level measurements. As the installation was not optimal, this could have resulted in limited connection to the groundwater body (perched or deep), and the readings will have a larger uncertainty (due to the inconsistencies in the installation of pipes or screens within the borehole). Instead, they were considered as indicative for possible follow-up installation of piezometers, not

for detailed groundwater monitoring.

An interesting aspect is the limited functioning of the 29 horizontal drains. In 1998, the drains produced only 20% of the water initially discharged in 1994 (Vásconez, 2000); this is ~12% of the annual rainfall, compared to an initial yield of ~56% of the annual rainfall. Since the groundwater heads started to be collected sometime after the installation of the drains, the effect of drainage could not be detected in the groundwater observations. Nevertheless, time series analysis revealed that if the drains were not 12% of the total annual rainfall, the groundwater recharge would increase by ~1 mm/day. The additional recharge would cause a rise in the groundwater level of up to ~0.5 m in wells PP2A, PP3A, and PP4A. This was concluded from Figure 2.16b, where the step response due to a constant recharge of 1 mm/day resulted in a groundwater level rise of ~0.3 to ~0.5 m. The drains did not reach the deep groundwater systems but drained small perched water bodies within the soil fed by rainfall. This was confirmed by the electrical conductivity results at the drains, which were similar to the electrical conductivity values of rainfall.

The Brönnimann classification system allowed us to simplify the Guarumales landslide to a two-layer system, separated by a slip surface (~30 to >90 m deep). This helped with interpreting the conceptual model where the bottom layer (schist bedrock) was permanently saturated, and the colluvium layer was unsaturated. The permeability of the slope was heterogeneous. Highly weathered material and relatively intact material were found in the slope during the drilling campaigns in both the bedrock and colluvium. We found perched groundwater in the slope, as well as deep/permanent groundwater. Infiltration from rainfall and a regional groundwater system were their main sources

2.7. CONCLUSION

The objective of this study was to characterize, understand, and quantify the mechanisms interfering with the stability of the Guarumales landslide. Special attention was paid to the role of predisposing conditions and possible triggering factors, such as rainfall and groundwater fluctuations. We showed that the movement of the landslide was continuous on an annual timescale, both in the direction and horizontal displacement rate, and there were no significant changes

over the last 18 years. Faster movement was found at the toe of the slope where clayey silt lenses, silty sand lenses, and springs were common. A detailed response of the displacement rate to pore pressure changes, if any, could not be determined as the surface displacement records were not detailed enough.

A conceptual model was developed for the Guarumales landslide. Shallow perched groundwater levels were located in clayey silt and silty sand lenses, which were part of the permeable and mainly unsaturated colluvium layer. The colluvium layer contained blocks of highly fractured shales, overlying a largely saturated unconfined bedrock layer. This agreed with the heterogeneous nature of the slope, which included both highly fractured material and intact material. The unconfined groundwater system is responded with a ~1 to 31 day response time to rainfall forcing on the piezometers PP3A, PP4A, and PP2A, at depths of ~30, ~40, and ~47 m, respectively. The pore water fluctuations were too small to have a significant effect on the landslide movement. The existing drainage did not reach the deep groundwater system. The system only drained small perched water bodies fed by rainfall, as evidenced by the quick response of drain discharge to rainfall, and the low values of electrical conductivity of the drained water.

Future work should be aimed at investigating whether pore water fluctuations in the Guarumales landslide have a significant effect on fluctuations in the landslide movement. This would require the collection of displacement and groundwater level data with higher spatio-temporal accuracy and resolution by using remote sensing or real-time kinematic global positioning systems (RTK-dGNSS) acquisitions.

3

A NEW METHOD TO DETECT CHANGES IN DISPLACEMENT RATES OF SLOW-MOVING LANDSLIDES USING INSAR TIME SERIES

This chapter is based on: Urgilez Vinueza, A., Handwerger, A.L., Bakker, M. et al. A new method to detect changes in displacement rates of slow-moving landslides using InSAR time series. *Landslides* 19, 2233–2247 (2022). <https://doi.org/10.1007/s10346-022-01913-8>

Abstract

Slow-moving landslides move downslope at velocities that range from mm year⁻¹ to m year⁻¹. Such deformations can be measured using satellite-based synthetic aperture radar interferometry (InSAR). We developed a new method to systematically detect and quantify accelerations and decelerations of slowly deforming areas using InSAR displacement time series. The displacement time series are filtered using an outlier detector and subsequently piecewise linear functions are fitted to identify changes in the displacement rate (i.e., accelerations or decelerations). Grouped accelerations and decelerations are inventoried as indicators of potential unstable areas. We tested and refined our new method using a high quality dataset from the Mud Creek landslide, California, USA. Our method detects accelerations and decelerations that coincide with those previously detected by manual examination. Second, we tested our method in the region around the Mazar dam and reservoir in Southeast Ecuador, where the time series data were of considerably lower quality. We detected accelerations and decelerations occurring during the entire study period near and upslope of the reservoir. Application of our method results in a wealth of information on the dynamics of the surface displacement of hillslopes and provides an objective way to identify changes in displacement rates. The displacement rates, their spatial variation, and the timing of accelerations and decelerations can be used to study the physical behavior of a slow-moving slope or for regional hazard assessment by linking the timing of changes in displacement rates to landslide causal and triggering factors.

3.1. INTRODUCTION

In chapter 2, we characterized and performed a hydrological analysis of the deep-seated, slow-moving Guarumales landslide. This case study revealed the complexity of the hydrogeological processes in Guarumales and the limitations of the in-situ monitoring of slope deformations. Considering these results in the analysis of the slow-moving landslides in the Mazar region is imperative.

Both in-situ and remote sensing approaches can be used to monitor slow-moving landslides. In-situ approaches include the Global Navigation Satellite System (GNSS) (Mulas et al., 2018; Notti et al., 2020), terrestrial laser scanners (Rosser et al., 2007; Aryal et al., 2012; Booth et al., 2018; Huang et al., 2019), inclinometers (Lollino et al., 2018) and extensometers (Klimeš, 2018). Remote sensing approaches include Light Detection and Ranging (lidar) (Mackey and Roering, 2011; Pirasteh et al., 2018; Jaboyedoff and Derron, 2020), interferometric synthetic aperture radar (InSAR) (Strozzi et al., 2005; Handwerger et al., 2013; Bayer et al., 2018; Dai et al., 2020), and optical remote sensing (Bennett et al., 2016; Lacroix et al., 2020a). While the highest data quality comes from in-situ measurements, these are limited to single locations within a landslide, can be challenging to install and maintain (especially in remote regions), and as a result, fail to capture large-scale spatial and temporal changes in landslide behavior. Therefore, satellite-based data present advantages when identifying and monitoring large regions of active slow-moving landslides (Lu et al., 2012; Bianchini et al., 2018; Del Soldato et al., 2019; van Natijne et al., 2020).

Satellite-based InSAR data have been used to monitor slow-moving landslides for several decades. Long-term monitoring provides the opportunity to use cumulative displacement time series to detect changes in the motion of a landslide (Cigna et al., 2012; Berti et al., 2013; Raspini et al., 2018) or to detect landslides over broad areas (Bordoni et al., 2018). To better understand landslide processes, these prior studies have focused on displacement time series evaluation in comparison to external triggering factors such as rainfall. The approach proposed in this chapter similarly focuses on long-term kinematic changes and, in addition, expands on prior work by incorporating the spatial variation and timing of such changes at a regional scale. This is a step forward for the regional evaluation of landslides, in particular, more broadly constraining landslide dy-

namics, physical behaviors, and trigger responses.

This chapter presents a method to detect, quantify, and inventory changes in the surface displacement rate of slowly deforming areas, such as landslides, across regional scales. Our method uses InSAR displacement time series to identify slowly deforming areas and detect the moment that a deforming area begins to accelerate or decelerate. All identified accelerations and decelerations are analyzed and inventoried to determine the timing and location of changes in the displacement rate of potential unstable areas. We first test and refine our new approach as a proof of concept at the well-studied and analyzed Mud Creek landslide on the Big Sur coast, California, USA. Then, we apply our method to a regular, unscreened data set along a reservoir upstream of the Mazar Dam, Ecuador.

3.2. InSAR METHODS

3.2.1. InSAR PROCESSING FOR BIG SUR, CALIFORNIA

For the California case study, we examined published InSAR time series from [Handwerger et al. \(2019b\)](#). This time series was made using data acquired by the Copernicus Sentinel-1 A/B (S1) satellites. These data are freely available and are provided by the European Space Agency ([Desnos et al., 2014](#)). The S1 satellites operate with a C-band (5.6 cm) radar wavelength and acquire data with a minimum acquisition interval of 6 days at a given location. Data are collected in ascending (flying north and looking east) and descending (flying south and looking west) flight geometries.

[Handwerger et al. \(2019b\)](#) processed data from descending track 42 between March 2015 and May 2017 and applied corrections to their InSAR data by using a scalable deformation model to reduce and correct unwrapping errors. They also manually removed poor quality interferograms before performing the time series inversion. These two steps were important for creating a high quality InSAR dataset that was used to reveal complex landslide motions. Yet this type of data correction is time consuming and challenging and is therefore infeasible for regional investigations that may consist of tens to hundreds of landslides and hundreds or thousands of interferograms. For the full InSAR processing details and analyses, please see [Handwerger et al. \(2019b\)](#).

3.2.2. INSAR PROCESSING FOR SOUTHEAST ECUADOR

To identify and monitor active landslides near the Mazar Dam, Ecuador, we constructed differential interferograms from InSAR data collected by S1 satellites. We processed the S1 data acquired in the Interferometric Wide (IW) swath mode, which has a 250 km wide swath and a pixel spacing size of ~2.3 m in the looking (i.e., range) direction and ~15.6 m in the along-flight (i.e., azimuth) direction. We processed 966 interferograms using the Jet Propulsion Laboratory (JPL) InSAR Scientific Computing Environment (ISCE) software package (Rosen et al., 2012). Our processing strategy was to construct interferogram pairs with two nearest neighbors. We processed 495 interferograms on ascending track 18 (T18A) and 471 interferograms on descending track 142 (T142D). All of the interferogram pairs used in this study are listed in Online Resources (ESM) 1 and 2 (Urgilez Vinueza et al., 2022). To geocode the data and remove topographic phase contributions, we incorporated a ~30 m DEM from the Shuttle Radar Topography Mission (SRTM) into our processing (Farr et al., 2007). To reduce noise, we multi-looked the interferograms by taking 9 looks in the range direction and 2 looks in the along-flight direction and applied a standard power spectral filter with a value of 0.5 (Goldstein and Werner, 1998). Finally, we quantified the time-dependent behavior of active landslides by constructing time series with the open-access Miami InSAR time-series software in Python (MintPy) (Yunjun et al., 2019). More specifically, we used the Small Baseline Subset (SBAS) technique (Berardino et al., 2002) weighted by the inverse of phase covariance (Tough et al., 1995; Guarnieri and Tebaldini, 2008; Yunjun et al., 2019). We applied a coherence threshold mask and dropped noisy pixels with a coherence of less than 0.4. We also corrected for tropospheric delay using ERA5 data from the European Center for Medium-Range Weather Forecasts (ECMWF) (Jolivet et al., 2011, 2014). To reduce long-wavelength noise, we selected a local stable reference point near the active landslides. The additional InSAR processing steps (i.e., unwrapping error corrections) performed by Handwerger et al. (2019b) for the case of the Mud Creek landslide were not implemented for the Ecuador case study because our goal was to develop and test a InSAR processing strategy that does not require individual corrections such that it can be applied to regional landslide detection and monitoring. The final result is a time series of cumulative displacements measured along

the satellite line-of-sight (LOS) for each pixel.

3.3. METHODOLOGY FOR THE DETECTION OF ACCELERATIONS AND DECELERATIONS

We developed a method to identify and quantify changes in the displacement rate over time of slowly deforming areas by evaluating the InSAR cumulative deformation time series of each pixel in our study areas. We assume that the deforming areas identified with InSAR are slope movement, but they could also be related to deforming structures in the area. Ultimately, we do not expect InSAR signals based on anything else than surface displacement. Our method consists of four steps (Figure 3.1). First, we select pixels in the area of interest that show a significant movement (subsection 3.3.1). Second, we perform outlier detection on the time series of each selected pixel (subsection 3.3.2). Third, we fit a piecewise-linear function model to each selected cumulative displacement time series to identify accelerations and decelerations (subsection 3.3.3). Fourth, we perform a spatial analysis on the detected accelerations and decelerations by identifying neighboring pixels with similar accelerations and decelerations (subsection 3.3.4). Our final result is a monthly inventory of the change points in the displacement time series corresponding to accelerations and decelerations. This information can be used to identify and monitor active slow-moving landslides and other localized ground deformations.

3.3.1. PIXEL SELECTION

The pixel selection is performed by analyzing the InSAR data in the area of interest. To identify the areas that most likely represent slope movement, we define our selection criterion based on the magnitude of the movement of pixels. We select pixels that exhibit the largest magnitude of displacement, above a specified percentile, for further analysis. It is recommended that the selected threshold percentile includes the largest displacement magnitude pixels without including noisy pixels (i.e., isolated pixels that are not likely representing slope movement). A lower threshold may include such isolated pixels, while a larger threshold would avoid noisy pixels, but it would also exclude pixels that belong

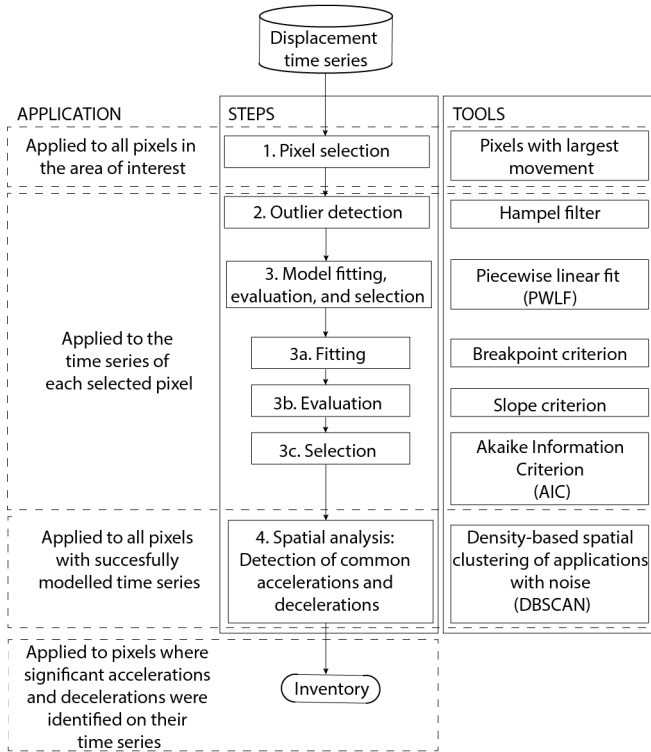


Figure 3.1: Flow chart showing the workflow of the method and the relationship among the steps involved

to potential deforming areas. A preliminary inspection of the data results in a balanced threshold selection. The selected pixels for the case studies in California and Ecuador are presented in subsection 3.4.1 and subsection 3.5.1.

3.3.2. OUTLIER DETECTION

The cumulative displacement time series from the InSAR data may contain outliers, and we use the Hampel method (Pearson, 2005, 2011) to identify them. The Hampel method uses a sliding window that scans the data and identifies an outlier when a data point differs from the median in the sliding window by a specified number of standard deviations. The sliding window is the window size (W) on each side of the evaluated point, so the total sliding window size is 2W + 1. The value of the window size is based on the temporal sampling of the InSAR data. Datasets with a lower temporal sampling require a smaller window size to avoid

including more than one season in the sliding window. A higher temporal sampling allows a larger window size. A lower number of standard deviations results in a stricter filter and in the identification of more outliers, while a higher number of standard deviations results in a coarser filter and fewer outliers. All identified outliers are removed from the time series. Outlier detection is applied to the case studies in California and Ecuador in [subsection 3.4.2](#) and [subsection 3.5.2](#).

3

3.3.3. MODEL FITTING, EVALUATION, AND SELECTION

After the outliers are identified and removed, a piecewise linear function is fitted to each cumulative displacement time series. A piecewise linear function consists of a number of straight segments where the slope of each segment represents a period of movement at a constant velocity. The specific time at which the slope (i.e., velocity) of the linear segment changes is called a breakpoint, and these breakpoints represent the timing of a change in velocity resulting from an acceleration or deceleration. We apply the PWLF Python package ([Jekel and Venter, 2019](#)), which was developed to fit continuous piecewise linear functions, provided that the number of breakpoints is specified.

We fit multiple piecewise linear function models to each time series. Each model has m breakpoints, where m ranges from 1 to the maximum number of breakpoints. Model m has $2m+2$ parameters: m breakpoints, $m+1$ slopes, and an intercept. The maximum number of breakpoints may be set based on the time span of the dataset and the expected maximum number of accelerations and decelerations in a given time frame. For example, in regions where landslides have documented seasonal velocity changes related to wet and dry seasons, we expect two breakpoints (1 acceleration and 1 deceleration) per year (e.g., [Handwerger et al. \(2019b\)](#); [Bayer et al. \(2018\)](#)).

The InSAR displacement time series indicate deformation in the LOS direction and can be positive or negative (depending on the direction of motion relative to the satellite look direction). In order to simplify the analysis, we converted the negative LOS values to positive LOS values since our objective is to detect changes in the time series. Yet, the piecewise linear fit may return sections with negative slopes that correspond to motion with a LOS direction that is opposite a landslide's downslope motion. For landslides, we assume they are always moving

in the same downslope direction within the period of study and there is no obvious physical explanation as to how the sign of the LOS can switch from positive to negative (or vice versa) during a short sliding period. Therefore, we assume negative slopes are a result of inversion or unwrapping errors and remove linear fits with negative slopes unless it is the first or last segment. In this latter case, slopes with LOS opposite of the downslope direction are likely an artifact of a limited number of data points when breakpoints occur near the beginning or end of the time series.

Next, each estimated breakpoint is evaluated using two criteria: the uncertainty of the breakpoint, referred to as the breakpoint criterion, and the estimated confidence intervals of the slopes of the segments on the two sides of each breakpoint, referred to as the slope criterion. The breakpoint criterion is assessed by evaluating the standard error of the estimated timing of the breakpoint. The standard error of the estimated breakpoint must be lower than a predefined threshold, which is set based on the temporal sampling of the InSAR data. The slope criterion considers the confidence intervals of the slopes of two consecutive segments in a model. We estimated the 95% confidence interval of a particular slope as ± 1.96 times the standard error of the estimated slope. A change in slope is considered significant when the confidence intervals of two consecutive slopes do not overlap.

All models that meet the breakpoint and slope criteria are further evaluated using the Akaike Information Criterion (AIC) to determine the optimal number of breakpoints. The AIC criterion is used to assess the overall fit of a model and penalizes for the number of estimated parameters, which prevents overfitting (Burnham and Anderson, 2004). The AIC is computed as:

$$AIC = n \times \left[\ln \frac{SSR}{n} \right] + 2k \quad (3.1)$$

where SSR is the sum of squared residuals, n is the number of data points, and k is the number of parameters (Burnham and Anderson, 2004). A smaller AIC indicates a better model fit. The model with the optimal number of breakpoints has the lowest AIC. Model fitting, evaluation, and selection is applied to the case studies in California and Ecuador in [subsection 3.4.3](#) and [subsection 3.5.3](#).

3.3.4. SPATIAL ANALYSIS: DETECTION OF ACCELERATIONS AND DECELERATIONS

After the breakpoints (i.e., points of acceleration/deceleration) are identified, a monthly spatial analysis is performed. Because of the uncertainty in the estimated timing of a breakpoint, a breakpoint is partly counted in the month of the estimated timing and partly in the months before and after. The distribution across the three months is based on the estimated standard error of the breakpoint as follows. A breakpoint is assigned to the middle of a month, and the probability that it occurs in that month is estimated using a Normal distribution with the estimated standard error as the standard deviation. The remaining probability (i.e., the probability that the breakpoint doesn't occur on the estimated month) is distributed equally over the months before and after. As a result, the number of accelerations or decelerations in a month is not an integer, and the total number of accelerations and decelerations sums to the total number of detected breakpoints.

Finally, a spatial analysis is performed to identify neighboring pixels exhibiting similar time series behaviors. We used the Python implementation of the Density-Based Spatial Clustering of Applications with Noise (DBSCAN) algorithm (Ester et al., 1996; Schubert et al., 2017) to identify pixels that belong to clusters with similar behavior (accelerations or decelerations). The algorithm uses two parameters: the maximum distance between pixels in a cluster and the minimum number of pixels in a cluster (Boeing, 2018). These two parameters are set based on the InSAR data density. More details in [subsection 3.4.4](#) and [subsection 3.5.4](#).

Our final product is an inventory of the timing of the changes in the displacement rate of pixels within a cluster of pixels that show similar behavior. The inventory is accompanied by multitemporal maps of grouped pixels corresponding to areas with similar behavioral patterns, likely representing slope movement. Note that in this chapter, we focus on identifying and quantifying the accelerations and decelerations that we find within pixels that are part of a cluster per month. The grouped pixels are indicators of deforming areas.

3.4. CASE STUDY 1: MUD CREEK LANDSLIDE

We tested and refined our method to detect the timing of accelerations and decelerations from the InSAR time series on data of the Mud Creek landslide. Mud Creek was a landslide that moved slowly for at least eight years (likely much longer) before accelerating rapidly and failing catastrophically on 20 May 2017 (Warrick et al., 2019; Handwerger et al., 2019b; Jacquemart and Tiampo, 2021). This landslide had a pre-catastrophic failure area of approximately 0.23 km² (Handwerger et al., 2019b) and a mean slope angle of 38 degrees (Warrick et al., 2019). The landslide's bedrock geology is composed of the Franciscan melange rock, which is characterized by a clayey granular matrix with highly sheared sandstone, siltstone, meta-sandstone, shale, serpentinite, and blueschist (McLAUGHLIN et al., 1982; McLaughlin et al., 2000). The average precipitation is around 1000 mm/y and occurs primarily between October and May. The Mud Creek landslide experienced extreme drought and extreme rainfall during our study period. A historic drought lasted from 2012-2016, while 2017 was one of the wettest years on record. Previous work by Handwerger et al. (2019b) and Jacquemart and Tiampo (2021) used InSAR time series to detect changes in landslide motion and found that seasonal rainfall drives these changes. This landslide was selected as a proof of concept for our new method due to its high quality time series (as described in subsection 3.2.1) and its documented seasonal behavior. We examined the period of slow landslide motion captured by the S1 InSAR time series between 2015 and 2017.

3.4.1. PIXEL SELECTION, CASE 1

For the Mud Creek landslide, we selected the 2% of pixels with the largest (absolute) displacement (147.4 mm), resulting in 1124 of 93590 pixels. This 2% threshold selected pixels that are part of the deforming area (Figure 3.2). In the case of Mud Creek, a higher percentile (>2%) would include pixels that may represent noise, not real displacement. A lower percentile (<2%) would leave out important pixels that may be part of an unstable area. A preliminary evaluation of the pixels is advised to select the threshold that captures most pixels within moving areas without noisy pixels. All selected pixels are entirely within the boundaries of the pre-catastrophic polygon mapped by Handwerger et al. (2019b).

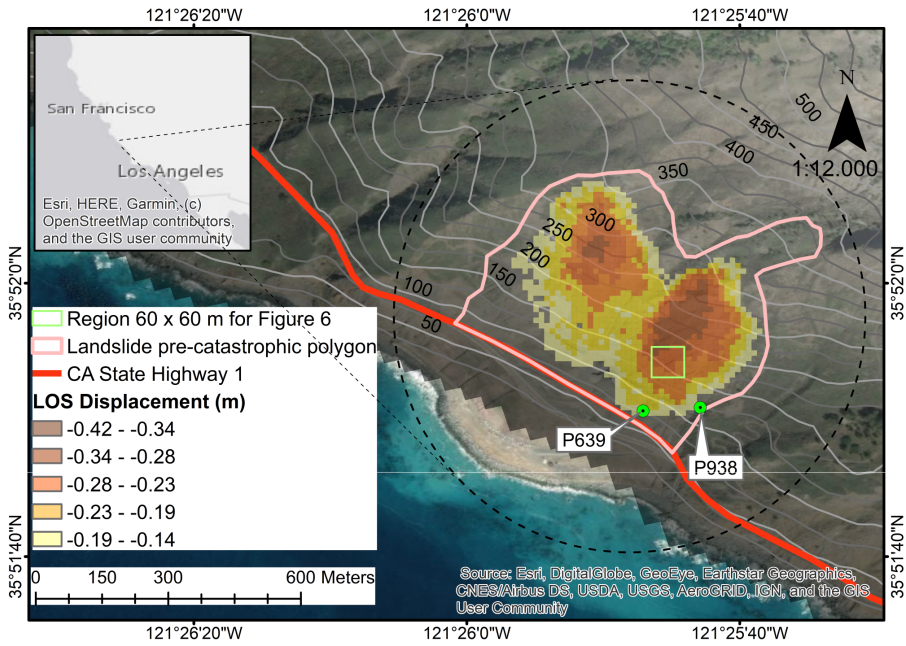


Figure 3.2: Selected pixels showing InSAR cumulative displacement in Mud Creek between 2015-2017. The pink polygon shows the pre-catastrophic collapse polygon from Handwerger et al. (2019b). The green box indicates a representative area of 60 x 60 m used by Handwerger et al. (2019b) to derive landslide velocities

3.4.2. OUTLIER DETECTION, CASE 1

We used the Hampel method to identify outliers as described in subsection 3.3.2 with a sliding window size of 7 data points (representing ~84 days) and 2 as the number of standard deviations. Very few outliers were detected and removed from this high quality data set. In total, 335 outliers were found and removed from 244 time series (0.47% of all data points), with a maximum of 4 outliers in one time series. In Figure 3.3, we show some examples of the application of the outlier filter to the displacement time series of the Mud Creek landslide.

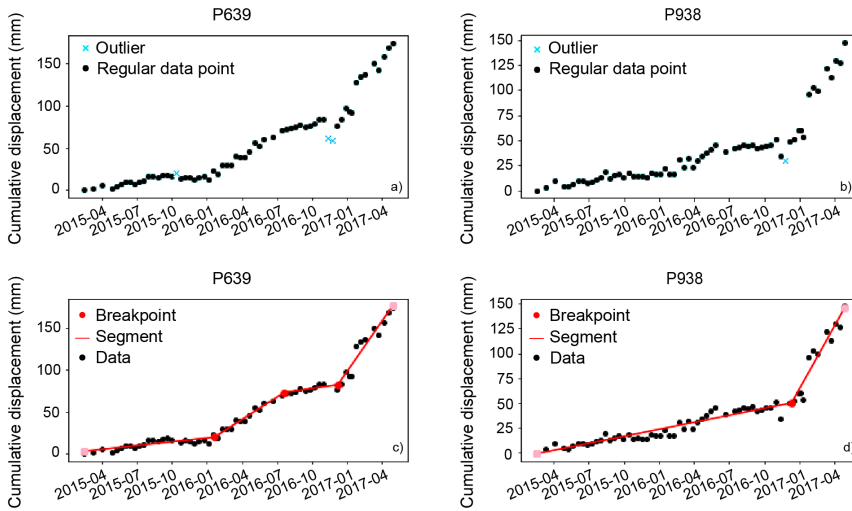


Figure 3.3: Examples of displacement time series and the identified outliers for pixels P639 (3 outliers) and P938 (1 outlier) in (a) and (b) and the fitted breakpoints of pixels P639 (3 breakpoints) and P938 (1 breakpoint) in (c) and (d) in the Mud Creek landslide. Pink points are the initial and final data points of the time series and are not considered breakpoints

3.4.3. MODEL FITTING, EVALUATION, AND SELECTION, CASE 1

We identified the number of breakpoints in each filtered time series using the method described in [subsection 3.3.3](#). We used a threshold standard error value of 30 days for the breakpoint criterion. The maximum number of breakpoints in a time series is set to four because the displacement time series are available for one year and nine months, where we can observe two rainy seasons (October to May each year). Based on the typical landslide behavior in coastal California (e.g., [Handwerger et al. \(2019b,a\)](#)), we expect at most two accelerations and two decelerations. 1120 out of the 1124 time series were fitted successfully. We identified 2967 breakpoints in total: 121 time series (i.e., pixels) with 1 breakpoint, 315 time series with 2 breakpoints, 520 time series with 3 breakpoints, and 164 time series with 4 breakpoints (see [Figure 3.4a](#)).

3.4.4. SPATIAL ANALYSIS: DETECTION OF ACCELERATIONS AND DECELERATIONS, CASE 1

We detected the timing of accelerations and decelerations of the fitted time series, as described in [subsection 3.3.4](#). We determined the location of the pixels of the 1120 fitted time series, and we used the DBSCAN algorithm to identify and select pixels within a cluster, using 12 m as the maximum distance between pixels and 4 pixels as the minimum number of pixels that form a cluster. The maximum distance between pixels is the space between the edges of 2 pixels and is set to 12 m, which is the spacing of the digital elevation model that was used to geocode the interferograms ([Handwerger et al., 2019b](#)). We then compiled an inventory of the total number of accelerations and decelerations detected from pixels within a cluster per month. For Mud Creek, the number of breakpoints after clustering remains the same. All pixels are part of a cluster during the studied period. In [Figure 3.4a](#), the results show that there are two clear periods of an increased number of accelerations (from November 2015 to March 2016 and from October 2016 to April 2017) and one period of an increased number of decelerations (from May 2016 to September 2016).

We compared our breakpoint detection inventory to the local precipitation patterns known to have controlled the behavior of Mud Creek. We found very little activity between July and October 2015 (i.e., there are no accelerations and only a few decelerations). This period is at the end of the dry season of a historic drought period. The landslide behavior changed when the 2015-2016 rainy season began, and we detected many acceleration breakpoints between October 2015 and February 2016. [Figure 3.4b](#) shows that a large portion of the landslide was accelerating in February 2016 (rainy season). This period of acceleration was followed by a period of deceleration during the 2016 dry season. [Figure 3.4c](#) shows the spatial distribution of deceleration points within the landslide in June 2016. Comparison with the November 2016 map shows spatial differences in the timing of accelerations and decelerations within the landslide.

The landslide then started to accelerate again shortly after the onset of seasonal rainfall in the wet season of 2016-2017. We found that the largest number of accelerations recorded in a month occurred earlier (two months after the onset of the rainy season) and was higher than the previous 2015-2016 wet season ([Fig-](#)

ure 3.4a). This change in behavior was presumably driven by the large changes in rainfall that occurred during the study period and our findings agree with the detailed analysis presented by Handwerger et al. (2019b). We found that almost all pixels within the landslide are accelerating in November 2016 (Figure 3.4d). Accelerations occurred during the entire wet season until the catastrophic failure in May 2017.

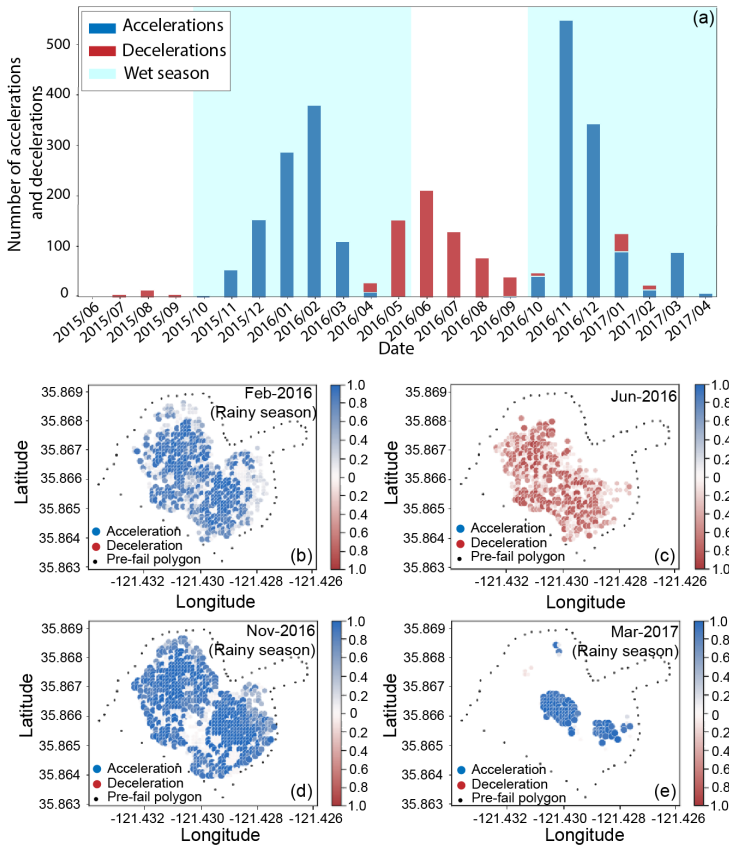


Figure 3.4: Inventory of monthly accelerations and decelerations for the Mud Creek landslide (a) and the location of the pixels showing accelerations and decelerations and the pre-fail polygon on February 2016 (b), June 2016 (c), November 2016 (d) and March 2017 (e). The color bar on the side of (b), (c), (d), and (e) indicate the probability of occurrence of acceleration (in blue) or deceleration (in red) shown in the map. A 100% probability of acceleration is indicated by 1 in blue, while a 100% probability of deceleration is indicated by 1 in red

We also compared our inventory of accelerations and decelerations to the velocity time series of Handwerger et al. (2019b) for 36 pixels within an area of 60 x

60 m in the landslide (Figure 3.2). The timing of accelerations and decelerations found with our method match those found by Handwerger et al. (2019b). Accelerations detected with our method correspond to periods of increasing velocities, while decelerations were detected during the period of decreasing velocities (see Figure 3.5). We observe that 32 out of 36 pixels accelerated from December 2016 to March 2017, 31 out of 36 pixels decelerated from May 2016 to August 2016, and 35 out of 36 pixels accelerated again from October 2016 to January 2017. Only 2 pixels decelerated in this last period.

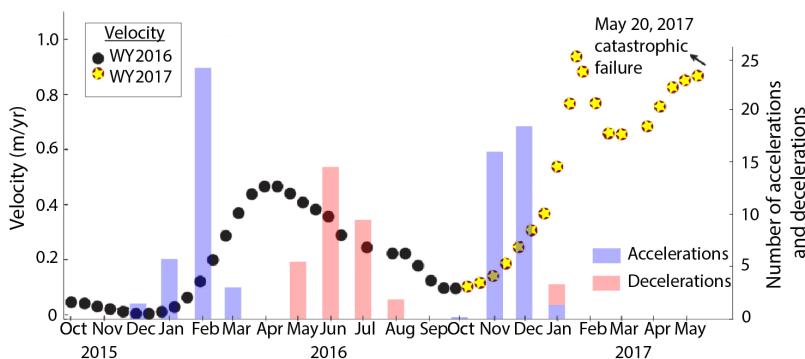


Figure 3.5: Velocity time series of Mud Creek landslide for the water years of 2016 (black dots) and 2017 (yellow dots) for a representative area (averaged over 60 x 60 m, shown in Figure 2) (modified from Handwerger et al. (2019b)). Blue and red bars represent our detected number of accelerations and decelerations, respectively. April 2016 and September 2016 show no accelerations and decelerations because there are no clustered responses at those times

3.5. CASE STUDY 2: MAZAR REGION

Our second study site is the region surrounding the Mazar hydroelectric power plant and its reservoir in southeast Ecuador (Figure 3.6). Here, a major hydroelectric complex extends from the Andes to the Amazonian region. The area is known to have several deep-seated landslides (e.g., Nicole (2015); Urgilez Vinuela et al. (2020)). Around the reservoir, seventeen slow-moving landslides have been identified by CELEC. CELEC identified the unstable areas during the construction of the Mazar dam and has been monitoring them because they are a threat to sustainable hydropower generation. The lithology of the landslide area is composed of two geological units: Alao Paute and El Pan, characterized

by metamorphic rocks, overlain by colluvium deposits ranging from 2 to 28 m (Nicole, 2015). The precipitation in the area is around 3000 mm/year and occurs primarily between April and August.

3.5.1. PIXEL SELECTION, CASE 2

For the Mazar region, we selected an area of 211 km² around the reservoir to examine the InSAR displacement time series from October 2016 to August 2020. Our pixel selection resulted in 3230 pixels with an absolute displacement value above the 98th percentile (99.9 mm). 28% of the selected pixels fall within the boundaries of the ground-based landslide inventory carried out by CELEC, while 72% fall outside the boundaries of the identified unstable areas.

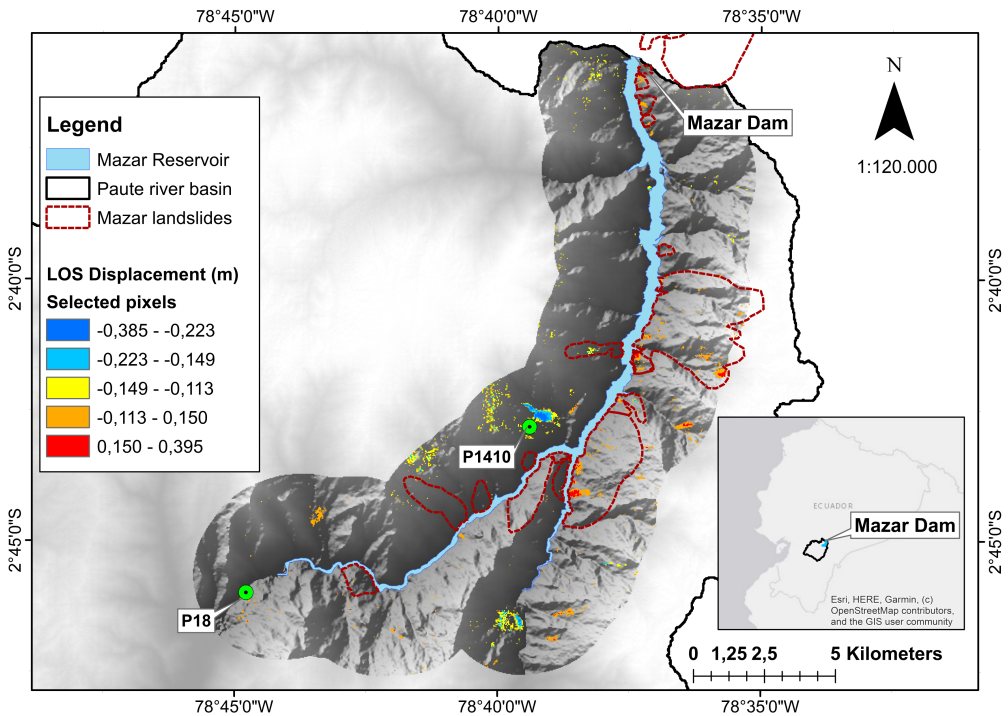


Figure 3.6: Location of the Mazar landslides, the Mazar dam, and the selected pixels around the Mazar reservoir. In addition, we show the 2% pixels with the largest cumulative displacement over four years over an area of 211 km² around the reservoir

3.5.2. OUTLIER DETECTION, CASE 2

We used the Hampel method as described in subsection 3.3.2 with a sliding window size of 7 data points and 2 as the number of standard deviations. Factors such as the vegetated soil cover and atmospheric disturbances resulted in noisy displacement time series. Additionally, and contrary to the case of the Mud Creek landslide, prior quality control of the data was not conducted for the Mazar landslides. One of the main objectives of our new detection method is to process large quantities of data at a regional spatial scale and in a relatively fast and semi-automated manner. In total, 25860 outliers were found in 2268 time series, each time series with 1 to 24 outliers. 4.7% of the data points were identified as outliers and removed from the time series. In Figure 3.7, we show two examples of the application of the outlier filter to the displacement time series of the pixels in the Mazar region.

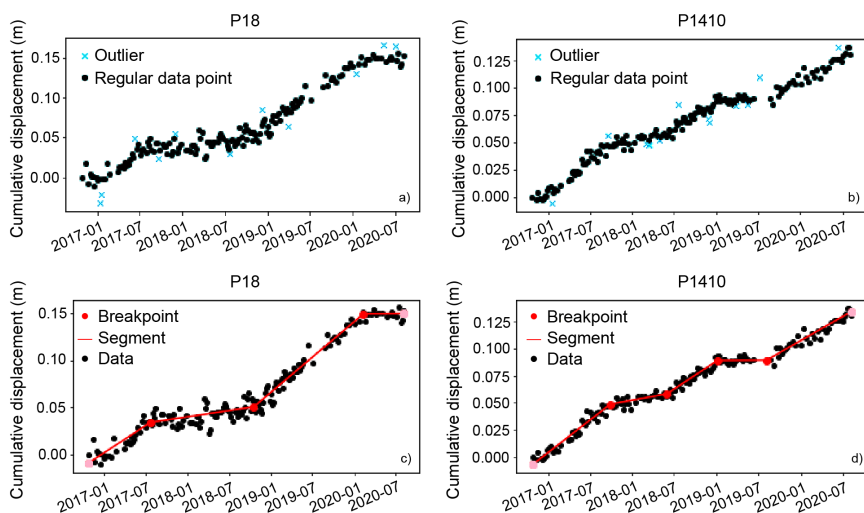


Figure 3.7: Examples of displacement time series and the identified outliers for pixels P18 (11 outliers) and P1410 (12 outliers) in (a) and (b) and the fitted breakpoints of P18 (3 breakpoints) and P1410 (4 breakpoints) in (c) and (d) in the Mazar region. Pink points are the initial and final data points of the time series and are not considered breakpoints

3.5.3. MODEL FITTING, EVALUATION, AND SELECTION, CASE 2

We identified the breakpoints in each time series using a threshold standard error value of 30 days for the breakpoint criterion. In the case of the Mazar region, we set the maximum number of breakpoints to eight due to the expected number of accelerations and decelerations that can occur over three years and six months under the influence of the rainy season (April-August). Our method was able to fit 2273 out of the 3230 time series successfully. We identified 3397 breakpoints in total: 1155 time series with 1 breakpoint, 725 time series with 2 breakpoints, 237 time series with 3 breakpoints, 107 time series with 4 breakpoints, 41 time series with 5 breakpoints, and 8 time series with 6 breakpoints. Two example fits are shown in [Figure 3.7c, d](#).

3.5.4. DETECTION OF ACCELERATIONS AND DECELERATIONS IN A CLUSTER, CASE 2

We performed the spatial analysis using the pixels of the 2273 fitted time series per month, using 30 m (i.e., DEM pixel spacing) as the maximum distance between pixels and 4 pixels as the minimum number of pixels that create a cluster. In the case of the Mazar region, the number of breakpoints after clustering diminished. There are 2793 of 3397 breakpoints in total: 561 time series with 1 breakpoint, 566 time series with 2 breakpoints, 186 time series with 3 breakpoints, 90 time series with 4 breakpoints, 34 time series with 5 breakpoints, and 2 time series with 6 breakpoints. In [Figure 3.8](#), we present a spatio-temporal inventory of the number of detected acceleration and deceleration points within a cluster and the location of the corresponding pixels for four periods. [Figure 3.8a](#) and [b](#) show a seasonal and yearly distribution of the monthly number of accelerations and decelerations, respectively. [Figure 3.8a](#) shows that the number of decelerations is higher than the number of accelerations in the first months of the year. There is a modest increase in the number of accelerations and a modest decrease in the number of decelerations once the wet season starts. However, we observe that by the end of the wet season and after, both accelerations and decelerations occur. [Figure 3.8b](#) indicates that the number of accelerations increases throughout the study period while the number of decelerations decreases. In 2020, the number of accelerations was higher than the number of decelerations.

Figure 3.8c-f show the location of pixels with a mild to high probability of occurrence of accelerations and decelerations.

By examining the spatial variability of accelerations and decelerations over the area around the Mazar reservoir, we find that most of the activity occurs on the south side of the reservoir, where two reservoir tributaries meet. Some activity is observed near the dam, on the north side, and the central-east side of the reservoir. Our inventory reveals that accelerations and decelerations occur throughout the year and are sparse around the reservoir. These are concentrated in specific locations at the end of the study period. This variability of accelerations and decelerations occurs within and between groups of pixels.

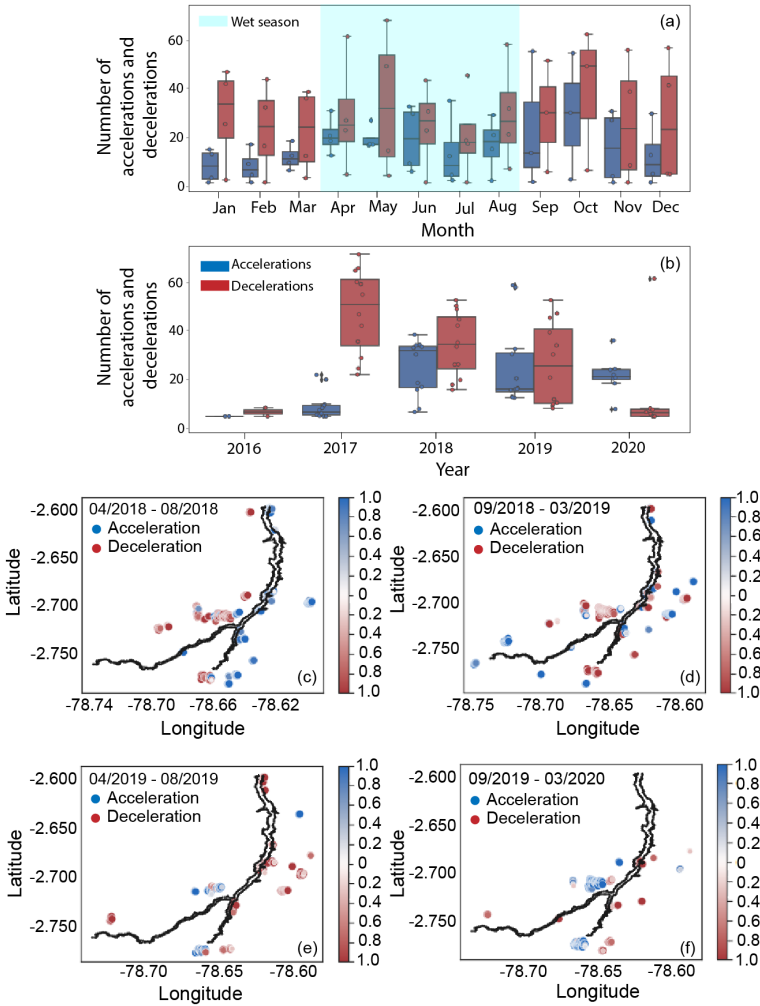


Figure 3.8: Spatio-temporal inventory of accelerations and decelerations for the Mazar region. (a) and (b) Indicate seasonal and yearly distribution of monthly accelerations and decelerations, respectively. The location of the pixels showing accelerations and decelerations for four periods are shown in panels (c), (d), (e), and (f). Panels (c) and (e) are during the rainy season of 2018 and 2019, respectively, with an average of 704 mm of rainfall over 5 months. Panels (d) and (f) occur during the dry season of 2018 and 2019, respectively, with an average of 557 mm of rainfall over 7 months. The color bars on the side of (c), (d), (e), and (f) indicate the probability of occurrence of the acceleration (in blue) or deceleration (in red) shown on the map. A 100% probability of acceleration is indicated by 1 in blue, while a 100% probability of deceleration is indicated by 1 in red. The black polygon shows the outline of the Mazar reservoir.

3.6. DISCUSSION

In this chapter, we developed a systematic method to detect, quantify, and inventory changes in the surface deformation rate of slowly deforming areas at a local and regional scale to investigate their temporal and spatial dynamics. Slow-moving landslides have been studied prior to this work using satellite data to identify ground motion areas and shifts in the displacement time series (Cigna et al., 2012; Berti et al., 2013; Raspini et al., 2019). Our method differs from previous work in that our InSAR detection analysis provides an objective way to construct multitemporal maps of unstable areas and an inventory of the timing of changes in the deformation rate of unstable areas.

Due to the nature of the InSAR data, the time series we used for the analysis often contained outliers. These outliers are usually related to specific data acquisitions in the time series and impede the fitting of the piecewise linear functions. For the Mud Creek landslide, there were very few outliers because analyses of a single landslide allow for more in-depth quality control measures. For Mazar, there were many outliers because we did not carefully inspect individual interferograms or perform unwrapping error corrections. This was intentional as one of our main goals is to develop a method to analyze large quantities of regional slope deformation data where it is infeasible to inspect and/or make corrections to thousands of interferograms. Therefore, we opted for the Hampel method as a filter routine to identify and remove the outliers while, at the same time, avoiding the exclusion of important data.

The optimization of the Hampel parameters was carried out considering the temporal sampling of the InSAR data. Smaller window sizes will not detect short-term outliers, while larger window sizes fail to identify outliers within a small portion of the window due to a higher median value. In our case, we used a window size of seven data points, representing a period of ~90 days, and the number of standard deviations was set to two. Moreover, we found that using a standard deviation smaller than 2 tends to over-smooth the time series while using a standard deviation over 3 did not identify all outliers.

We evaluated the uncertainty of the timing of the breakpoints using the breakpoint criterion and decided on a threshold standard error value of 30 days. A smaller threshold value leads to a stricter algorithm so few breakpoints are ac-

cepted. On the contrary, a higher threshold value allows more breakpoints to be identified, but then the time frame when accelerations and decelerations occur becomes too large and becomes meaningless with respect to slow-moving landslide dynamics. Any threshold that yields a time frame larger than the duration of a (wet) season will not give useful information about the temporal dynamics of the slow-moving slopes. Therefore, we used a threshold standard error of 30 days and a monthly temporal resolution.

We selected our pixels considering the 98th percentile of the absolute cumulative displacement of the InSAR data. Some of the selected pixels that comply with this condition were isolated and did not have an immediate neighboring pixel showing significant displacement. We assumed that isolated pixels do not correspond to landslides. Several studies have shown that clusters of pixels with relatively high LOS displacement can be used to identify active landslides (e.g., [Bekaert et al. \(2020\)](#)). Therefore, we selected pixels that belong to a cluster that showed activity (acceleration or deceleration) in the same month. We followed this approach to achieve spatial consistency and temporal persistency (pixels with a significant change in displacement rate) ([Raspini et al., 2018](#)).

Our method identified breakpoints that show clear changes in deformation velocity that can be related to seasonal rainfall. In the Mud Creek landslide, accelerations occur during the rainy season, while decelerations occur during the dry season, as has been shown by hundreds of landslides in coastal California ([Handwerger et al., 2019a](#)). Previous work on the Mud Creek landslide showed that the slope dynamics are directly related to large changes in seasonal rainfall ([Warrick et al., 2019](#); [Handwerger et al., 2019b](#); [Jacquemart and Tiampo, 2021](#)). Our change detection approach captured the seasonal kinematics of Mud Creek and allowed us to explore spatial trends and accelerations and decelerations by fully utilizing the rich information provided by InSAR. During the period between Feb-May 2017, the landslide was likely moving faster than InSAR can detect, as the landslide approached catastrophic collapse. This causes phase bias, an additional unwrapping challenge that obscures the true deformation rate and is not possible to correct manually. However, it is encouraging that our method detected the overall change in the signal of the data, dominated by accelerations, and did not capture the small apparent deceleration in the months before failure

(Figure 3.5).

For the Mazar region, we observed more complex behavior resulting from analyses of numerous large and spatially variable deforming areas. We found that the accelerations and decelerations occurred during the entire study period and were distributed around the reservoir. In Figure 3.8 a and b, we showed that both accelerations and decelerations occurred during the entire period and that in 2020 the number of accelerations was higher than the number of decelerations. The high number of unstable areas that were identified using our method may have caused this somewhat less predictable behavior, which can be related to lagged responses of deep-seated landslides in the area, as well as to the creep behavior of more surficial landslides. Local factors such as slope, distance to the reservoir, specific land use, irrigation, and local geomorphology, among others, may influence these different behaviors and the occurrence of accelerations and decelerations at different times. This behavior is also captured at Mud Creek, where even a single landslide can show spatial variation in the timing of accelerations and decelerations. The overall behavior of the Mazar region is complex and needs further in-depth analysis, such as a hydro-meteorological and geotechnical analysis of the larger Mazar region, which is out of the scope of this paper and is part of our next follow-up study.

3.7. CONCLUSIONS

We developed an objective and systematic method for detecting accelerations and decelerations of slowly deforming areas from InSAR data. Our method consists of InSAR time series analyses corresponding to the selected pixels (with the highest cumulative displacement). These time series are filtered, and breakpoints are detected using piecewise linear functions fitted to the time series. These breakpoints represent the times when the displacement rate changes significantly. We analyzed the spatial distribution of the successfully modeled pixels and inventoried the accelerations and decelerations that showed similar spatial behavior.

We tested our method on the high-quality InSAR dataset of the Mud Creek landslide in California. Our method successfully detected the timing of accelerations and decelerations at Mud Creek that were driven by changes in seasonal

rainfall. Next, we investigated a landslide-prone area impacting a hydropower area in southeast Ecuador. Although the time series data were of significantly lower quality (compared to Mud Creek), we identified deforming areas with complex acceleration and deceleration patterns within and between groups of pixels that did not always coincide with wet and dry seasons.

We conclude that our method can identify changes in the ground surface displacement rate of deforming areas that can be used to examine this behavior and inventory these changes in an objective and straightforward manner. The ability to determine the temporal and spatial variation of velocity changes is a step forward in the large-scale interpretation of the physical behavior of slow-moving deforming areas. Ultimately, our inventory of accelerations and decelerations can be used to shed light on the dynamics of slow-moving landslides at both sub-landslide and regional scales with high spatial and temporal resolution.

4

EVALUATION OF THE DYNAMICS OF THE SLOW-MOVING LANDSLIDES IN THE MAZAR REGION USING INSAR-DERIVED DISPLACEMENT DATA

Abstract

The tropical Ecuadorian Andes is characterized by the presence of slow-moving landslides that have been identified and monitored for many years, becoming increasingly important since the impoundment of the Mazar reservoir in 2010, in southeast Ecuador. In the previous chapter, we leveraged satellite-derived displacement time series and developed a method to determine changes in the displacement rate of slow-moving landslides, and we applied it to the slopes around the Mazar dam and reservoir. In this chapter, we aim to identify and model the timing and frequency of velocity changes of pixels and to investigate whether they are correlated with hydrometeorological forcings. We built 85 models using multiple regression analysis and we found that the multiple regression models show a modest R^2 (maximum 0.44). We found that the regional behavior of slow-moving landslides could not be correlated to the hydrometeorological factors of the area, suggesting that hydrology alone is insufficient to explain the behavior of slow-moving landslides in the region, as most clusters exhibit little to no seasonal dynamics (one or two velocity changes) over four years. The quality of the InSAR data and the effect of local in-situ factors such as local geology, morphology, and anthropogenic activity might be influencing the regional landslide dynamics to the local and regional scale.

4.1. INTRODUCTION

Slow-moving landslides are characterized by their slow velocity, being in the order of millimeters to centimeters per year. These landslides are constantly monitored, especially in areas where they pose a potential threat. They can remain active for a long time and sometimes become catastrophic (Hendron Jr and Patton, 1985; Intrieri et al., 2018; Handwerker et al., 2019b).

While slow-moving landslides are primarily studied in the United States, Europe, and some parts of Asia (Lacroix et al., 2020b), research in the tropical Andes is limited due to a lack of in-situ data, with most studies focusing on case studies (e.g., Zerathe et al. (2016); Soto et al. (2017); Urgilez Vinueza et al. (2020)). To overcome this challenge, researchers have used other sources of data, such as satellite-derived displacement, to observe and analyze superficial slow deformations on unstable slopes (e.g., Bordoni et al. (2018); Raspini et al. (2018); ?). These analyses enable the characterization of slow-moving patterns on a large scale and a regional evaluation of the overall state of unstable slopes.

Furthermore, most of these studies use hydrometeorological forcings, with rainfall being the primary driver of accelerated movement (e.g., Iverson (2000); Tofani et al. (2006); Matsuura et al. (2008); Zerathe et al. (2016); Soto et al. (2017); Handwerker et al. (2019b)). However, hydrometeorological data are not always available (either due to temporal or spatial constraints), especially in remote areas. Researchers have resorted to using satellite-derived data to estimate rainfall and other hydrological proxies (e.g., Uwihirwe et al. (2020)).

In chapter 3, we proposed a methodology to detect changes in the displacement rate of slow-moving landslides using InSAR-derived displacement data. We applied that methodology to the slopes around the Mazar reservoir in southeast Ecuador and identified specific locations where accelerations and decelerations occurred over the four years of analysis. The objective of this chapter is to identify the timing and frequency of velocity changes in the Mazar reservoir area and to investigate whether they are correlated with hydrometeorological forcings.

Here we use multiple regression analysis to investigate the relationship between accelerated movement, hydrology, and meteorology in the area. We used the results from chapter 3, hydrometeorological data provided by governmental institutions, and data from satellite sources as input data for the multiple regres-

Table 4.1: Inventory of observed slow-moving landslides around the Mazar reservoir provided by CELEC-EP. The numbers correspond to the landslides in Figure 1

Number	Name	Area (ha)	Type of movement
1	Chalacay	~9	Creep, toe erosion
2	Cruzpamba	~30	Translational, creep
3	Ermita	~20	Creep, toe erosion
4	Guachapala	~190	–
5	Las Juntas	~89	Translational, creep
6	Llamacon	~90	Creep
7	Naste	~61	Rotational, creep
8	Osomache Norte	~20	Creep, toe erosion
9	Osomache Sur	~30	Creep, toe erosion
10	Osoyacu	~380	Translational, creep
11-12	Palmas – Santa Rosa	~155	Translational, creep
13	Santa Rita	~15	–
14	Toctehuayco	~40	–
15	Tomebamba	~180	Translational, creep
16	Tuban	~18	–

sion analysis. The multiple regression results help to determine if the hydrometeorological variables have a significant influence on the displacement dynamics.

4.2. DESCRIPTION OF THE STUDY AREA

The area under study is located in southeast Ecuador and sits within the Cordillera Real, as part of the Andes mountain range. The Hidropaute hydroelectric complex is located here and produces almost one-third of the country’s total energy using three hydropower plants. The Mazar dam is one of them. Sixteen landslides have been identified along the Mazar reservoir and monitored for several years since its impoundment in 2010 (Figure 4.1). Table 4.1 shows the landslide inventory, their areas, and identified types of movement.

The study region is located in the transition between the Andes mountain range and the Amazon rainforest. Geologically, the landslides are located within the Alao Paute Unit and El Pan Unit (as part of the Alao terrain), which are characterized by metamorphic rocks (shale and phyllites), meta-andesites, volcanic

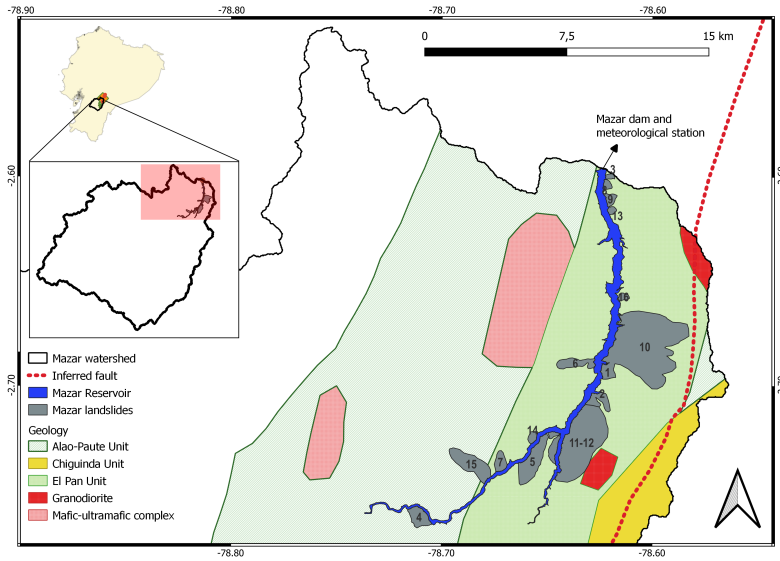


Figure 4.1: Location and geological map of the Mazar landslides

agglomerates, tuffs, and green rocks that have developed pelite and schist facies (Nicole, 2015; Urgilez Vinueza et al., 2020) (Figure 4.1). The mean annual rainfall is around 1290 mm/year, measured at the Mazar meteorological station from 2013 to 2020, with a standard deviation of ~230 mm/y. The rainfall is influenced by the Amazonian regime. The wettest season is from April to August, and the somewhat drier season is between November and March. The slopes range from 0° to $> 45^\circ$, with a median of 20° . The vegetation in the area is considered a lower mountain rainforest, with land used for the construction of small towns, agriculture, and cattle grazing. Small, shallow soil slides are relatively abundant (see Figure 4.2) and have altered the landscape, especially in steep areas with a slope $> 45^\circ$.

4.3. DATA SOURCES

4.3.1. DISPLACEMENT DATA

Since 2012, in-situ geodetical data of some of the landslides have been collected by Electrical Corporation of Ecuador (CELEC-EP) personnel every 30 days (Table 4.1). The surveys use total stations and fixed reference points. This information generates a time series of cumulative displacement per observation point.



Figure 4.2: Examples of slopes around the Mazar lake, with visible alterations on the toe of the slope and signs of creep deformation.

4

In this study, we select 13 out of 14 available in-situ observation points from the Chalacay landslide for further analysis (CH1 to CH14). CH11 is discarded from the analysis because its time series did not match the temporal resolution of the current study. Even though the remaining landslides have in-situ displacement time series, most were incomplete or did not match the temporal resolution of the current study. In the previous chapter, we compiled the inventory of accelerations and decelerations in the study area for 2016-2020 from InSAR data. These accelerations and decelerations were linked to a specific location represented by a pixel that belonged to a cluster of pixels. Combining pixels into a cluster of pixels ensured spatial consistency. The timing of the accelerations and decelerations, as well as their locations, were used here.

4.3.2. HYDROMETEOROLOGICAL DATA

Hydrometeorological data were obtained from different sources. For rainfall, data were provided by the Municipal Public Company of Telecommunications, Water, Sewerage, and Sanitation of Cuenca (ETAPA-EP) and CELEC-EP. However, the datasets were incomplete for the studied period (2016-2020). Therefore, we explored two options: look for nearby stations and perform intra-station interpolation and satellite-derived rainfall products. [Appendix A](#) details this analysis, where ultimately, we used rainfall from the Mazar station infilled with rainfall from a meteorological station located 20 km downstream.

Reference evapotranspiration was used to derive effective rainfall in the area. It was calculated using the Mazar meteorological station data using the Python package PyEt-a ([Vremec and Collenteur, 2021](#)). The Mazar meteorological sta-

tion measures temperature, relative humidity, wind velocity, and short-wave radiation data to calculate reference evapotranspiration. The PyEt-a package offers several methods for calculating reference evapotranspiration depending on the input data availability. In this case, we used the FAO guidelines for crop evapotranspiration that uses the Penmann-Monteith equation (Allen et al., 1998).

CELEC-EP provided water levels of the reservoir and discharge data from the Mazar dam. Given that the temporal resolution of the displacement data is monthly, the hydrometeorological data were resampled to match the temporal resolution of the displacement data.

Daily soil moisture data was provided by Planet, formerly VanderSat (VdS) (<https://vandersat.com/data/soil-moisture/>, last access: 5 April 2023). We processed over 2000 raster files containing volumetric near-surface soil moisture for the upper 5 cm of soil, with a spatial resolution of 100 m x 100 m. We calculated the soil moisture averaged over the area and resampled it to a monthly time step.

4.4. METHODOLOGY

4.4.1. DISPLACEMENT ANALYSIS

The first step was to verify the satellite displacement data using in-situ deformation time series in the Chalacay landslide. The Chalacay landslide was selected for this evaluation because of its clear displacement and the presence of 13 in-situ displacement monitoring points. This way, we verify that the in-situ and satellite-derived data show a similar deformation pattern. In the Chalacay landslide, we projected the LOS displacement time series to the slope direction. The projection was made using the methodology specified in Handwerger et al. (2019b), where the geometry of the radar instrument and the downslope direction are accounted for through a vector transformation.

The next step was to derive a time series of normalized velocities per pixel in the Mazar area. To do this, we used the timing of the changes in the velocity of each pixel. We found that, in the Mazar area, there were pixels with one to a maximum of four changes in velocity. Therefore, at most, five different velocities existed in a particular time series. Note that we are, at this stage, mainly interested in relative velocities and the occurrence of accelerations and decel-

erations. Therefore, each measured LOS velocity was normalized relative to the average LOS velocity at that location. We classified normalized velocities above one as high and below one as low.

Moreover, each cluster of pixels was manually evaluated to determine whether the velocity time series of the individual pixels were consistent. Then, a single ‘master’ time series of normalized velocities per cluster was obtained by taking the median velocity of all individual time series. Subsequently, we constructed a heat map showing normalized velocities per cluster per month to observe trends of relatively high and low velocities in time. Lastly, we constructed a time series of the percentage of clusters with high velocities per month.

4

4.4.2. HYDROMETEOROLOGICAL VARIABLES

In addition to monthly rainfall, effective rainfall, reservoir water levels, and soil moisture, we derived other hydrometeorological variables that might be related to slow-moving dynamics in the region, such as antecedent precipitation Index (API) as a proxy of soil moisture and the number of high-intensity rain events in the basin. We also used the exponential moving average (P_{EMA}) of rainfall to explore the long-term rainfall signal in the area.

The antecedent precipitation index (API) was used as a proxy for soil moisture accumulation. It is based on rainfall that has occurred in the preceding days, acting as a measure of catchment wetness. The API in a particular day was calculated as the rain of that day plus the rain of a predefined number of days prior, influenced by a decay factor k .

$$API_t = \sum_{n=0}^T k^n P_{t-n} \quad (4.1)$$

where P_t is the daily precipitation [mm d^{-1}] on day t , k is the decay factor, and T is the predefined number of days prior to day t considered for the calculation of API. The value of API was taken on the last day of the month to derive monthly data. In this case, the exponential moving average (P_{EMA}) was used to identify long-term trends in the rainfall data. P_{EMA} was calculated using rain from that day plus P_{EMA} from the previous time step, both affected by a smoothing factor.

$$P_{EMA_0} = P_0 \quad (4.2)$$

$$P_{EMA_t} = \alpha P_t + (1 - \alpha)P_{EMA_{t-1}}; t > 0 \quad (4.3)$$

where P is the rainfall observation at time t , P_{EMA_t} is the exponential moving average at time t , and α is the smoothing factor. The P_{EMA} at the first timestep is the rainfall on that day. The smoothing factor varies between 0 and 1, representing the weight given to the most recent period.

Finally, we defined the number of high-intensity rain events in the area in a month using daily rainfall. We defined an event as the accumulation of rain from successive days, with at most one gap day without rainfall. In a determined month, a high-intensity event was defined as being in the top 75th percentile of rain events.

Ultimately, seven hydrometeorological variables (i.e., rainfall, effective rainfall, reservoir water levels, API, P_{EMA} , soil moisture, and the number of high-intensity events) were tested against the slow-moving dynamics of the landslides around the Mazar reservoir.

4.4.3. EVALUATION OF DISPLACEMENT DATA AGAINST HYDROMETEOROLOGICAL VARIABLES

Normalized velocities were evaluated against the hydrometeorological variables through correlations and multiple regression analyses. The idea was to determine whether the hydrometeorological variables were correlated with the slow-moving dynamics of the landslides under study. A single time series was obtained with the percentage of clusters that move with above-average velocity each month. A correlation analysis was performed between this time series against all seven hydrometeorological factors. Then, a multiple regression analysis was performed using non-correlated variables. This was determined by observing the correlations between the hydrometeorological variables. A high correlation between two or more of these variables meant they did not participate in a multiple regression model together.

4.5. RESULTS

4.5.1. DISPLACEMENT ANALYSIS

As described in the methodology section, a comparison was made between 13 in-situ displacement time series from the Chalacay landslide and the satellite-derived displacement time series from 28 pixels within the landslide. We classified the in-situ and satellite-based points based on their cumulated value into four categories: low, mid-low, mid-high, and high velocities. The location of these points and the class to which they belong are shown in [Figure 4.3](#). It shows that the in-situ and satellite-based monitoring points were mainly located on the north side of the landslide area. The fastest-moving points were located close to each other on the northern sector of the landslide, while the surrounding points showed mid-high and mid-low velocities for both in-situ and satellite monitoring points. The low-velocity points were located on the outer part of this cluster for both in-situ and satellite-based monitoring points and on another location on the south of the landslide for satellite-based monitoring points. The results show that the satellite-based observations were closely related to the in-situ monitoring points. A direct comparison between the in-situ and satellite-based cumulative displacement time series per category can be seen in [Figure 4.4](#).

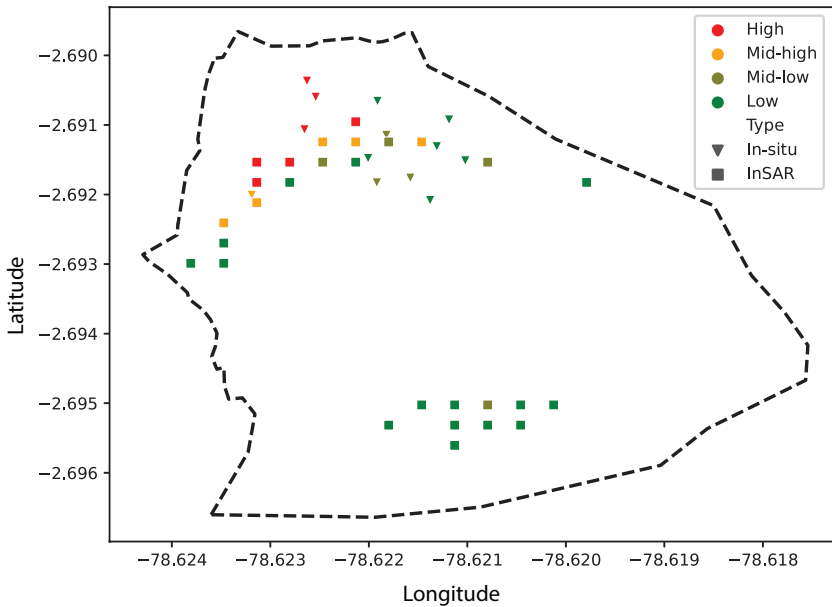


Figure 4.3: Chalacay landslide and its in-situ and satellite-based monitoring points. The legend shows the class to which each monitoring point (triangle) and pixel (square) belong to, based on the cumulative displacement value

Figure 4.5 shows the cumulative displacement boxplots from the in-situ observations (a) and the projected cumulative displacement from satellite observations, (b). In both panels of Figure 4.5, 3 (in-situ) and 4 (satellite) observation points have a cumulative displacement above average. This is also detected in Figure 4.3, where high-velocity cumulative displacements were located on the northern part of the landslide.

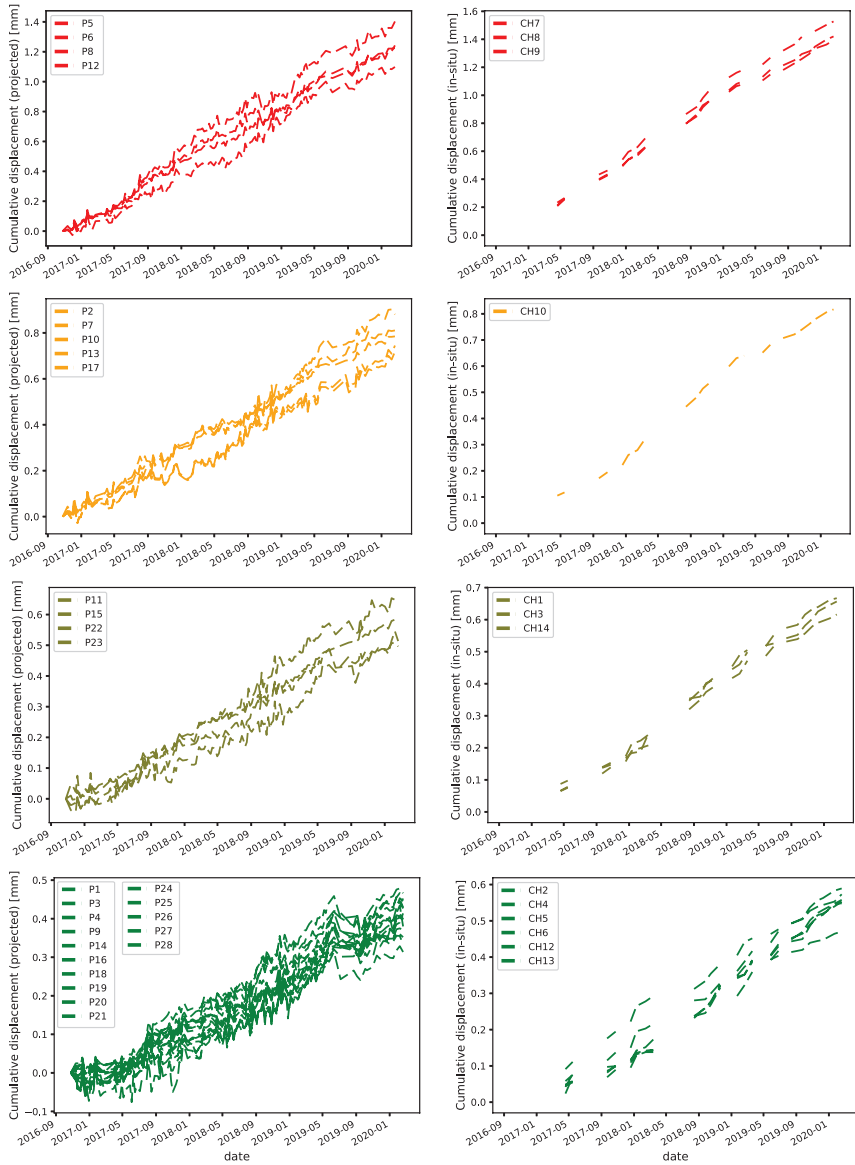


Figure 4.4: Cumulative displacement time series of the in-situ monitoring points in the Chalacay landslide (right) and the InSAR cumulative displacement time series of the pixels within the Chalacay landslide (left). The colors indicate the class to which they belong based on their cumulative displacement value, as indicated in [Figure 4.3](#)

Over the Mazar area, 71 clusters of pixels were detected. Out of the 71 clusters, 32 have one change in velocity, 28 have two changes in velocity, 8 have three

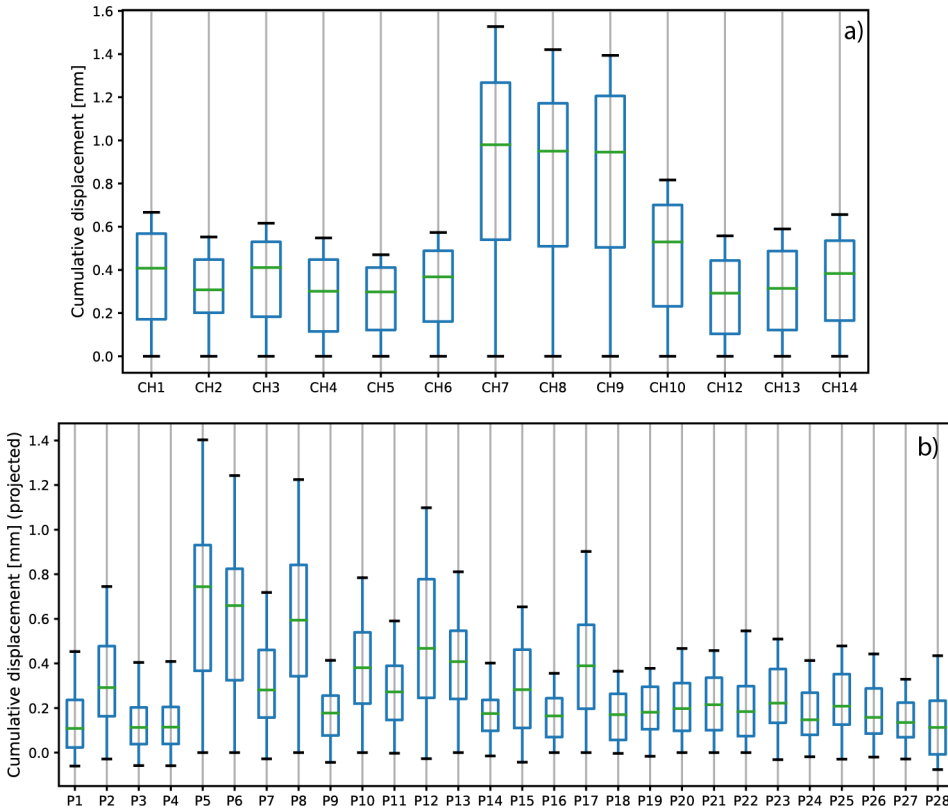


Figure 4.5: Cumulative displacement of 13 in-situ monitoring points (a) and 32 satellite-based pixels (b) in Chalacay as boxplots

changes in velocity, and 4 have four changes in velocity (Figure 4.6). The clusters with one and two changes in velocity were located relatively far from the reservoir, up on the slopes, with exceptions near the dam and on the right tributary to the main reservoir body. The four clusters with four changes in velocity were located on the toe of the slope, and the eight clusters with three changes were spread around the area, mainly far from the reservoir.

In order to visualize the evolution of the 71 clusters' velocities over time, we used a heatmap of monthly normalized velocities (Figure 4.7a). A value above 1 (orange, purple) indicates a cluster moving faster than the average, while a value below 1 (orange, yellow) indicates a cluster moving slower than the average. Overall, two-thirds of clusters were moving at high velocities at the beginning of the period. This number decreased over 12 months until 02-2018, which was

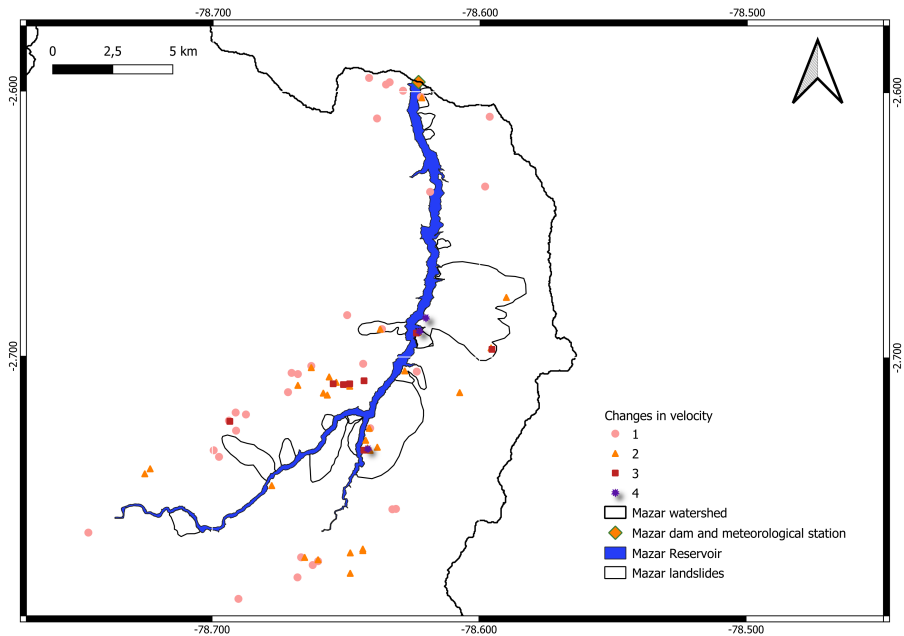


Figure 4.6: Location of the detected clusters on the slopes of the Mazar area

when most clusters moved with low velocities for three months. From 07-2018 to 01-2019, the number of clusters increased again, reaching up to one-third of them moving fast. After 01-2019, this number decreased again over nine months until 10-2019 and increased after 10-2019. Most of the clusters in this last period moved slowly.

Since most of the clusters have one or two changes in velocity, we also analyzed, per month, the normalized velocities of the 71 clusters categorized by the number of changes in velocity. This overview revealed that most of the high velocities observed at the beginning of the period were related to the clusters with only one change in velocity (Figure 4.7b). Almost half of the identified clusters moved fast for the first months until a deceleration occurred. Then the 32 clusters moved with a constant low velocity until the end of the period. In Figure 4.7c, we observe that most of the clusters with two changes in velocity moved with average and high velocities during the entire period. High velocities were mainly observed during 06-2018 and 09-2019. Figure 4.7e shows a similar behaviour, with its three clusters having high velocities during 06-2018 and 06-

2019, and also during 06-2017 and 06-2018. Clusters with three changes in velocities showed average and high velocities from the beginning until 06-2018, where the number of clusters moving fast decreased. After 10-2019, the number of clusters moving fast increased again (Figure 4.7d).

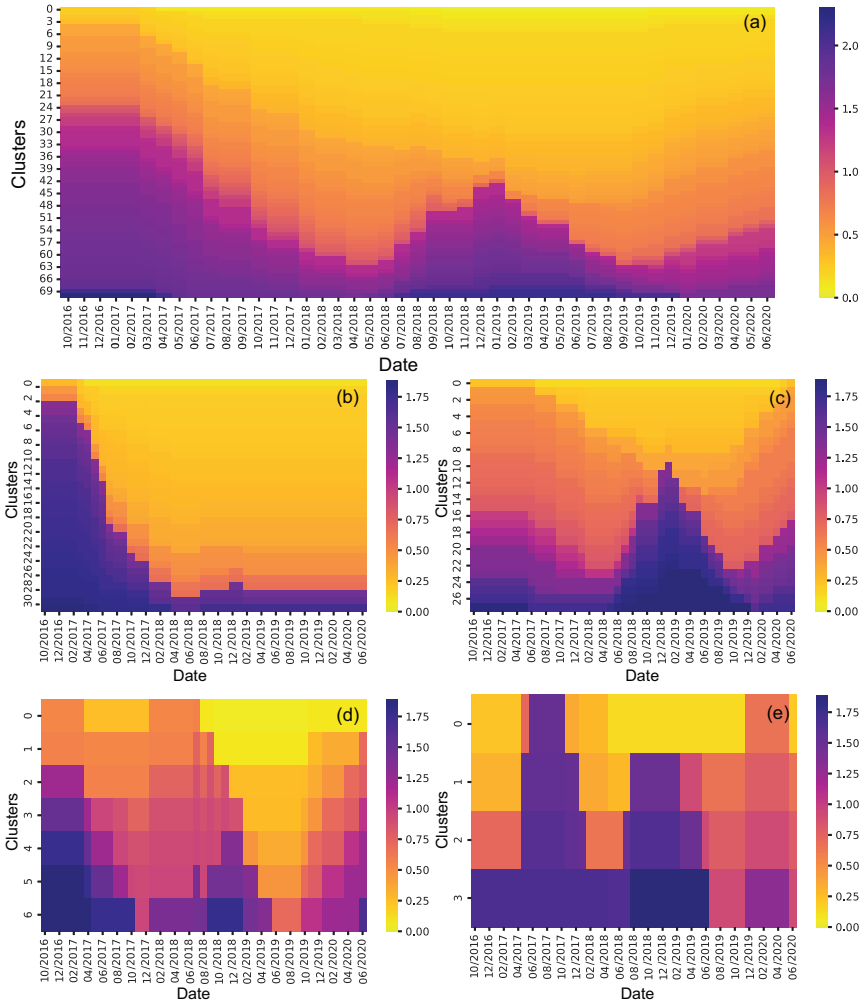


Figure 4.7: Heatmap of normalized velocities of (a) 71 clusters identified on the landslides around the Mazar reservoir, (b) 32 clusters with one change in velocity, (c) 28 clusters with two changes in velocity, (d) 8 clusters with three changes in velocity, and (e) 3 clusters with four changes in velocity. The color bar indicates the value of normalized velocity relative to the average per cluster per month

For the multiple regression analysis, we extracted, per month, the percentage of clusters moving with above-average velocities. This time series was used as the dependent variable for the multiple regression analysis.

4.5.2. HYDROMETEOROLOGICAL ANALYSIS

We used seven hydrometeorological variables to perform the multiple regression analysis. We used in-situ rainfall from the Mazar station, effective rainfall, reservoir levels, and satellite-derived soil moisture. Using the in-situ rainfall, we calculated API, P_{EMA} , and the number of high-intensity events in the basin (see subsection 4.3.2). For the API, we used antecedent precipitation of 7 days, 10 days, and 30 days. For the P_{EMA} , we used a smoothing factor of 0.1 as it gives more weight to the antecedent P_{EMA} , as shown in Equation 4.3. There are, in total, nine independent hydrometeorological variables. The results are shown in Figure 4.8 and Figure 4.9.

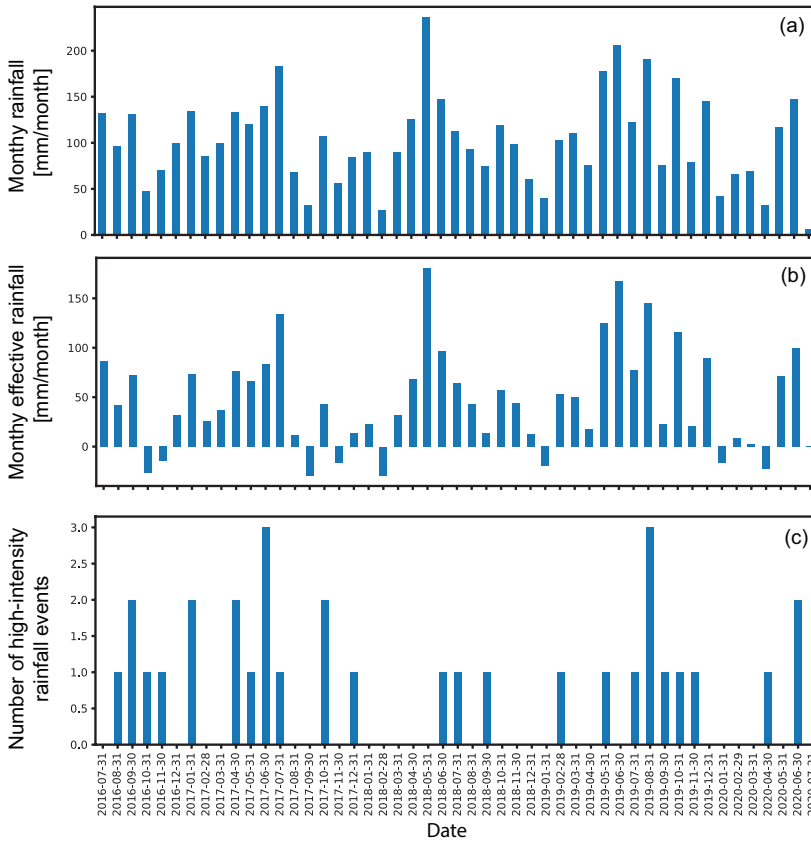


Figure 4.8: Monthly precipitation (a), monthly evapotranspiration (b), and number of high-intensity rainfall events per month (c)

4.5.3. EVALUATION OF DISPLACEMENT DATA AGAINST HYDROMETEOROLOGICAL VARIABLES

In the multiple regression analysis, the displacement data, as a time series of the percentage of clusters moving fast, is the dependent variable, while the nine hydrometeorological variables are the independent variables. Before the multiple regression analysis took place, we performed a correlation analysis between all independent variables to guarantee that these variables were not correlated. Correlated independent variables were not used in the same multiple-regression model.

Figure 4.10 shows that the independent input variables derived from rainfall were highly correlated. Effective rainfall, API 7 days, API 10 days, and API 30 days

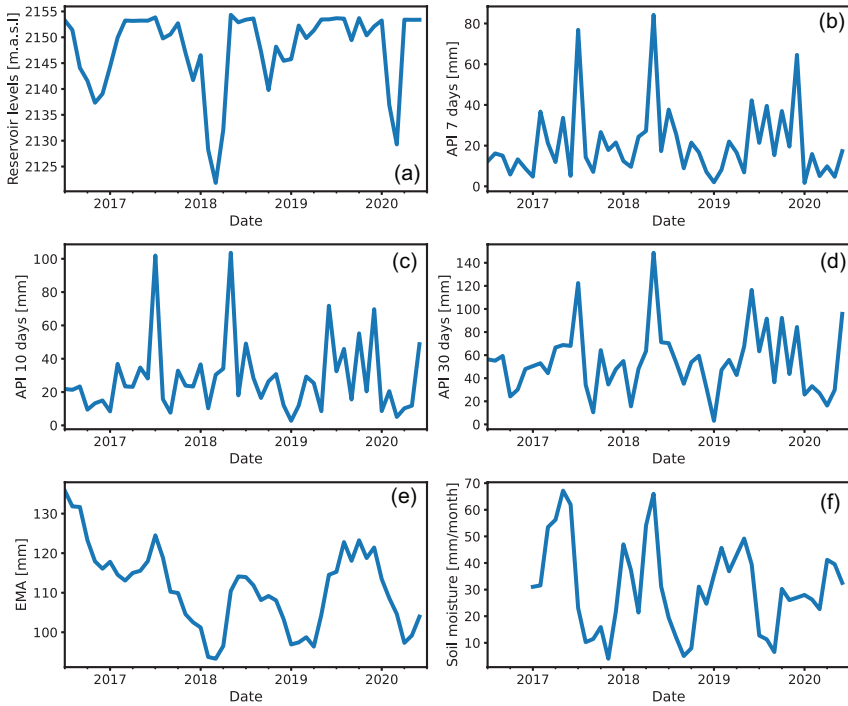


Figure 4.9: Monthly reservoir levels (a), API 7 days (b), API 10 days (c), API 30 days (d), P_{EMA} (e), and Soil moisture (f)

have a Pearson correlation coefficient higher than 0.6 with rainfall and among each other. The correlations between the dependent and independent variables are weak, 0.3 being the highest between P_{EMA} and displacement.

Considering these results, 85 multiple regression models were evaluated. We modeled the number of the fastest-moving clusters per month, using all 71 clusters together. We also used the 71 clusters split into the classified groups of clusters depending on the number of changes in velocity they have (i.e., 32 clusters with one change in velocity, 28 clusters with two changes in velocity, and 8 clusters with three changes in velocity). Consequently, we constructed the 85 models four times. We did not construct the models using the group of clusters with four changes in velocity since it was composed only of 3 clusters. Each model had four R^2 , each representing the model's goodness of fit per cluster group. Then, we selected the maximum R^2 per model and identified to which group they belong (i.e., group of clusters with one, two, or three changes in velocity

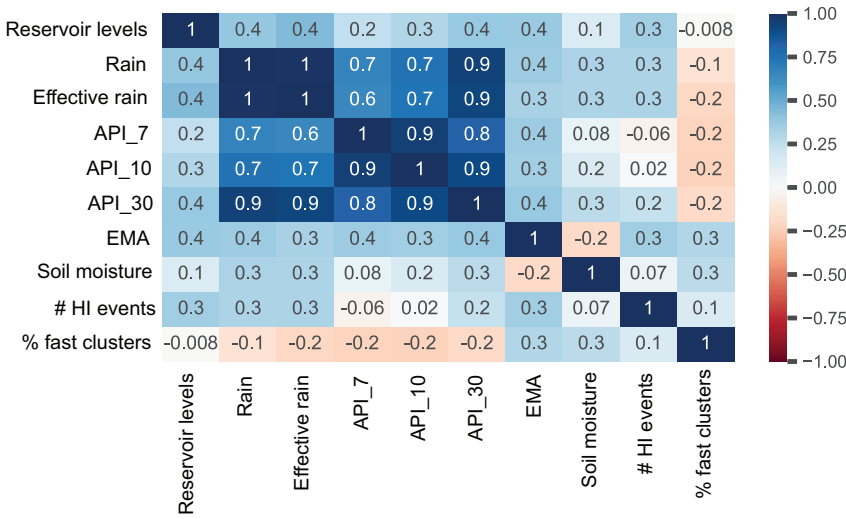


Figure 4.10: Correlations between hydrometeorological and relative velocity data

or all 71 clusters). In [Figure 4.11](#), we showed the distribution of the maximum R^2 per model and cluster group and classified them per number of variables in the model. In general, the multiple regression models show a modest R^2 (coefficient of determination), which indicates that they do not fit the distribution of the number of fast-moving clusters per month. We observed that models with two and three changes in velocity had the lowest R^2 , reaching up to 0.25. Models with one change in velocity had the highest R^2 and performed better with more variables. The highest R^2 was 0.44 in a model with five variables belonging to the cluster group with one change in velocity. The model has reservoir levels, effective rainfall, P_{EMA} , soil moisture, and the number of high-intensity events as independent variables.

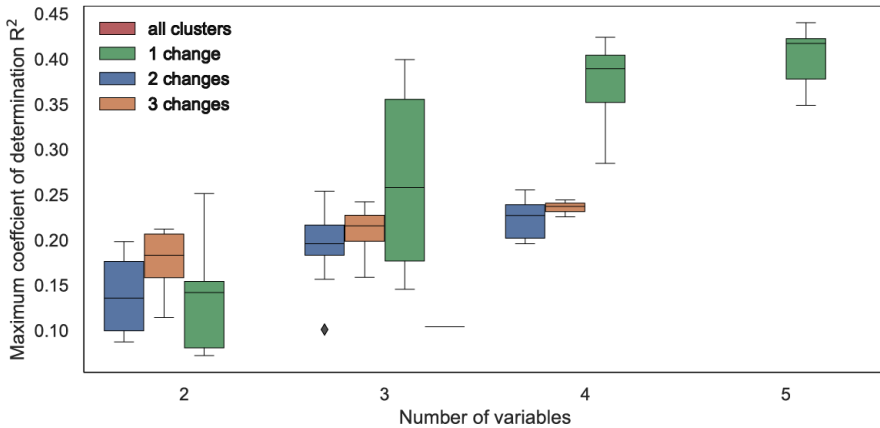


Figure 4.11: Maximum coefficients of determination R^2 of all 85 models, classified according to their number of variables and the group of pixels to which they belong

4.6. DISCUSSION

In our analysis, we compared the InSAR displacement data set to in-situ displacement recorded in the Chalacay landslide. Our findings revealed that the InSAR-derived and the in-situ cumulative displacements were coherent and of the same order of magnitude (Figure 4.5). Additionally, the location of the fastest InSAR-derived pixels coincided with the location of the in-situ monitoring points with a higher cumulative displacement rate from 2016 to 2020. This result indicates that both products provide a consistent view of the displacement in the area. Miele et al. (2021) also showed that InSAR data could accurately monitor slope deformations in south Ecuador, close to the Mazar reservoir.

Rainfall data in the study area was scarce. There was only one in-situ monitoring station at the Mazar dam, which had a significant gap in its time series. This situation led to sourcing rainfall data from satellites. However, satellite rainfall estimations in the Ecuadorian tropical Andes are often biased or erroneous due to various climatic drivers that result in varied spatiotemporal precipitation patterns (Chavez and Takahashi, 2017; Manz et al., 2017; Erazo et al., 2018). Additionally, the use of these products is often restricted due to the short length of satellite records. Studies have attempted to produce high-resolution precipitation datasets in Ecuador and Peru (e.g., Fernandez-Palomino et al. (2022)); however, they found that it is still challenging to reproduce rainfall patterns, espe-

cially in specific areas of the Ecuadorian Andes. Considering these limitations, we decided to infill in-situ rainfall from the Mazar station with in-situ rainfall from the Guarumales meteorological station, located ~20 km downstream of the Mazar dam, and use it as a hydrometeorological forcing for the analysis.

We used a multiple regression analysis to construct 85 models using all hydrometeorological and geodetical variables. Unfortunately, none of these models could reproduce the displacement time series observed in the area. The highest coefficient of determination (R^2) was 0.44 between the velocities of the group of clusters with only one change in velocity per month and the following variables: effective rainfall, reservoir levels, P_{EMA} , soil moisture, and the number of high-intensity events. In this case, P_{EMA} is the variable with the most significant influence on the model. As we observed in [Figure 4.9e](#), P_{EMA} 's values decreased during the period in which we observed a significant decrease in the number of fast-moving clusters ([Figure 4.7b](#)). Still, a low R^2 indicates that the model does not represent the dependent variable.

Most of the observed clusters (60 out of 71) had one or two changes in velocity over the four years of analysis and were distributed over the entire area. This behavior could not be linked to the seasonal hydrometeorological changes considered in this study. In the previous chapter, we took specific considerations when defining the InSAR time series to inventory changes in velocity, which could be hindering the capability of the method we used. For instance, we considered a standard methodology to generate InSAR time series without additional processing steps (i.e., without a manual inspection and removal of poor quality interferograms that have low coherence) since our goal was to determine if this generic product could be applied for regional landslide monitoring. Nevertheless, without additional InSAR processing, the generic displacement time series might only show the most significant changes in velocity, while the smaller, likely seasonal changes might be hidden within the noise in the time series. [Cohen-Waeber et al. \(2018\)](#) showed that by applying independent and principal component analysis to the InSAR displacement time series, spatial and temporal displacement patterns were revealed and were related to seasonal pore-pressure changes.

In this analysis, we constructed a normalized velocity time series per clus-

ter of pixels for all pixels. We did it so each cluster represents an area that is consistently moving and to reduce the amount of data in the multiple regression models, i.e., we derived 71 time series (for the 71 clusters) from the 3230 time series (from the 3230 pixels). The normalized time series of each cluster was obtained by calculating the median velocity of all time series within that cluster. Even though this approach represents the overall velocity of that cluster quite well, the timing of the change in velocity of each pixel within a cluster was not always consistent (e.g., 11 out of 32 clusters with one change in velocity had the timing of this change within 6 months or less, the rest of clusters had a timing of change in velocity greater than 6 months, and up to ~2 years). This situation is common in clusters with one and two changes in velocity. Clusters with a varying time in velocity change might lead to uncertainties within the multiple regression models.

Slow-moving landslides have been studied at local and regional scales. Most of the studies at the local scale have been able to relate the acceleration patterns to seasonal hydrometeorological changes (e.g., [Herrera et al. \(2013\)](#)) and in-situ disturbances such as road deformations (e.g., [Nappo et al. \(2019\)](#)). Similarly, in [chapter 3](#), we showed that the accelerations and decelerations in the Mud Creek landslide were related to seasonal rainfall. At the regional scale, however, more factors are at play, and while some have found seasonal accelerations and decelerations driven by rainfall (e.g., [Zhang et al. \(2018\)](#)), anthropogenic activities and specific local conditions may cause different velocity patterns within the same landslide body or among the same landslide complex ([Herrera et al., 2013](#)).

The landslides around the Mazar reservoir have individual sliding mechanisms (see [Table 4.1](#)) and have local geological, geomorphological, and hydrogeological settings. The varying timing of velocity changes observed over the area ([Figure 4.6](#)) might be related to the individual dynamics of the landslides. These landslides might respond independently to rainfall, reservoir level changes, and groundwater storage. For instance, [Kang et al. \(2021\)](#) indicated that the sliding mechanisms of the landslides along the Highway 50 corridor were closely related to pore-water pressures to which each landslide was linked. The effect of the pore-water pressure on a landslide depended on the depth of the sliding surface, precipitation, and hydrogeological factors such as hydraulic conductivity

and diffusivity (Hu et al., 2019; Xu et al., 2019). Therefore, landslides in the same region but with heterogeneous local settings respond differently to hydrometeorological forcings, such as precipitation (Hu et al., 2018; Zhao et al., 2018).

4.7. CONCLUSION

The objective of this chapter was to identify and model the timing and frequency of velocity changes of clusters of pixels and to investigate whether they are correlated with hydrometeorological forcings. We used InSAR-derived displacement data to investigate the sliding mechanisms of landslides on the slopes around the Mazar reservoir. Much of the research on slow-moving landslides has identified hydrometeorological and in-situ forcings as the main driving mechanisms for initiating or reactivating accelerations and decelerations of slow-moving landslides. In this chapter, we leveraged the InSAR-derived dynamics of the slope deformations and evaluated the possible relationship to available hydrometeorological information in the area. We performed multiple regression models using the variables above and found that the regional behavior of slow-moving landslides could not be correlated to the hydrometeorological factors of the area.

Our analysis suggests that hydrology alone is insufficient to explain the behavior of slow-moving landslides in the region, as most clusters exhibit little to no seasonal dynamics (one or two velocity changes) over four years. This can be due to the lack of in-situ information, such as groundwater and soil moisture, which would allow for a more comprehensive analysis of all the factors that can affect the displacements. Additionally, the fact that most of the clusters have one or two changes in velocity over four years of analysis may indicate that small changes in velocity were hidden within the noise of the generic InSAR displacement time series. Even though we were able to find temporally and spatially consistent clusters of pixels, most of them showed heterogeneous timing of changes in velocity, which brings uncertainty to the multiple regression models.

A regional analysis of this kind is challenging to perform in the presence of heterogeneous landslide mechanisms, where slopes seem to respond differently to the same regional inputs. Therefore, in order to evaluate the effect of hydrometeorological forcings in the area, a detailed analysis of local slope settings and mechanisms must be coupled with the surficial dynamics observed using

our method. In conclusion, our findings suggest that more in-depth research is needed to understand better the complex processes contributing to landslides in the Mazar region. This study provides a foundation for future investigations.

5

SYNTHESIS AND CONCLUSIONS

The Andes mountain range is a relatively young geological formation. As such, it is prone to instabilities due to tectonic activity, or high precipitation amounts (especially in the northern Andes), among other factors. This is no exception in Ecuador, as the Andes traverse the country's continental region, dividing it into three distinct geomorphological areas. Precipitation levels vary across Ecuador, ranging from ~700 mm to ~2000 mm per year in the southern coast and highlands and from ~2000 mm to ~3000 mm per year in the northern coast and the Amazon region of Ecuador.

Our study area is in southeast Ecuador, a transitional zone between the Andes and the Amazon rainforest. This region is characterized by slow-moving landslides that have been identified and monitored for many years. These landslides gained increased significance following the construction of the Mazar dam and subsequent impoundment of the Mazar reservoir in 2010. The interaction between the geological dynamics of the Andes and the unique environmental conditions in this region has contributed to the development and persistence of these slow-moving landslides, making them a focal point of investigation and concern.

The main objective of this dissertation was to develop a systematic approach to identify the onset of accelerations and decelerations, their physical causes, and the influence of hydrometeorological factors on the landslides near the Mazar reservoir in southeast Ecuador. Specifically, we addressed the following objectives:

1. To perform a hydrogeological characterization of the Guarumales landslide at the local scale while considering its broader implications within the Mazar region;
2. To develop a new methodology to identify accelerations and decelerations of slow-moving landslides at the regional scale using InSAR displacement time series, and apply it on the landslides around the Mazar reservoir;
3. To analyze the detected accelerations and decelerations of the landslides in the Mazar region and explore the influence of hydrometeorological forcings on the dynamics of the landslides.

These three specific objectives will be discussed in [section 5.1](#), [section 5.2](#), and [section 5.3](#). [Section 5.4](#), [section 5.5](#), and [section 5.6](#) offer a broader overview of the findings of this thesis and the associated limitations and future work.

5.1. GUARUMALES CASE STUDY

First, we proposed a hydrogeological characterization of the Guarumales landslide, located approximately 20 kilometers downstream from the Mazar dam and subjected to extensive monitoring. This investigation aimed to comprehend the specific dynamics of a landslide at a local scale while considering its broader implications within the Mazar region.

A comprehensive dataset was readily available to facilitate the characterization of the Guarumales landslide. This dataset encompassed a remarkable eighteen-year collection of in-situ displacement data from 2001 to 2018 and rainfall and groundwater level data spanning from 2013 to 2018. The displacement data analysis revealed consistent surface movement rates while highlighting rainfall's profound influence on the groundwater system. However, due to the limited detail in the displacement data records, it was not feasible to ascertain a direct correlation between the displacement rates and changes in the pore water pressure. Nevertheless, our investigation uncovered an essential aspect of the Guarumales landslide's slow-moving behavior: the horizontal drains installed across the slope area drain 12% of the total annual rainfall. This excess of water would cause a rise in the groundwater level of up to ~0.5 m, adding to the driving forces of the landslide. This shows commendable management practices employed by CELEC-EP in effectively mitigating the adverse effects associated with the variations on the movement of the Guarumales landslide.

The conceptual model of the Guarumales landslide provided valuable insights into the intricate hydrogeological characteristics of this landslide within the broader context of the Mazar region. The presence of perched groundwater systems, giant boulders within the colluvium system, and fractures and cracks in the slope collectively contributed to the complexities encountered while analyzing the Guarumales landslide. The limited spatial distribution of the in-situ monitoring points further restricted the interpretation of landslide behavior. Since 2020, according to communications with CELEC-EP, an early-warning system

primarily based on rainfall patterns has been developed for the Guarumales landslide in response to fast-moving landslides, particularly near the small streams within Guarumales. This system is a precautionary measure to enhance preparedness and response to potential fast-moving landslide events, such as debris flows.

In conclusion, we were able to perform a hydrogeological characterization of the Guarumales landslide. We identified the main geological features and the hydrological responses of groundwater to rainfall. However, we were not able to identify a clear relationship between the landslide movement and the driving mechanisms underlying the Guarumales landslide. Given the limitations encountered in the case study of the Guarumales landslide and the absence of comprehensive in-situ information relating to the slopes surrounding the Mazar reservoir, we developed a new method to investigate the dynamics of the Mazar region.

5.2. DEVELOPMENT OF A METHOD TO DETECT ACCELERATIONS AND DECELERATIONS FROM INSAR DISPLACEMENT TIME SERIES

Chapter 3 centred on the comprehensive examination of the Mazar region encompassing the vicinity of the Mazar reservoir. We used InSAR-derived displacement time series over the Mazar region and developed a systematic method to detect, quantify, and inventory changes in the surface deformation rate of slowly deforming areas. We identified the fastest-moving InSAR pixels and analyzed the time series associated with those pixels. The outcome was a comprehensive inventory of the occurrences of accelerations and decelerations derived from the InSAR displacement time series. Considering the temporal resolution limitations imposed by the satellite's orbit time, typically 6 to 12 days, we opted for a monthly timescale for our analysis.

Furthermore, our analysis considered the presence of uncertainties associated with the timing of detected accelerations and decelerations. We set a maximum permissible uncertainty of 30 days. An uncertainty threshold greater than 30 days results in the identification of more accelerations and decelerations, but

such an extended time frame would make the analysis less meaningful in capturing the temporal dynamics of the slow-moving slopes. Any threshold longer than the duration of a (wet) season does not give useful information about the temporal dynamics of the slow-moving slopes.

We tested our method in the Mudcreek landslide in the United States. We used the InSAR displacement time series from a previous study, which had undergone a rigorous evaluation process, resulting in a high-quality dataset. Our analysis successfully identified monthly accelerations and decelerations that corresponded to periods of intense rainfall and drought, respectively. The results demonstrated the method's capability to detect and quantify the temporal dynamics of the landslide accurately.

After this successful test, we applied the method to the Mazar region. In this case, the quality of the time series data was considerably lower compared to the Mudcreek landslide dataset. Despite this limitation, our analysis identified deforming areas with complex acceleration and deceleration patterns within and between groups of pixels. Somewhat surprisingly, the identified variations did not consistently align with the wet and dry seasons, indicating the presence of additional factors influencing the deformations within the Mazar region.

Overall, we developed a new method to detect surface accelerations and decelerations at the regional scale and used it on the slopes near and around the Mazar reservoir. We leveraged the temporal and spatial variation of velocity changes of slow-moving deforming areas to interpret their dynamics at the large scale. Ultimately, we used our inventory of surface displacement rate changes to investigate the dynamics of slow-moving landslides at both sub-landslide and regional scales with high spatial and temporal resolution.

5.3. ANALYSIS OF THE DETECTED ACCELERATIONS AND DECELERATIONS IN THE MAZAR REGION

In [chapter 4](#), we used the surface displacement rate changes results ([chapter 3](#)) to identify the timing and frequency of velocity changes of the landslides in the Mazar reservoir area and to investigate whether they were correlated with hydrometeorological forcings from October 2016 to July 2020 through multiple lin-

ear regression analysis. Our analysis revealed the presence of distinct clusters of pixels exhibiting varying surface displacement dynamics across the Mazar region. These dynamics were characterized by a different number of velocity changes, ranging from one to four, observed within the identified clusters. Despite our efforts, we were not able to find a significant correlation between the landslide dynamics and the seasonal behavior of hydrometeorological forcings in the study area. In hindsight, this was probably not a huge surprise as most of the clusters of pixels exhibited only one or two changes in velocity over the four years of data analysis, irrespective of the seasonal variations in hydrometeorological forcings.

The velocity changes of the identified clusters over the Mazar area were derived from the InSAR-based displacement time series generated in [chapter 3](#). These time series were created using a standard methodology without any extensive investigation of the individual interferograms used in their generation. The primary objective was to determine whether the approach developed on [chapter 3](#) enabled a reasonable interpretation of the slow-moving dynamics at the regional scale. It is concluded that the standard methodology employed in generating the displacement time series has limitations. The methodology identifies the most significant velocity changes, which potentially misses smaller (likely seasonal) changes that may be hidden in the noise present in the time series.

Given the identified variations in dynamics across the Mazar area and the limited availability of hydrometeorological data, it became evident that hydrology alone cannot adequately explain the behavior of the slow-moving landslides in the region. The absence of essential in-situ information, such as groundwater and soil moisture measurements, coupled with the potential influence of anthropogenic disturbances, prevented a more comprehensive analysis of all the factors possibly influencing the sliding mechanisms. It became apparent that slopes within the same region responded differently to the same regional inputs, suggesting the effect of local site-specific factors. A full analysis of the surficial dynamics identified with our methodology requires knowledge of local slope settings and mechanisms. Such an analysis may enable a more accurate evaluation of the effect of hydrometeorological forcings in the area.

In conclusion, we analyzed the resulting inventory of accelerations and decelerations from [chapter 3](#) and evaluated the effect (if any) of the hydrometeoro-

logical forcings in the area. However, we were not able to establish a correlation between them due to the limited availability of in-situ data, as well as the limited quality of the InSAR displacement time series.

5.4. LIMITATIONS OF SLOW-MOVING LANDSLIDES RESEARCH IN THE CONTEXT OF THE ANDES MOUNTAIN RANGE

Our study highlighted the limited availability of information in the Ecuadorian Andes when analyzing slow-moving landslides as natural hazards. While we were able to establish connections between rainfall patterns and groundwater responses, such as in the Guarumales case study, we encountered challenges in identifying empirical relationships between displacement (whether derived from in-situ measurements or satellite data) and the hydrometeorological forcings at both the local scale (Guarumales) and regional scale (Mazar region). One major limitation was the lack of sufficient detail in the displacement time series to represent the slopes' dynamics accurately. In the case of the Guarumales study, the spatio-temporal resolution of the in-situ monitoring points was inadequate to capture the slow-moving seasonal dynamics of the slope. Similarly, while providing extensive spatio-temporal data for the Mazar region, the satellite-based displacement time series likely focused on capturing the most significant velocity changes. As a result, most clusters of pixels exhibited only one or two velocity changes over the four-year analysis period.

Another significant limitation was the availability of in-situ hydrometeorological data, particularly at the regional scale. Although daily reservoir water level data were accessible throughout our study period, obtaining comprehensive in-situ rainfall data posed challenges. In-situ rainfall data was only available for one station at the Mazar dam, for which we had to do an intrastation interpolation due to the data gaps in the time series. We utilized satellite data and models to derive additional hydrometeorological variables to supplement the limited in-situ data. Satellite data allowed us to estimate soil moisture levels, providing valuable insights into the moisture content of the slopes. Furthermore, we employed models to estimate evapotranspiration, which enabled a more comprehensive analysis of the hillslope water balance and its impact on the dynamics

of slow-moving landslides. It is important to acknowledge that these alternative data sources and modeling approaches introduced certain limitations and uncertainties. Satellite-based measurements and model outputs are subject to inherent inaccuracies and approximations, which must be carefully considered when interpreting and using the derived datasets.

The limitations identified in this study are closely tied to the broader data availability constraints observed in the Andes region. It is worth noting that many worldwide studies rely on satellite-derived data, such as InSAR-derived displacement data, to monitor slow-moving landslides (Bordoni et al., 2018; Berti et al., 2013; Raspini et al., 2019). However, most of these studies have been conducted in the global north, encompassing regions like the United States, Europe, and Asia (Lacroix et al., 2020b). Consequently, the calibration of these satellite products is predominantly based on these locations. As a result, obtaining accurate satellite acquisitions for the global south, including underdeveloped areas, poses significant data acquisition and validation challenges. This was evident in our study regarding the InSAR displacement data acquired and processed for the Mazar region, as discussed in chapter 3. Similarly, Appendix A revealed notable dissimilarities between the satellite-derived and in-situ recorded rainfall data for the Mazar region.

Throughout this thesis, a recurring limitation has been the limited availability of in-situ data within the area of interest. Even though in-situ data has been collected for several years, their frequency and accuracy were too coarse for detailed analysis of the hydromechanical mechanisms of the Mazar deformations. The available data collected for the Guarumales case study proved insufficient in capturing the detailed dynamics of the slopes. Furthermore, the absence of comprehensive in-situ data in the Mazar region compelled us to rely on satellite-derived displacement data for the regional analysis. The overall quality of the processed displacement data, combined with the limited number of available meteorological stations and the lack of in-situ hydrological data, impeded our ability to establish a clear correlation between slope displacement in the Mazar region and the hydrometeorological forcings influencing the area. It is important to highlight the need to improve the spatio-temporal resolution of the local monitoring systems to capture the velocity variations of the slowly deforming areas of

the Mazar region.

5.5. SLOW-MOVING LANDSLIDES IN THE ECUADORIAN ANDES

The current management practices implemented by CELEC-EP in the Mazar region involve on-site monitoring of the identified landslides in the vicinity of the Mazar dam and reservoir, as well as a focus on understanding the geological characteristics of these landslides. The monitoring has been carried out using a Total Station, measuring every two weeks at specific locations within the locally identified landslides. However, due to unforeseen circumstances such as bad weather, instrument failure, or human errors, these monitoring campaigns are not always carried out. This leads to having coarse in-situ data, both spatially and temporally. Our research showed that this coarse in-situ data is insufficient to perform a detailed analysis of the slow-moving dynamics of the slopes in the Mazar region. For a better insight in these dynamics, and thus, a reliable landslide early-warning system, it is imperative to improve the spatio-temporal resolution of the in-situ monitoring systems. Some alternatives to improve the in-situ monitoring systems are the use of Terrestrial Laser Scanning, or detailed LIDAR data over the area of interest.

In line with these efforts, our work complemented these field-based activities by identifying additional areas undergoing deformation that had not been identified previously. This approach facilitates collaboration between in-situ observations and monitoring and the satellite-derived identification of potentially unstable areas. At the local scale, our research successfully identified the effectiveness of the current management plans, particularly in preventing the accumulation of groundwater that could lead to catastrophic consequences.

If studies on landslide hazard assessment increasingly focus on less economically developed countries, valuable information regarding landslide monitoring can be obtained in these areas, which often face a higher vulnerability to the impacts of this natural hazard (Lacroix et al., 2020b). In Ecuador, constructing hydropower dams has become a priority within the country's energy sector development plans (Mite-León and Barzola-Monteses, 2018; Barzola-Monteses et al., 2019). However, we have observed a significant gap in data availability and the extent of research conducted on landslide hazards in the Ecuadorian Andes.

Given the growing emphasis on hydropower development, it is crucial to prioritize landslide hazard assessments in these areas to prevent potentially catastrophic consequences. The combination of infrastructure development, such as dams, and the presence of landslide-prone regions highlights the importance of understanding and effectively managing the associated risks.

Over the first half of 2023, many landslides have impacted Ecuador. Some examples include the slow-moving landslides in southern Ecuador, i.e., Santa Isabel, Tarqui, Cañar, and Alausí. The catastrophic failure of the slow-moving landslide in Alausí on March 26, 2023, resulting in the displacement of three million cubic meters of material over 24 hectares, has had devastating consequences (Flores et al., 2023). The loss of 65 lives and the remaining ten missing individuals further emphasize the event's severity. Reports indicate that cracks had already started to appear in December 2022, and by March 15, 2023, the area was on yellow alert. Although monitoring was reportedly in place, it could not anticipate the occurrence of the catastrophic failure in March.

5

5.6. FUTURE WORK

By studying and calibrating satellite-derived products more frequently in the global south, specifically in regions prone to landslides, such as Ecuador, it becomes possible to apply methodologies similar to the one described in this thesis. This can lead to more accurate monitoring of slow-moving landslides and enable the modeling of acceleration patterns before catastrophic failures occur. Addressing data availability and calibration limitations in these regions is crucial to advance our understanding of slow-moving landslide dynamics, improve hazard assessment, and develop more effective mitigation strategies.

Through comprehensive research and enhanced monitoring techniques, we can strive to minimize the future loss of life and property associated with landslides. It is essential to prioritize investments in monitoring infrastructure, data collection, and research initiatives to mitigate the risks posed by these natural hazards and enhance the resilience of communities living in landslide-prone areas.

REFERENCES

- Alcántara-Ayala, I., Oliver-Smith, A., 2014. Icl latin-american network: on the road to landslide reduction capacity building. *Landslides* 11, 315–318.
- Alho, C.J.R., 2011. Environmental effects of hydropower reservoirs on wild mammals and freshwater turtles in amazonia: a review .
- Allen, R.G., Pereira, L.S., Raes, D., Smith, M., 1998. Crop evapotranspiration-guidelines for computing crop water requirements-fao irrigation and drainage paper 56. Fao, Rome 300, D05109.
- Almeida, E., Charpentier, J., Ramon, P., 1997. Evaluación de la dinámica del deslizamiento guarumales.
- An, H., Viet, T.T., Lee, G., Kim, Y., Kim, M., Noh, S., Noh, J., 2016. Development of time-variant landslide-prediction software considering three-dimensional subsurface unsaturated flow. *Environmental modelling software* 85, 172–183.
- Anderson, M.G., Lloyd, D.M., 1991. Using a combined slope hydrology-stability model to develop cut slope design charts. *Proceedings of the Institution of Civil Engineers* 91, 705–718.
- Argentino, A.S.G.M., Andino, P.M., et al., 2007. Movimientos en masa de la región andina: Una guía para la evaluación de amenazas .
- Aristizábal, E., Martínez-Carvajal, H., García-Aristizábal, E., 2017. Modelling shallow landslides triggered by rainfall in tropical and mountainous basins, in: *Advancing Culture of Living with Landslides: Volume 4 Diversity of Landslide Forms*, Springer. pp. 207–212.
- Aryal, A., Brooks, B.A., Reid, M.E., Bawden, G.W., Pawlak, G.R., 2012. Displacement fields from point cloud data: Application of particle imaging velocimetry to landslide geodesy. *Journal of Geophysical Research: Earth Surface* 117.

- Askarinejad, A., Springman, S.M., 2017. A novel technique to monitor subsurface movements of landslides. *Canadian Geotechnical Journal* 55, 620–630. doi:[10.1139/cgj-2016-0338](https://doi.org/10.1139/cgj-2016-0338).
- Bagwari, S., Gehlot, A., Singh, R., Thakur, A.K., 2021. Rainfall induced landslide monitoring system. *International Journal on Engineering Applications (I.R.E.A.)* 9. doi:[10.15866/irea.v9i1.19543](https://doi.org/10.15866/irea.v9i1.19543).
- Baize, S., Audin, L., Winter, T., Alvarado, A., Moreno, L.P., Taïpe, M., Reyes, P., Kauffmann, P., Yepes, H., 2015. Paleoseismology and tectonic geomorphology of the pallatanga fault (central ecuador), a major structure of the south-american crust. *Geomorphology* 237, 14–28.
- Bakker, M., Schaars, E., 2019. Solving groundwater flow problems with time series analysis: you may not even need another model. *Groundwater* 57, 826–833.
- Barla, G., Paronuzzi, P., 2013. The 1963 vajont landslide: 50th anniversary .
- Barzola-Monteses, J., Mite-León, M., Espinoza-Andaluz, M., Gómez-Romero, J., Fajardo, W., 2019. Time series analysis for predicting hydroelectric power production: The ecuador case. *Sustainability* 11, 6539.
- Bayer, B., Simoni, A., Mulas, M., Corsini, A., Schmidt, D., 2018. Deformation responses of slow moving landslides to seasonal rainfall in the northern apennines, measured by insar. *Geomorphology* 308, 293–306. doi:[10.1016/j.geomorph.2018.02.020](https://doi.org/10.1016/j.geomorph.2018.02.020).
- Beck, H.E., Van Dijk, A.I.J.M., Levizzani, V., Schellekens, J., Miralles, D.G., Martens, B., De Roo, A., 2017. Mswep: 3-hourly 0.25 global gridded precipitation (1979–2015) by merging gauge, satellite, and reanalysis data. *Hydrology and Earth System Sciences* 21, 589–615.
- Beck, H.E., Wood, E.F., Pan, M., Fisher, C.K., Miralles, D.G., Van Dijk, A.I.J.M., McVicar, T.R., Adler, R.F., 2019. Mswep v2 global 3-hourly 0.1 precipitation: methodology and quantitative assessment. *Bulletin of the American Meteorological Society* 100, 473–500.

- Bekaert, D.P.S., Handwerger, A.L., Agram, P., Kirschbaum, D.B., 2020. InSAR-based detection method for mapping and monitoring slow-moving landslides in remote regions with steep and mountainous terrain: An application to nepal. *Remote Sensing of Environment* 249, 111983.
- Belle, P., Aunay, B., Lachassagne, P., Ladouche, B., Join, J.L., 2018. Control of tropical landcover and soil properties on landslides' aquifer recharge, piezometry and dynamics. *Water* 10, 1491.
- Bennett, G.L., Roering, J.J., Mackey, B.H., Handwerger, A.L., Schmidt, D.A., Gullod, B.P., 2016. Historic drought puts the brakes on earthflows in northern california. *Geophysical Research Letters* 43, 5725–5731.
- Berardino, P., Fornaro, G., Lanari, R., Sansosti, E., 2002. A new algorithm for surface deformation monitoring based on small baseline differential sar interferograms. *IEEE Transactions on geoscience and remote sensing* 40, 2375–2383.
- Berti, M., Corsini, A., Franceschini, S., Iannaccone, J.P., 2013. Automated classification of persistent scatterers interferometry time series. *Natural Hazards and Earth System Sciences* 13, 1945–1958.
- Bianchini, S., Raspini, F., Solari, L., Del Soldato, M., Ciampalini, A., Rosi, A., Casagli, N., 2018. From picture to movie: Twenty years of ground deformation recording over tuscan region (italy) with satellite insar. *Frontiers in Earth Science* 6, 177.
- Boeing, G., 2018. Clustering to reduce spatial data set size. arXiv preprint arXiv:1803.08101 .
- Bogaard, T., Greco, R., 2018. Invited perspectives: Hydrological perspectives on precipitation intensity-duration thresholds for landslide initiation: proposing hydro-meteorological thresholds. *Natural Hazards and Earth System Sciences* 18, 31–39.
- Bogaard, T.A., Greco, R., 2016. Landslide hydrology: from hydrology to pore pressure. *Wiley Interdisciplinary Reviews: Water* 3, 439–459.

- Booth, A.M., McCarley, J., Hinkle, J., Shaw, S., Ampuero, J., Lamb, M.P., 2018. Transient reactivation of a deep-seated landslide by undrained loading captured with repeat airborne and terrestrial lidar. *Geophysical Research Letters* 45, 4841–4850.
- Bordoni, M., Bonì, R., Colombo, A., Lanteri, L., Meisina, C., 2018. A methodology for ground motion area detection (gma-d) using a-dinsar time series in landslide investigations. *Catena* 163, 89–110.
- Borrelli, L., Nicodemo, G., Ferlisi, S., Peduto, D., Di Nocera, S., Gullà, G., 2018. Geology, slow-moving landslides, and damages to buildings in the verbicaro area (north-western calabria region, southern italy). *Journal of Maps* 14, 32–44.
- Bounab, A., El Kharim, Y., El Hamdouni, R., Hlila, R., 2021. A multidisciplinary approach to study slope instability in the alboran sea shoreline: Study of the tamegaret deep-seated slow-moving landslide in northern morocco. *Journal of African Earth Sciences* 184, 104345.
- Brönnimann, C.S., 2011. Effect of groundwater on landslide triggering. Technical Report. EPFL.
- Brückl, E., Brunner, F., Lang, E., Mertl, S., Müller, M., Stary, U., 2013. The gradenbach observatory—monitoring deep-seated gravitational slope deformation by geodetic, hydrological, and seismological methods. *Landslides* 10, 815–829.
- Burnham, K.P., Anderson, D.R., 2004. Model selection and multimodel inference. A practical information-theoretic approach 2.
- CELEC-EP, 2011. Monitoreo. informe anual 2011.
- Cevallos Andrade, L.S., 2010. Análisis de la estabilidad y diagnóstico del talud de la zona no. 2 en guarumales .
- Charpentier, J., 1996. Resultados de la interpretación inclinométrica.
- Chavez, S.P., Takahashi, K., 2017. Orographic rainfall hot spots in the andes-amazon transition according to the trmm precipitation radar and in situ data. *Journal of Geophysical Research: Atmospheres* 122, 5870–5882.

- Ciavolella, M., Bogaard, T., Gargano, R., Greco, R., 2016. Is there predictive power in hydrological catchment information for regional landslide hazard assessment? *Procedia Earth and Planetary Science* 16, 195–203.
- Cigna, E., Tapete, D., Casagli, N., 2012. Semi-automated extraction of deviation indexes (di) from satellite persistent scatterers time series: tests on sedimentary volcanism and tectonically-induced motions. *Nonlinear processes in geophysics* 19, 643–655.
- Cohen-Waeber, J., Bürgmann, R., Chaussard, E., Giannico, C., Ferretti, A., 2018. Spatiotemporal patterns of precipitation-modulated landslide deformation from independent component analysis of insar time series. *Geophysical Research Letters* 45, 1878–1887. doi:[2017GL075950](https://doi.org/2017GL075950).
- Collenteur, R.A., Bakker, M., Caljé, R., Klop, S.A., Schaars, E., 2019. Pastas: open source software for the analysis of groundwater time series. *Groundwater* 57, 877–885.
- Cotecchia, F., Santaloia, F., Lollino, P., 2011. Slow landsliding as effect of hydro-mechanical coupled processes: examples of resulting damages and mitigation strategies, in: *Proceedings of the 2nd International Workshop on Landslides*, 28–29 September, Naples, Italy.
- Crosta, G.B., Frattini, P., 2003. Distributed modelling of shallow landslides triggered by intense rainfall. *Natural Hazards and Earth System Sciences* 3, 81–93.
- Cruden, D., Varnes, D., 1996. Landslides: Investigation and mitigation. chapter 3—landslides types and processes. *Transportation research board special report* 247.
- Cui, Q., Zhang, L., Chen, X., Cao, Z., Wei, X., Zhang, J., Xu, J., Liu, D., Du, C., 2022. Quantitative risk assessment of landslides with direct simulation of pre-failure to post-failure behaviors. *Acta Geotechnica* 17, 4497–4514.
- Córdova, A., Santo, J., Córdova, A., Vaca, S., Alvarado, A., Naya, V., Singaicho, J., Ruiz, M., Yepes, H., Vallée, M., et al., 2014. Informe Sismico Para El Ecuador. Technical Report. Instituto Geofisico de la Escuela Politecnica Nacional.

- Dai, F.C., Lee, C.F., 2002. Landslide characteristics and slope instability modeling using gis, lantau island, hong kong. *Geomorphology* 42, 213–228.
- Dai, K., Peng, J., Zhang, Q., Wang, Z., Qu, T., He, C., Li, D., Liu, J., Li, Z., Xu, Q., Burgmann, R., Milledge, D.G., Tomas, R., Fan, X., Zhao, C., Liu, X., 2020. Entering the era of earth observation-based landslide warning systems: A novel and exciting framework. *IEEE Geoscience and Remote Sensing Magazine* 8, 136–153. doi:[10.1109/MGRS.2019.2954395](https://doi.org/10.1109/MGRS.2019.2954395).
- Del Soldato, M., Solari, L., Raspini, F., Bianchini, S., Ciampalini, A., Montalti, R., Ferretti, A., Pellegrineschi, V., Casagli, N., 2019. Monitoring ground instabilities using sar satellite data: A practical approach. *ISPRS International Journal of Geo-Information* 8, 307.
- Desnos, Y.L., Borgeaud, M., Doherty, M., Rast, M., Liebig, V., 2014. The european space agency's earth observation program. *IEEE Geoscience and Remote Sensing Magazine* 2, 37–46.
- Dille, A., Kervyn, F., Handwerger, A.L., d'Oreye, N., Derauw, D., Bibentyo, T.M., Samsonov, S., Malet, J.P., Kervyn, M., Dewitte, O., 2021. When image correlation is needed: Unravelling the complex dynamics of a slow-moving landslide in the tropics with dense radar and optical time series. *Remote Sensing of Environment* 258, 112402.
- Du, J., Yin, K., Lacasse, S., 2013. Displacement prediction in colluvial landslides, three gorges reservoir, china. *Landslides* 10, 203–218.
- Díaz, G., Arriagada, P., Górski, K., Link, O., Karelavic, B., Gonzalez, J., Habit, E., 2019. Fragmentation of chilean andean rivers: expected effects of hydropower development. *Revista chilena de historia natural* 92, 1–13.
- ECUAELECTRICIDAD, 2000a. Informe de monitoreo e instrumentación de la central hidroeléctrica paute, noviembre 2000.
- ECUAELECTRICIDAD, 2000b. Informe de monitoreo e instrumentación de la central hidroeléctrica paute, septiembre 2000.

- Erazo, B., Bourrel, L., Frappart, F., Chimborazo, O., Labat, D., Dominguez-Granda, L., Matamoros, D., Mejia, R., 2018. Validation of satellite estimates (tropical rainfall measuring mission, trmm) for rainfall variability over the pacific slope and coast of ecuador. *Water* 10, 213.
- Ester, M., Kriegel, H.P., Sander, J., Xu, X., et al., 1996. A density-based algorithm for discovering clusters in large spatial databases with noise., in: *kdd*, pp. 226–231.
- Farr, T.G., Rosen, P.A., Caro, E., Crippen, R., Duren, R., Hensley, S., Kobrick, M., Paller, M., Rodriguez, E., Roth, L., et al., 2007. The shuttle radar topography mission. *Reviews of geophysics* 45.
- Fernandez-Palomino, C.A., Hattermann, F.F., Krysanova, V., Lobanova, A., Vega-Jácome, F., Lavado, W., Santini, W., Aybar, C., Bronstert, A., 2022. A novel high-resolution gridded precipitation dataset for peruvian and ecuadorian watersheds: development and hydrological evaluation. *Journal of Hydrometeorology* 23, 309–336.
- Flores, F., López, L., Mite, A., 2023. Sitrep no. 87 - deslizamiento casual - alausí. <https://www.gestionderiesgos.gob.ec/wp-content/uploads/2023/06/SITREP-Nro.-87-Deslizamiento-Alausi-21062023-15h00.pdf>. Accessed: 04 July 2023.
- Froude, M.J., Petley, D.N., 2018. Global fatal landslide occurrence from 2004 to 2016. *Natural Hazards and Earth System Sciences* 18, 2161–2181. doi:10.5194/nhess-18-2161-2018.
- Funk, C., Peterson, P., Landsfeld, M., Pedreros, D., Verdin, J., Shukla, S., Husak, G., Rowland, J., Harrison, L., Hoell, A., 2015. The climate hazards infrared precipitation with stations—a new environmental record for monitoring extremes. *Scientific data* 2, 1–21.
- Goetz, J.N., Guthrie, R.H., Brenning, A., 2011. Integrating physical and empirical landslide susceptibility models using generalized additive models. *Geomorphology* 129, 376–386.
- Goldstein, R.M., Werner, C.L., 1998. Radar interferogram filtering for geophysical applications. *Geophysical research letters* 25, 4035–4038.

- Golub, G.H., Van Loan, C.F., 1980. An analysis of the total least squares problem. *SIAM journal on numerical analysis* 17, 883–893.
- Guarnieri, A.M., Tebaldini, S., 2008. On the exploitation of target statistics for sar interferometry applications. *IEEE Transactions on Geoscience and Remote Sensing* 46, 3436–3443.
- Guerrero, R., 2018. Memoria: Proceso de datos estación pluviométrica guarumales.
- Guns, M., Vanacker, V., 2013. Forest cover change trajectories and their impact on landslide occurrence in the tropical andes. *Environmental earth sciences* 70, 2941–2952.
- Guns, M., Vanacker, V., 2014. Shifts in landslide frequency–area distribution after forest conversion in the tropical andes. *Anthropocene* 6, 75–85.
- Guo, J., Xu, M., Zhao, Y., 2015. Study on reactivation and deformation process of xierguazi ancient-landslide in heishui reservoir of southwestern china, Springer. pp. 1135–1141.
- Gupta, A., 2011. *Tropical geomorphology*. Cambridge University Press.
- Guzzetti, F., Peruccacci, S., Rossi, M., Stark, C.P., 2008. The rainfall intensity–duration control of shallow landslides and debris flows: an update. *Landslides* 5, 3–17.
- Guzzetti, F., Reichenbach, P., Cardinali, M., Ardizzone, F., Galli, M., 2003. The impact of landslides in the umbria region, central italy. *Natural Hazards and Earth System Science* 3, 469–486. doi:[10.5194/nhess-3-469-2003](https://doi.org/10.5194/nhess-3-469-2003).
- Handwerger, A.L., Fielding, E.J., Huang, M., Bennett, G.L., Liang, C., Schulz, W.H., 2019a. Widespread initiation, reactivation, and acceleration of landslides in the northern california coast ranges due to extreme rainfall. *Journal of Geophysical Research: Earth Surface* 124, 1782–1797.
- Handwerger, A.L., Huang, M.H., Fielding, E.J., Booth, A.M., Bürgmann, R., 2019b. A shift from drought to extreme rainfall drives a stable landslide to catastrophic failure. *Scientific reports* 9, 1–12.

- Handwerger, A.L., Roering, J.J., Schmidt, D.A., 2013. Controls on the seasonal deformation of slow-moving landslides. *Earth and Planetary Science Letters* 377-378, 239–247. doi:[10.1016/j.epsl.2013.06.047](https://doi.org/10.1016/j.epsl.2013.06.047).
- Handwerger, A.L., Roering, J.J., Schmidt, D.A., Rempel, A.W., 2015. Kinematics of earthflows in the northern california coast ranges using satellite interferometry. *Geomorphology* 246, 321–333. doi:[10.1016/j.geomorph.2015.06.003](https://doi.org/10.1016/j.geomorph.2015.06.003).
- Hencher, S., 2010. Preferential flow paths through soil and rock and their association with landslides. *Hydrological processes* 24, 1610–1630.
- Hendron Jr, A.J., Patton, F.D., 1985. The vaiont slide. A geotechnical analysis based on new geologic observations of the failure surface. Volume 1. Main text. Technical Report.
- Herrera, G., Gutiérrez, F., García-Davalillo, J., Guerrero, J., Notti, D., Galve, J., Fernández-Merodo, J., Cooksley, G., 2013. Multi-sensor advanced dinsar monitoring of very slow landslides: The tena valley case study (central spanish pyrenees). *Remote Sensing of Environment* 128, 31–43. doi:[10.1016/j.rse.2012.09.020](https://doi.org/10.1016/j.rse.2012.09.020).
- Hersbach, H., Bell, B., Berrisford, P., Hirahara, S., Horányi, A., Muñoz-Sabater, J., Nicolas, J., Peubey, C., Radu, R., Schepers, D., 2020. The era5 global reanalysis. *Quarterly Journal of the Royal Meteorological Society* 146, 1999–2049.
- Hu, X., Bürgmann, R., Lu, Z., Handwerger, A.L., Wang, T., Miao, R., 2019. Mobility, thickness, and hydraulic diffusivity of the slow-moving monroe landslide in california revealed by l-band satellite radar interferometry. *Journal of Geophysical Research: Solid Earth* 124, 7504–7518.
- Hu, X., Lu, Z., Pierson, T.C., Kramer, R., George, D.L., 2018. Combining insar and gps to determine transient movement and thickness of a seasonally active low-gradient translational landslide. *Geophysical Research Letters* 45, 1453–1462.
- Huang, R., Jiang, L., Shen, X., Dong, Z., Zhou, Q., Yang, B., Wang, H., 2019. An efficient method of monitoring slow-moving landslides with long-range terrestrial laser scanning: a case study of the dashu landslide in the three gorges reservoir region, china. *Landslides* 16, 839–855.

- Huffman, G.J., Bolvin, D.T., Braithwaite, D., Hsu, K., Joyce, R., Kidd, C., Nelkin, E.J., Sorooshian, S., Tan, J., Xie, P., 2019. NASA Global Precipitation Measurement (GPM) Integrated Multi-satellite Retrievals for GPM (IMERG). Algorithm Theoretical Basis Doc. Technical Report.
- Huffman, G.J., Bolvin, D.T., Nelkin, E.J., Wolff, D.B., Adler, R.F., Gu, G., Hong, Y., Bowman, K.P., Stocker, E.F., 2007. The trmm multisatellite precipitation analysis (tmpa): Quasi-global, multiyear, combined-sensor precipitation estimates at fine scales. *Journal of hydrometeorology* 8, 38–55.
- Hungr, O., Evans, S., Bovis, M., Hutchinson, J., 2001. A review of the classification of landslides of the flow type. *Environmental & Engineering Geoscience* 7, 221–238.
- Hutchinson, J., 1988. General report: morphological and geotechnical parameters of landslides in relation to geology and hydrogeology, in: *Proceedings of 5th International Symposium on Landslides*, Balkema, Rotterdam, Netherlands, 1988, pp. 3–35.
- Intrieri, E., Raspini, F., Fumagalli, A., Lu, P., Del Conte, S., Farina, P., Allievi, J., Ferretti, A., Casagli, N., 2018. The maoxian landslide as seen from space: detecting precursors of failure with sentinel-1 data. *Landslides* 15, 123–133.
- Iverson, R.M., 2000. Landslide triggering by rain infiltration. *Water resources research* 36, 1897–1910.
- Jaboyedoff, M., Derron, M.H., 2020. Landslide analysis using laser scanners, in: *Developments in Earth Surface Processes*. Elsevier B.V. volume 23, pp. 207–230. doi:[10.1016/B978-0-444-64177-9.00007-2](https://doi.org/10.1016/B978-0-444-64177-9.00007-2).
- Jacquemart, M., Tiampo, K., 2021. Leveraging time series analysis of radar coherence and normalized difference vegetation index ratios to characterize pre-failure activity of the mud creek landslide, california. *Natural Hazards and Earth System Sciences* 21, 629–642. doi:[10.5194/nhess-21-629-2021](https://doi.org/10.5194/nhess-21-629-2021).
- Jekel, C.E., Venter, G., 2019. pwlf: a python library for fitting 1d continuous piecewise linear functions. URL: https://github.com/cjekel/piecewise_linear_fit_py.

- Jian, W., Wang, Z., Yin, K., 2009. Mechanism of the anlesi landslide in the three gorges reservoir, china. *Engineering Geology* 108, 86–95.
- Jokisch, B.D., Lair, B.M., 2002. One last stand? forests and change on ecuador's eastern cordillera. *Geographical Review* 92, 235–256.
- Jolivet, R., Agram, P.S., Lin, N.Y., Simons, M., Doin, M.P., Peltzer, G., Li, Z., 2014. Improving insar geodesy using global atmospheric models. *Journal of Geophysical Research: Solid Earth* 119, 2324–2341.
- Jolivet, R., Grandin, R., Lasserre, C., Doin, M.P., Peltzer, G., 2011. Systematic insar tropospheric phase delay corrections from global meteorological reanalysis data. *Geophysical Research Letters* 38.
- Kang, Y., Lu, Z., Zhao, C., Xu, Y., Kim, J.w., Gallegos, A.J., 2021. Insar monitoring of creeping landslides in mountainous regions: A case study in eldorado national forest, california. *Remote Sensing of Environment* 258, 112400.
- Kang, Y., Zhao, C., Zhang, Q., Lu, Z., Li, B., 2017. Application of insar techniques to an analysis of the guanling landslide. *Remote Sensing* 9, 1046. doi:[10.3390/rs9101046](https://doi.org/10.3390/rs9101046).
- Kirschbaum, D.B., Adler, R., Hong, Y., Kumar, S., Peters-Lidard, C., Lerner-Lam, A., 2012. Advances in landslide nowcasting: evaluation of a global and regional modeling approach. *Environmental Earth Sciences* 66, 1683–1696.
- Klimeš, J., 2018. Extensometer BT - *Encyclopedia of Engineering Geology*, Springer International Publishing, Cham, pp. 323–324. URL: https://doi.org/10.1007/978-3-319-73568-9_119, doi:[10.1007/978-3-319-73568-9_119](https://doi.org/10.1007/978-3-319-73568-9_119).
- Kuriakose, S.L., Van Beek, L.P.H., Van Westen, C.J., 2009. Parameterizing a physically based shallow landslide model in a data poor region. *Earth surface processes and landforms* 34, 867–881.
- Lacroix, P., Dehecq, A., Taipe, E., 2020a. Irrigation-triggered landslides in a peruvian desert caused by modern intensive farming. *Nature Geoscience* 13, 56–60.

- Lacroix, P., Handwerker, A.L., Bièvre, G., 2020b. Life and death of slow-moving landslides. *Nature Reviews Earth Environment* 1, 404–419.
- Li, Y., Uti, S., Milledge, D., Chen, L., Yin, K., 2021. Chasing a complete understanding of the failure mechanisms and potential hazards of the slow moving liangshuijing landslide. *Engineering Geology* 281, 105977.
- Litherland, M., Aspden, J., Clarke, M., Jemielita, R., Bermúdez, R., Viteri, F., Silva, K., 1994. Geological and metal occurrence maps of the southern cordillera real and el oro metamorphic belts, ecuador, escala 1: 500.000. Proyecto cordillera Real. Instituto Ecuatoriano de Minería (INEMIN), Corporación de desarrollo e investigación Geológico-Minero-Metalúrgico (CODIGEM) y British Geological Survey (BGS) .
- Loaiza-Usuga, J.C., Monsalve, G., Pertuz-Paz, A., Arce-Monsalve, L., Sanín, M., Ramírez-Hoyos, L.F., Sidle, R.C., 2018. Unraveling the dynamics of a creeping slope in northwestern colombia: Hydrological variables, and geoelectrical and seismic signatures. *Water* 10, 1498.
- Lollino, G., Allasia, P., Giordan, D., 2018. Inclinomometer BT - Encyclopedia of Engineering Geology, Springer International Publishing, Cham, pp. 509–512. URL: https://doi.org/10.1007/978-3-319-73568-9_167, doi:10.1007/978-3-319-73568-9_167.
- López, M., 1995. Estudio geológico-geotécnico del macro deslizamiento guarumales. Universidad Central del Ecuador: Quito, Ecuador .
- Lu, P., Casagli, N., Catani, F., Tofani, V., 2012. Persistent scatterers interferometry hotspot and cluster analysis (psi-hca) for detection of extremely slow-moving landslides. *International journal of remote sensing* 33, 466–489.
- Luteyn, J.L., Churchill, S.P., 2000. 11. vegetation of the tropical andes: An overview. *Imperfect Balance* , 281–310.
- Mackey, B.H., Roering, J.J., 2011. Sediment yield, spatial characteristics, and the long-term evolution of active earthflows determined from airborne lidar and historical aerial photographs, eel river, california. *Bulletin* 123, 1560–1576.

- Malet, J.P., Maquaire, O., Vanash, T., 2003. Hydrological behaviour of earthflows developed in clay-shales: investigation, concept and modelling. The occurrence and mechanisms of flows in natural slopes and earthfills, Patron Editore, Bologna , 175–193.
- Mancini, F., Ceppi, C., Ritrovato, G., 2010. Gis and statistical analysis for landslide susceptibility mapping in the daunia area, italy. *Natural Hazards and Earth System Sciences* 10, 1851–1864.
- Manz, B., Páez-Bimos, S., Horna, N., Buytaert, W., Ochoa-Tocachi, B., Lavado-Casimiro, W., Willems, B., 2017. Comparative ground validation of imerg and tmpa at variable spatiotemporal scales in the tropical andes. *Journal of Hydrometeorology* 18, 2469–2489.
- Matsuura, S., Asano, S., Okamoto, T., 2008. Relationship between rain and/or meltwater, pore-water pressure and displacement of a reactivated landslide. *Engineering Geology* 101, 49–59.
- McLaughlin, R.J., Ellen, S., Blake, M., Jayko, A.S., Irwin, W., Aalto, K., Carver, G., Clarke, S., 2000. Geology of the cape mendocino, eureka, garberville, and southwestern part of the hayfork 30× 60 minute quadrangles and adjacent offshore area, northern california. sea 1.
- McLAUGHLIN, R.J., Kling, S.A., Poore, R.Z., McDougall, K., Beutner, E.C., 1982. Post–middle miocene accretion of franciscan rocks, northwestern california. *Geological Society of America Bulletin* 93, 595–605.
- Miele, P., Di Napoli, M., Guerriero, L., Ramondini, M., Sellers, C., Annibaldi Corona, M., Di Martire, D., 2021. Landslide awareness system (laws) to increase the resilience and safety of transport infrastructure: The case study of pan-american highway (cuenca–ecuador). *Remote Sensing* 13, 1564.
- Mite-León, M., Barzola-Monteses, J., 2018. Statistical model for the forecast of hydropower production in ecuador. *Int. J. Renew. Energy Res* 10, 1130–1137.
- Molina, A., Vanacker, V., Brisson, E., Mora, D., Balthazar, V., 2015. Multidecadal change in streamflow associated with anthropogenic dis-

- turbances in the tropical andes. *Hydrology and Earth System Sciences* 19, 4201–4213.
- Monsieurs, E., Dewitte, O., Demoulin, A., 2019. A susceptibility-based rainfall threshold approach for landslide occurrence. *Natural Hazards and Earth System Sciences* 19, 775–789. doi:[10.5194/nhess-19-775-2019](https://doi.org/10.5194/nhess-19-775-2019).
- Monsieurs, E., Jacobs, L., Michellier, C., Basimike Tchangaboba, J., Ganza, G.B., Kervyn, F., Maki Mateso, J.C., Mugaruka Bibentyo, T., Kalikone Buzera, C., Nahimana, L., 2018. Landslide inventory for hazard assessment in a data-poor context: a regional-scale approach in a tropical african environment. *Landslides* 15, 2195–2209.
- Moreiras, S.M., 2005. Climatic effect of enso associated with landslide occurrence in the central andes, mendoza province, argentina. *Landslides* 2, 53–59.
- Mostbauer, K., Kaitna, R., Prenner, D., Hrachowitz, M., 2018. The temporally varying roles of rainfall, snowmelt and soil moisture for debris flow initiation in a snow-dominated system. *Hydrology and Earth System Sciences* 22, 3493–3513.
- Muenchow, J., Brenning, A., Richter, M., 2012. Geomorphic process rates of landslides along a humidity gradient in the tropical andes. *Geomorphology* 139, 271–284.
- Mulas, M., Formicola, P., Corsini, A., 2018. Development of gns lowcost receivers based monitoring array for landslides continuous monitoring. *Geophysical Research Abstracts* 20, 18048.
- Nappo, N., Peduto, D., Mavrouli, O., van Westen, C.J., Gullà, G., 2019. Slow-moving landslides interacting with the road network: Analysis of damage using ancillary data, in situ surveys and multi-source monitoring data. *Engineering geology* 260, 105244.
- van Natijne, A.L., Lindenbergh, R.C., Bogaard, T.A., 2020. Machine learning: New potential for local and regional deep-seated landslide nowcasting. *Sensors* 20, 1425. doi:[10.3390/s20051425](https://doi.org/10.3390/s20051425).

- Nicole, B., 2015. Analysis of slope stability by back-calculation along the paute river valley: Application to construction of the mazar hydroelectric project—ecuador, in: *Engineering Geology for Society and Territory-Volume 2*. Springer, pp. 301–306.
- Notti, D., Cina, A., Manzino, A., Colombo, A., Bendea, I.H., Mollo, P., Giordan, D., 2020. Low-cost gnss solution for continuous monitoring of slope instabilities applied to madonna del sasso sanctuary (nw italy). *Sensors* 20, 289. doi:[10.3390/s20010289](https://doi.org/10.3390/s20010289).
- Papathoma-Köhle, M., Zischg, A., Fuchs, S., Glade, T., Keiler, M., 2015. Loss estimation for landslides in mountain areas—an integrated toolbox for vulnerability assessment and damage documentation. *Environmental Modelling & Software* 63, 156–169.
- Pearson, R., 2011. *Exploring data in engineering, the sciences, and medicine*. OUP USA.
- Pearson, R.K., 2005. *Mining imperfect data: Dealing with contamination and incomplete records*. SIAM.
- Pecoraro, G., Calvello, M., Piciullo, L., 2019. Monitoring strategies for local landslide early warning systems. *Landslides* 16, 213–231. doi:[10.1007/s10346-018-1068-z](https://doi.org/10.1007/s10346-018-1068-z).
- Peruccacci, S., Brunetti, M.T., Gariano, S.L., Melillo, M., Rossi, M., Guzzetti, F., 2017. Rainfall thresholds for possible landslide occurrence in italy. *Geomorphology* 290, 39–57.
- Peterson, T.J., Western, A.W., Cheng, X., 2018. The good, the bad and the outliers: automated detection of errors and outliers from groundwater hydrographs. *Hydrogeology Journal* 26, 371–380.
- Petley, D., 2012. Global patterns of loss of life from landslides. *Geology* 40, 927–930. doi:[10.1130/G33217.1](https://doi.org/10.1130/G33217.1).

- Petley, D.N., Mantovani, F., Bulmer, M.H., Zannoni, A., 2005. The use of surface monitoring data for the interpretation of landslide movement patterns. *Geomorphology* 66, 133–147. doi:[10.1016/j.geomorph.2004.09.011](https://doi.org/10.1016/j.geomorph.2004.09.011).
- Pinyol, N.M., Alonso, E.E., Corominas, J., Moya, J., 2012. Canelles landslide: modelling rapid drawdown and fast potential sliding. *Landslides* 9, 33–51. doi:[10.1007/s10346-011-0264-x](https://doi.org/10.1007/s10346-011-0264-x).
- Pirasteh, S., Li, J., Chapman, M., 2018. Use of lidar-derived dem and a stream length-gradient index approach to investigation of landslides in zagros mountains, iran. *Geocarto International* 33, 912–926. doi:[10.1080/10106049.2017.1316779](https://doi.org/10.1080/10106049.2017.1316779).
- Plaza, G., Zevallos, O., Cadier, , 2011. La josefina landslide dam and its catastrophic breaching in the andean region of ecuador, in: *Natural and artificial rockslide dams*. Springer, pp. 389–406.
- Pratt, W.T., Duque, P., Ponce, M., 2005. An autochthonous geological model for the eastern andes of ecuador. *Tectonophysics* 399, 251–278.
- Prokešová, R., Medved'ová, A., Tábořík, P., Snopková, Z., 2013. Towards hydrological triggering mechanisms of large deep-seated landslides. *Landslides* 10, 239–254.
- Ramon, P., 1997. Resultados obtenidos en los drenajes subhorizontales instalados en el deslizamiento guarumales.
- Raspini, F., Bianchini, S., Ciampalini, A., Del Soldato, M., Montalti, R., Solari, L., Tofani, V., Casagli, N., 2019. Persistent scatterers continuous streaming for landslide monitoring and mapping: the case of the tuscan region (italy). *Landslides* 16, 2033–2044. doi:[10.1007/s10346-019-01249-w](https://doi.org/10.1007/s10346-019-01249-w).
- Raspini, F., Bianchini, S., Ciampalini, A., Del Soldato, M., Solari, L., Novali, F., Del Conte, S., Rucci, A., Ferretti, A., Casagli, N., 2018. Continuous, semi-automatic monitoring of ground deformation using sentinel-1 satellites. *Scientific reports* 8, 1–11.

- Robles, J., 2000. Estabilidad geológica de las zonas del embalse, presa, campamento guarumales y de otras instalaciones de la central hidroeléctrica paute.
- Robles, J., Guzmán, P., 2017. Informe de analisis de susceptibilidad de zonas inestables para prospeccion e implementación de instrumentacion.
- Robles, J., Villacis, R., Guzman, P., 2016. Informe de monitoreo geológico macro-deslizamiento guarumales.
- Rosen, P.A., Gurrola, E., Sacco, G.F., Zebker, H., 2012. The insar scientific computing environment, in: EUSAR 2012; 9th European conference on synthetic aperture radar, VDE. pp. 730–733.
- Rosser, N., Lim, M., Petley, D., Dunning, S., Allison, R., 2007. Patterns of precursory rockfall prior to slope failure. *Journal of Geophysical Research* 112, F04014. doi:[10.1029/2006JF000642](https://doi.org/10.1029/2006JF000642).
- Rosso, R., Rulli, M.C., Vannucchi, G., 2006. A physically based model for the hydrologic control on shallow landsliding. *Water Resources Research* 42.
- Schubert, E., Sander, J., Ester, M., Kriegel, H.P., Xu, X., 2017. Dbscan revisited, revisited: why and how you should (still) use dbscan. *ACM Transactions on Database Systems (TODS)* 42, 1–21.
- Schuster, R., Salcedo, D., Valenzuela, L., 2002. Overview of catastrophic landslides of south america in the twentieth century, in: *Catastrophic Landslides: Effects, Occurrence, and Mechanisms*. Geological Society of America, pp. 1–34.
- Schuster, R.L., 1979. Reservoir-induced landslides .
- Schuster, R.L., Fleming, R.W., 1982. Geologic aspects of landslide control using walls, in: *Application of Walls to Landslide Control Problems*, ASCE. pp. 1–18.
- Segoni, S., Piciullo, L., Gariano, S.L., 2018. A review of the recent literature on rainfall thresholds for landslide occurrence. *Landslides* 15, 1483–1501.
- Sidle, R., Ochiai, H., 2006. Processes, prediction, and land use. *Water resources monograph*. American Geophysical Union, Washington 525.

- Sidle, R.C., Bogaard, T.A., 2016. Dynamic earth system and ecological controls of rainfall-initiated landslides. *Earth-science reviews* 159, 275–291.
- Soto, J., Galve, J.P., Palenzuela, J.A., Azañón, J.M., Tamay, J., Irigaray, C., 2017. A multi-method approach for the characterization of landslides in an intramontane basin in the andes (loja, ecuador). *Landslides* 14, 1929–1947.
- Spikings, R., Winkler, W., Seward, D., Handler, R., 2001. Along-strike variations in the thermal and tectonic response of the continental ecuadorian andes to the collision with heterogeneous oceanic crust. *Earth and Planetary Science Letters* 186, 57–73.
- Strozzi, T., Farina, P., Corsini, A., Ambrosi, C., Thüring, M., Zilger, J., Wiesmann, A., Wegmüller, U., Werner, C., 2005. Survey and monitoring of landslide displacements by means of l-band satellite sar interferometry. *Landslides* 2, 193–201. doi:[10.1007/s10346-005-0003-2](https://doi.org/10.1007/s10346-005-0003-2).
- Tang, H., Wasowski, J., Juang, C.H., 2019. Geohazards in the three gorges reservoir area, china—lessons learned from decades of research. *Engineering Geology* 261, 105267.
- Tibaldi, A., Ferrari, L., Pasquarè, G., 1995. Landslides triggered by earthquakes and their relations with faults and mountain slope geometry: an example from ecuador. *Geomorphology* 11, 215–226.
- Tofani, V., Dapporto, S., Vannocci, P., Casagli, N., 2006. Infiltration, seepage and slope instability mechanisms during the 20–21 november 2000 rainstorm in tuscan, central italy. *Natural Hazards and Earth System Sciences* 6, 1025–1033.
- Tomás, R., Li, Z., Lopez-Sanchez, J.M., Liu, P., Singleton, A., 2016. Using wavelet tools to analyse seasonal variations from insar time-series data: a case study of the huangtupo landslide. *Landslides* 13, 437–450. doi:[10.1007/s10346-015-0589-y](https://doi.org/10.1007/s10346-015-0589-y).
- Tough, J., Blacknell, D., Quegan, S., 1995. A statistical description of polarimetric and interferometric synthetic aperture radar data. *Proceedings of the Royal Society of London. Series A: Mathematical and Physical Sciences* 449, 567–589.

- Urgilez Vinueza, A., Handwerger, A.L., Bakker, M., Bogaard, T., 2022. A new method to detect changes in displacement rates of slow-moving landslides using insar time series. *Landslides* 19, 2233–2247.
- Urgilez Vinueza, A., Robles, J., Bakker, M., Guzman, P., Bogaard, T., 2020. Characterization and hydrological analysis of the guarumales deep-seated landslide in the tropical ecuadorian andes. *Geosciences* 10, 267.
- Uwihirwe, J., Hrachowitz, M., Bogaard, T.A., 2020. Landslide precipitation thresholds in rwanda. *Landslides* 17, 2469–2481.
- Valentino, R., Montrasio, L., Losi, G.L., Bittelli, M., 2011. An empirical model for the evaluation of the degree of saturation of shallow soils in relation to rainfalls. *Canadian geotechnical journal* 48, 795–809.
- Vallet, A., Bertrand, C., Fabbri, O., Mudry, J., 2015. An efficient workflow to accurately compute groundwater recharge for the study of rainfall-triggered deep-seated landslides, application to the séchilienne unstable slope (western alps). *Hydrology and Earth System Sciences* 19, 427–449.
- Varnes, D.J., 1978. Slope movement types and processes. Special report 176, 11–33.
- Vásconez, F., 2000. Análisis de la peligrosidad de grandes deslizamientos en la república del ecuador con el caso-ejemplo guarumales. Johannes Gutenberg University of Mainz: Mainz, Germany .
- Vasconez, F., Vasconez, B., 2001. Evolucion del macrodeslizamiento guarumales periodo diciembre 1999—enero 2001.
- Villacis, R., Robles, J., 2015. Informe de la evolución del macrodeslizamiento guarumales.
- Vorpahl, P., Elsenbeer, H., Märker, M., Schröder, B., 2012. How can statistical models help to determine driving factors of landslides? *Ecological Modelling* 239, 27–39.

- Vremec, M., Collenteur, R., 2021. Pyet-a python package to estimate potential and reference evapotranspiration, pp. EGU21–15008.
- Wang, S., Zhang, K., van Beek, L.P., Tian, X., Bogaard, T.A., 2020. Physically-based landslide prediction over a large region: Scaling low-resolution hydrological model results for high-resolution slope stability assessment. *Environmental Modelling and Software* 124, 104607. doi:[10.1016/j.envsoft.2019.104607](https://doi.org/10.1016/j.envsoft.2019.104607).
- Warrick, J.A., Ritchie, A.C., Schmidt, K.M., Reid, M.E., Logan, J., 2019. Characterizing the catastrophic 2017 mud creek landslide, california, using repeat structure-from-motion (sfm) photogrammetry. *Landslides* 16, 1201–1219.
- Whiteley, J., Kendall, M., Sujitapan, C., Inauen, C., Swift, R., Watlet, A., Raines, M., Boyd, J., Cimpoiasu, M., Holmes, J., Sibbett, L., Uhlemann, S., Chambers, J., 2019a. An overview of high spatial resolution geophysical methods for landslide characterisation and monitoring, in: 25th European Meeting of Environmental and Engineering Geophysics, EAGE Publications BV. European Association of Geoscientists and Engineers, EAGE. pp. 1–5. doi:[10.3997/2214-4609.201902450](https://doi.org/10.3997/2214-4609.201902450).
- Whiteley, J.S., Chambers, J.E., Uhlemann, S., Wilkinson, P.B., Kendall, J.M., 2019b. Geophysical monitoring of moisture-induced landslides: A review. *Reviews of Geophysics* 57, 106–145. doi:[10.1029/2018RG000603](https://doi.org/10.1029/2018RG000603).
- Xu, C., Tian, Y., Zhou, B., Ran, H., Lyu, G., 2017. Landslide damage along araniko highway and pasang lhamu highway and regional assessment of landslide hazard related to the gorkha, nepal earthquake of 25 april 2015. *Geoenvironmental Disasters* 4, 14. doi:[10.1186/s40677-017-0078-9](https://doi.org/10.1186/s40677-017-0078-9).
- Xu, G., Li, W., Yu, Z., Ma, X., Yu, Z., 2015. The 2 september 2014 shanshucao landslide, three gorges reservoir, china. *Landslides* 12, 1169–1178.
- Xu, Y., Kim, J., George, D.L., Lu, Z., 2019. Characterizing seasonally rainfall-driven movement of a translational landslide using sar imagery and smap soil moisture. *Remote Sensing* 11, 2347.

- Yunjun, Z., Fattahi, H., Amelung, F., 2019. Small baseline insar time series analysis: Unwrapping error correction and noise reduction. *Computers & Geosciences* 133, 104331.
- Zeil, W., 1979. The andes-a geological review .
- Zerathe, S., Lacroix, P., Jongmans, D., Marino, J., Taïpe, E., Wathélet, M., Pari, W., Smoll, L.F., Norabuena, E., Guillier, B., 2016. Morphology, structure and kinematics of a rainfall controlled slow-moving andean landslide, peru. *Earth Surface Processes and Landforms* 41, 1477–1493.
- Zhang, Y., Liu, J., Cheng, Q., Xiao, L., Zhao, L., Xiang, C., Buah, P.A., Yu, H., He, Y., 2022. A new permanent displacement model considering pulse-like ground motions and its application in landslide hazard assessment. *Soil Dynamics and Earthquake Engineering* 163, 107556.
- Zhang, Y., Meng, X., Jordan, C., Novellino, A., Dijkstra, T., Chen, G., 2018. Investigating slow-moving landslides in the zhouqu region of china using insar time series. *Landslides* 15, 1299–1315. doi:[10.1007/s10346-018-0954-8](https://doi.org/10.1007/s10346-018-0954-8).
- Zhao, C., Kang, Y., Zhang, Q., Lu, Z., Li, B., 2018. Landslide identification and monitoring along the jinsha river catchment (wudongde reservoir area), china, using the insar method. *Remote Sensing* 10, 993.
- Zimmermann, B., Elsenbeer, H., 2009. The near-surface hydrological consequences of disturbance and recovery: a simulation study. *Journal of Hydrology* 364, 115–127.

A

**IN-SITU AND SATELLITE RAINFALL
ANALYSIS FOR THE MAZAR REGION**

Our research correlates the inventory of landslide velocity changes and potential hydrometeorological drivers in the Mazar area. Rainfall is one of the hydrometeorological factors to be studied; however, only one in-situ meteorological station with rainfall information is available in the area. The Mazar station has data starting from 03-2013; however, around 40% of the data is missing or has measurement errors (Figure A.1).

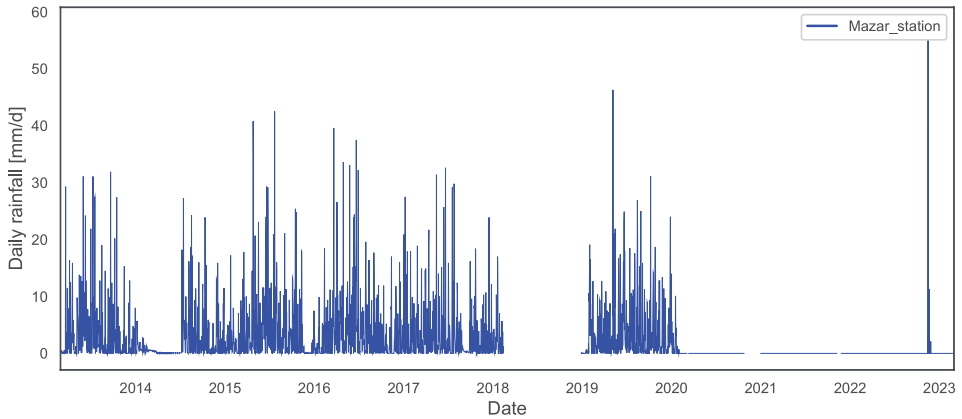


Figure A.1: Daily rainfall from the in-situ Mazar station

This situation raised concerns about the meteorological station's functionality and the rainfall data's applicability in this paper. Hence, we explored two options: The first option was to evaluate the quality of the rainfall data in the Mazar station using the double-mass curve analysis using a nearby station. We used the Guarumales station, located twenty kilometers downstream of the Mazar dam. This reliable meteorological station records data from 03-2013 and is used as a reference station for said analysis. Figure A.2 shows inconsistencies between these two stations. We plotted a scatter plot between the cumulative rainfall from both stations, and we found specific periods where the Mazar station might not be functioning correctly, as also observed in Figure A.1, where the data does not seem to follow the usual trends in 2014 and after 2020. There are missing data from the Mazar station, as also observed in Figure A.1 during 2018. Even though these inconsistencies are found in the double-mass curve, we can also observe that the rest of the period seems well correlated.

Therefore, we used scatter plots of daily and monthly rainfall, as shown in

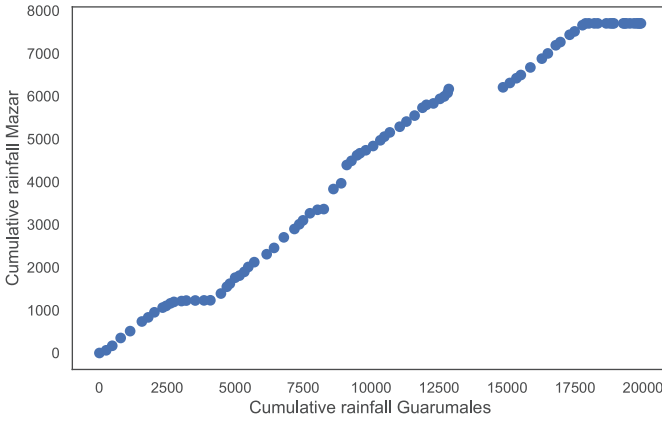


Figure A.2: Double-mass curve between the Guarumales and Mazar meteorological stations

Figure A.3, to perform an intra-station interpolation between these two meteorological stations. It is observed that the stations are well correlated, with a Pearson r of 0.6 for monthly rainfall (Figure A.2). Therefore, it was decided to infill the missing data and the data with possible measurement errors from the Mazar station using Equation A.1. from the linear regression between the two data sets.

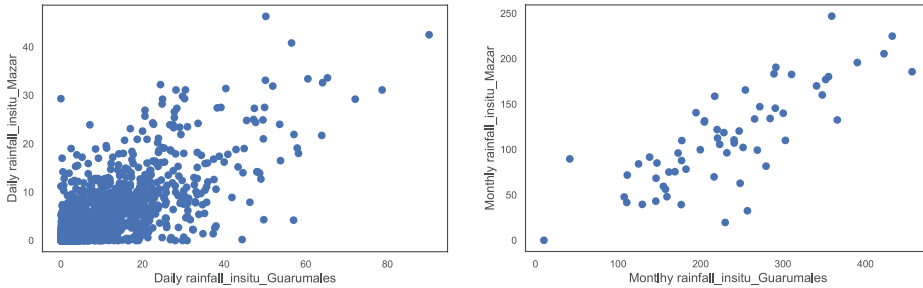


Figure A.3: Scatter plot between the Guarumales and Mazar meteorological stations in a daily (left) and monthly (right) timescale

$$P_{mazar} = \begin{cases} 0, & \text{if } P_{guarumales} = 0 \\ 0.4599 \times P_{guarumales} + 4.7581, & \text{otherwise} \end{cases} \quad (\text{A.1})$$

In Equation A.1, P_{mazar} is the rainfall of the Mazar station, and $P_{guarumales}$ is the rainfall from the Guarumales station. Applying this equation, daily and

monthly rainfall in the Mazar station results as shown in [Figure A.4](#).

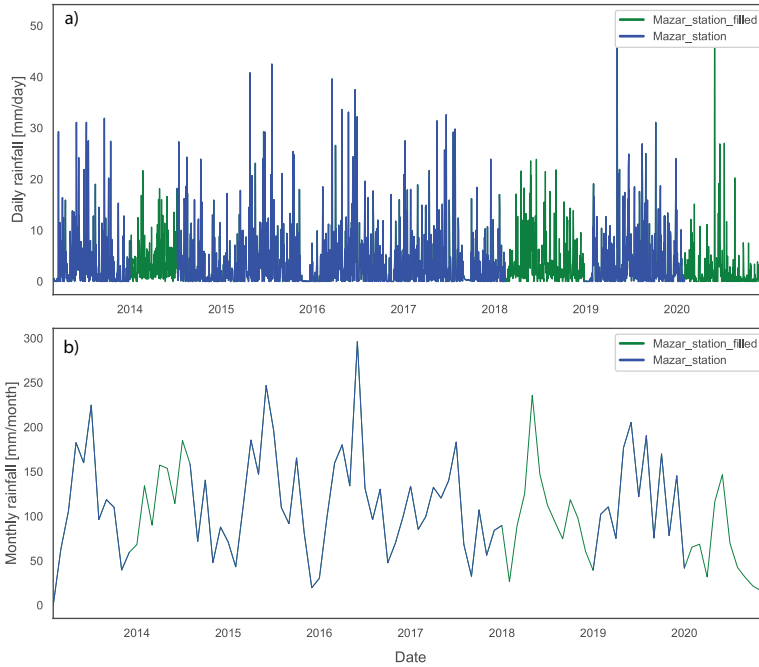


Figure A.4: Daily (a) and monthly (b) rainfall in the Mazar station with infilled data using the Guarumales station

The second option was to use satellite rainfall products over the area. The idea was to explore these products as an alternative to the current in-situ meteorological station. In this case, satellite rainfall was calculated as an area average over the study area ([Figure A.5](#)). The advantage of this option is the continuous dataset and the larger spatial footprint provided by the satellite products.

We considered two types of satellite-derived data for this evaluation: reanalysis precipitation data using ERA5 (spatial resolution: $0.1^\circ \times 0.1^\circ$) ([Hersbach et al., 2020](#)), which has been shown to outperform other reanalysis precipitation data and perform well in the Amazon river basin, and global merged precipitation products such as CHIRPS (spatial resolution: $0.05^\circ \times 0.05^\circ$) ([Funk et al., 2015](#)) and MSWEP (spatial resolution: $0.1^\circ \times 0.1^\circ$) ([Beck et al., 2017, 2019](#)). Gauge-based datasets were incorporated into satellite and reanalysis information in the global merged precipitation products. Additionally, two other satellite-derived precipitation products were considered: the Tropical Rainfall Measuring Mission

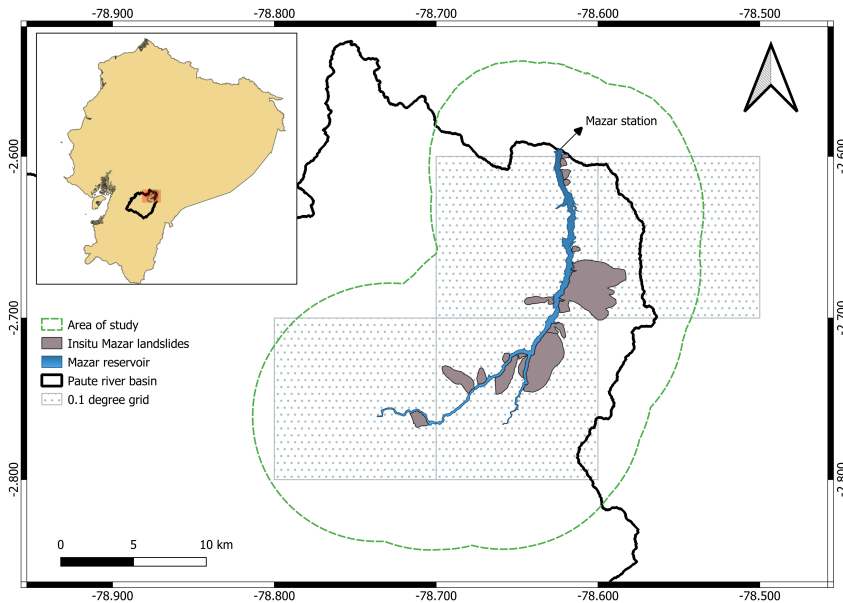


Figure A.5: Location of the Mazar meteorological station and pixels considered in the area for the satellite rainfall, with a spatial resolution of 0.1°

(TRMM) Multisatellite Precipitation Analysis (spatial resolution: $0.25^\circ \times 0.25^\circ$) (Huffman et al., 2007) and the Global Precipitation Measurement (GPM) Integrated Multisatellite Retrievals (spatial resolution: $0.1^\circ \times 0.1^\circ$) (Huffman et al., 2019). These data were compared to the in-situ data in the Mazar station (Figure A.6). It is observed that ERA5 rainfall overestimates and its temporal pattern does not match the in-situ rainfall pattern. The latter also happens with all satellite-based products, where the temporal patterns of the in-situ rainfall are not replicated. The satellite product that seems to be more related to the in-situ product is MSWEP, with a Pearson r of 0.49. All correlation coefficients can be observed in Table A.1.

The rest of the satellite products show a weak correlation, with Pearson r below 0.4. MSWEP in Figure A.6 seems to follow the rainfall patterns of the in-situ rainfall; however, there are temporal patterns that do not match what is observed in the field. It is essential to capture these patterns to evaluate them further with the displacements observed in the area, which is the main objective of chapter 4.

In the Ecuadorian tropical Andes, satellite rainfall estimations are often bi-

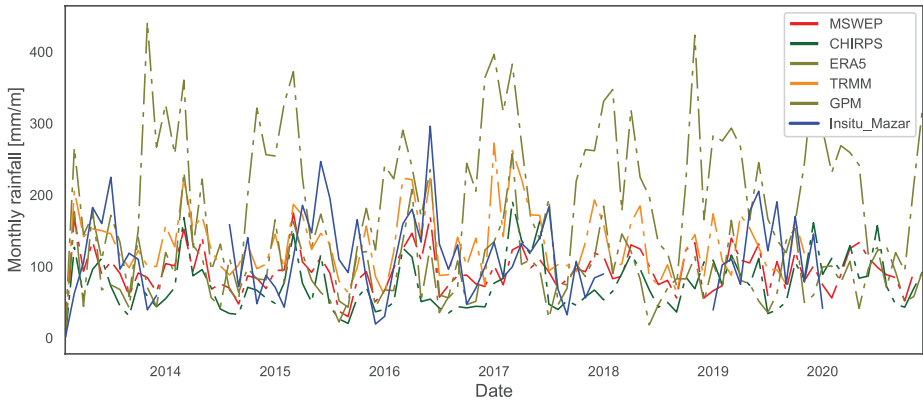


Figure A.6: Comparison between in-situ rainfall in the Mazar station and the five satellite-derived rainfall time series over the Mazar area

Table A.1: Pearson r between the satellite rainfall products and the in-situ rainfall from the Mazar station

Satellite product	Pearson r
ERA5	-0.10
MSWEP	0.49
CHIRPS	0.22
TRMM	0.35
GPM	0.12

ased or erroneous due to various climatic drivers that result in varied spatiotemporal precipitation patterns (Chavez and Takahashi, 2017; Manz et al., 2017; Erazo et al., 2018). Additionally, the use of these products is often restricted due to the short length of satellite records. Studies have attempted to produce high-resolution precipitation datasets in Ecuador and Peru (e.g., Fernandez-Palomino et al. (2022)); however, they found that it is still challenging to reproduce rainfall patterns, especially in parts of the Ecuadorian Andes. Considering these limitations, it was decided to use the infilled in-situ rainfall for further analyses in this chapter. Monthly rainfall (Figure A.4) is used further in the chapter to compare it to the inventoried velocity changes over the Mazar area.

ACKNOWLEDGEMENTS

This PhD journey has been enlightening. Through it, I've grown intellectually, professionally, and, most of all, personally. My intellectual growth would have never been possible without the outstanding guidance from my two promotors. I'm very grateful to Dr. Mark Bakker and Dr. Thom Bogaard. They have always been patient, kind, supportive, and honest. I'll always remember when Mark didn't give up on me and tried his best to put me on the right track. He's always been the voice of reason. Thom was the person who brought me here, accepted me into this program, and guided me from beginning to end. He's been there for me for all academic and sometimes non-academic issues. He supported me when I decided to work for a few months while doing my PhD. I'll always be grateful for that. Thank you for being part of this journey. I'm thankful to the department's Secretaries for their support since my PhD began.

I'm also thankful to my supervisor in Ecuador, Dr. Pablo Guzman, and his colleagues and good friends, Jessica Robles and Rigoberto Guerrero. They provided me with the data I needed for the development of this thesis and also their support when I asked for it.

My sincere gratitude goes to the team at IGRAC, with whom I shared most of 2022 working together. I found great people who were always happy to help or assist in anything I needed to work. They made me feel welcome and supported when they knew I was doing my PhD alongside my work. To Claudia, Stefan, Christina, Arnaud, and Elisabeth, thank you very much!

I am very thankful to my colleagues in the Water Management department with whom I've shared most of my time at TU Delft: Dr. Judith Uwihirwe, Dr. Chelsea Kandroop, Bahareh Kianfar, Jenny Soonthornrangsan, and Dr. Changrang Zhou. We had many enjoyable moments together and shared successes and setbacks. Those less-than-good moments were not too bad as long as someone was around. Thank you for being there for me.

I'm deeply thankful to my friends outside the university who became my family in the Netherlands: Gabriela Martínez, Dr. Martin Lefevre, Ir. Aislín Marquez, Ir. Pedro Villavicencio, Dr. Pamela Cerón, Ir. Monireh Azimi, and Ingrid Úbeda. You were there for me whenever I felt alone or needed a shoulder. You always had time for me, good words, and good food to share!

I can't begin to express my gratitude to my husband, Ir. Ismael Portilla. At my lowest, he has always been my pillar. He's supported me on this journey, even before I started applying for the program. He always knew I'd make it, which served greatly on the times I didn't believe it myself. He's been my rock for almost 14 years, and I'm grateful he's in my life.

Y a mi familia y mis padres, Ramiro y Rocío, les estoy profundamente agradecida por todo lo que han dado. Han sacrificado mucho para que yo esté aquí; siempre estaré agradecida por eso. Siempre tenían palabras amables, incluso si no entendían mucho de lo que estaba haciendo; eso no importaba porque solamente necesitaba sentir sus corazones abrazando el mío.

Alexandra Urgilez Vinueza

CURRICULUM VITAE

Alexandra Urgilez Vinueza

Alexandra Urgilez was born on 1st October 1990 in Cuenca, Ecuador. She conducted her PhD research on “Analysis of the slow-moving landslides in the Mazar region in southeast Ecuador”. In September 2016, she completed her Master’s degree in Hydrogeology and Water Management under the School of Engineering, faculty of Science, Agriculture, and Engineering at Newcastle University, United Kingdom. In 2013, she completed her undergraduate study as a Civil Engineer, from the Engineering Faculty at the Universidad de Cuenca, in Cuenca, Ecuador. After her undergraduate studies, from 2014 to mid-2015, she worked as a Project Engineer at the Program for soil and water management (PROMAS) at the Universidad de Cuenca. After returning from her master’s studies, she joined Petroamazonas, Quito for 8 months working as a Project Engineer in the Civil Engineering department. She returned to Cuenca by the end of 2017, where she re-joined PROMAS for 4 months before traveling to The Netherlands for her PhD. The findings of her PhD research have been presented at numerous international conferences: the European Geoscience Union EGU 2019-2020-2021; the Fifth World Landslide Forum WLF 5 in 2021. Her first poster presented at EGU, 2019 was awarded the Outstanding Student and PhD candidate Presentation OSPP award. The findings of her PhD resulted in publications in peer review journals and conference abstracts.

LIST OF PUBLICATIONS

A.1. PAPERS

2. **Urgilez Vinueza, A.**, Handwerger, A.L., Bakker, M., and Bogaard, T. (2022). *A new method to detect changes in displacement rates of slow-moving landslides using InSAR time series*. *Landslides*, 19(9), 2233-2247, <https://doi.org/10.1007/s10346-022-01913-8>
1. **Urgilez Vinueza, A.**, Robles, J., Bakker, M., Guzman, P., and Bogaard, T. (2020). *Characterization and hydrological analysis of the Guarumales deep-seated landslide in the tropical Ecuadorian Andes*. *Geosciences*, 10(7), 267, <https://doi.org/10.3390/geosciences10070267>

A.2. PRESENTATIONS

5. **Urgilez Vinueza, A.** (2023). *Potencial de la información satelital para el manejo de amenazas naturales*. In Feria de Innovación y Sostenibilidad en la Construcción.
4. **Urgilez Vinueza, A.** (2022). *Evaluation of the G3P Global Gravity-based Ground-water product*. In G3P General Assembly.
3. **Urgilez Vinueza, A.**, Handwerger, A.L., Bakker, M., and Bogaard, T. (2021). *A new method to detect changes in displacement rates of slow-moving landslides using InSAR time series*. In EGU General Assembly Conference, No. EGU21-14447.
2. **Urgilez Vinueza, A.**, Robles, J., Bakker, M., Guzman, P., and Bogaard, T. (2019). *The occurrence of Landslides in Guarumales, Ecuador*. In EGU General Assembly Conference Abstracts (p. 5100).
1. **Urgilez Vinueza, A.** (2017). *Development of a Hydrogeological Model for Managing Deep-Seated Landslides in Guarumales–Ecuador*. In V CONGRESO REDU (p. 364).